TU Graz

AFFIDAVIT

I declare that I have authored this thesis independently, that I have not used other than the declared sources/resources, and that I have explicitly indicated all material which has been quoted either literally or by content from the sources used. The text document uploaded to TUGRAZonline is identical to the present doctoral thesis.

Date	Signature

Abstract

The transport of charge carriers in semiconductors is a topic of utmost interest in many fields of semiconductor processing and device development. In this work Electron Beam Induced Current (EBIC) measurements were done in combination with three dimensional Technology Computer Aided Design (TCAD) simulations to characterize the transport of minority charge carriers in silicon *p-n* junction devices. EBIC measurements produce a spatially resolved map of the diode's response and give additional information to standard characterization methods like spectral responsivity, dark current and capacitance measurements. The influence of doping concentration, electron beam energy, surface quality and diode biasing on the EBIC signal was investigated, using simple step junction diode structures produced by epitaxial deposition. A large influence of surface preparation on the EBIC signal was shown and a measurement method to evaluate the surface quality is presented. This rather simple structure, was also used to set up and calibrate the EBIC TCAD simulation environment. Simulation results are presented, which fit the measurements very well. To investigate the diffusion lengths depending on substrate material and doping and the influence of CMOS processing, a dedicated test chip was designed, which was processed in a 0.35 µm high voltage CMOS process and investigated. Additionally to substrate type, also different *n*-well types were examined. It is shown that for the extraction of bulk transport properties a high surface quality is necessary while for the investigation of junction shapes and positions a high surface recombination rate is preferable. A procedure to remove the oxide stack on top of investigated region was introduced.

Kurzfassung

In vielen Bereichen der Halbleiterprozessierung und der Entwicklung von Halbleiter Bauelementen ist der Ladungsträgertransport von höchster Bedeutung. In dieser Arbeit, werden Electron Beam Induced Current (EBIC) Messungen, also die Anregung von Ladungsträgern unter Verwendung eines Elektronenstrahls, verwendet um den Transport, von Minoritätsladungsträgern in Silizium Bauelementen mit *p-n* Übergang, zu untersuchen. Zusätzlich zu den experimentellen Messungen, wurden drei dimensionale Technology Computer Aided Design (TCAD) Simulationen durchgeführt. EBIC Messungen produzieren räumlich aufgelöste Abbildungen der Dioden Charakteristik und geben so wertvolle zusätzliche Informationen zu üblichen Charakterisierungsmethoden, wie spektraler Respons, Dunkelstrom und Kapazitäten Messungen. Der Einfluss von Dotierkonzentration, Elektronenstrahlenergie, Oberflächenqualität und das Betreiben der Diode in Sperrrichtung, auf das EBIC Signal wurden untersucht. Dafür wurden Strukturen mit beinahe abruptem *p-n* Übergang verwendet, welche mittels epitaktischem Wachstum produziert wurden. Ein sehr markanter Einfluss von Oberflächenpräparation auf das EBIC Signal wurde beobachtet und im Zuge dessen, wird eine Messmethode zur Evaluierung der Oberflächenqualität vorgestellt. Diese eher einfache Struktur, wurde verwendet um die EBIC TCAD Simulationsumgebung aufzusetzen und zu kalibrieren. Simulationsergebnisse, die den Messungen sehr gut entsprechen werden präsentiert. Um Diffusionslängen in Abhängigkeit von Substratmaterialien zu extrahieren wurde ein speziell designter Test Chip entwickelt, in einem 0.35 µm Hochvolt CMOS Prozess produziert und untersucht. Zusätzlich zum Startmaterial, wurden auch verschiedene *n*-Wannen Arten prozessiert und verglichen. Es wird aufgezeigt, dass um Substrat Transporteigenschaften zu extrahieren, eine hohe Oberflächenqualität notwendig ist. Andererseits, ist eine hohe Oberflächenrekombinationisrate Vorteilhaft, um die Form und Positionen von Übergängen aufzuzeigen. Es wird ein Verfahren vorgestellt, um die vorhandenen Oxid Schichten über der zu untersuchenden Region, zu entfernen und dabei das Messergebnis so wenig wie möglich zu beeinflussen.

Acknowledgements

I would like to thank both my supervisors from TU Graz and ams AG, Peter Hadley and Rainer Minixhofer for their great support over these years. I'm very thankful for having two supervisors who cared so much and being so interested in my work. Thanks a lot for the inspiring discussions and motivating me when needed.

Special thanks, to my whole group at ams AG who welcomed me in their group and always supported me. Especially I want to thank, Ingrid, Frederic, Georg and Jong Mun who always took the time for discussions and explanations. Frederic, thanks a lot for being so patient with me and my simulation skills.

I also want to thank all my colleagues from the "teambuilding" group, who became real friends over these years and who made the work place a place where I enjoyed to be and liked to go. Thanks to all of you, for the coffee and cheering me up when I was down and making my time as a PhD student such a special time.

Finally I wan to express my gratitude for my parents and my whole family, who made my studies possible. They always supported me emotionally and financially. Thank you for being so proud of me.

Contents

Declaration of Authorship **i**

Abstract **ii**

Kurzfassung **iii**

Acknowledgements **iv**

1 Introduction **1**

2 Carrier transport in semiconductors **3**
2.1 Carrier drift 3
2.2 Carrier diffusion 4
2.3 Carrier recombination and generation 4
2.4 Lifetime and diffusion length 5
2.4.1 Recombination lifetime 5
Surface recombination rate 7
2.5 Continuity equation 7

3 Measurement of semiconductor transport properties **9**
3.1 Measurement Methods 10

4 Electron matter interaction **13**
4.1 Electron beam damage and surface charging 15
4.1.1 Beam damage due to elastic scattering 15
4.1.2 Beam damage due to inelastic scattering 15

5 *p*-*n* Junctions **17**

6 EBIC measurement methodology **21**
6.1 Quantitative measurement of semiconductor parameters 23
6.2 Experimental set-up and measurement procedure 23

7 EBIC TCAD simulation **26**
7.1 Introduction to TCAD 26
7.2 TCAD Simulation of EBIC measurements 26
7.2.1 Electron beam generation 26
7.2.2 Parameters included in model 27
7.2.3 Structure Generation 30
7.2.4 Transient simulation and EBIC line scan 31

8 EPI diodes **32**
8.1 Structure 32
8.2 Sample preparation 34
8.3 Mesurement and simulation results 35

8.3.1 Influence of surface recombination rate . . . 35
8.3.2 Influence of doping concentration . . . 40
8.3.3 Influence of electron beam energy . . . 43
8.3.4 Biasing of the diode . . . 45
8.4 Simulation of influence of interface charge and bulk lifetime . . . 47
8.4.1 Minority carrier lifetime . . . 47
8.4.2 Surface Charge . . . 48
8.5 Extraction of surface recombination velocity . . . 57
8.6 Conclusions from EPI diode investigations . . . 60

9 EBIC testchip 61
9.1 The test structure . . . 61
9.2 Sample preparation . . . 63
9.3 Influence of sample preparation . . . 64
9.4 Determination of diffusion length . . . 67
9.5 Influence of *n*-well type . . . 72
9.6 Influence of electric field across structure . . . 80
9.7 EBIC on cross-sections . . . 82
9.7.1 Cleaved sample . . . 82
9.7.2 FIB cross-section . . . 84
9.8 EBIC TCAD simulation . . . 86
9.9 Rectangular diodes . . . 88
9.10 Conclusion on EBIC testchip . . . 89

10 Conclusion 91

Bibliography 94

List of Figures

2.1 Different recombination mechanisms: (a) Shockley-Read-Hall recombination, (b) radiative recombination and (c) auger recombination.[25] . . 5

4.1 Schematic showing the interaction between incident electron beam and sample. 13
4.2 Monte Carlo simulations of electron trajectory paths using Casino [46] for Silicon and Gold. (a) Silicon the Electron beam energy is 5 keV, (b) Silicon and 20 keV, (c) Gold and 5 keV and (d) Gold and 20 keV. 14

5.1 Abrupt *p-n* junction in thermal equilibrium. In (a) the space charge dirstribution, in (b) the electric field distribution and in (c) the potential variation is shown.[47] 18
5.2 The biasing modes are shown schematically and the corresponding energy bands. In (a) without applied bias, in (b) forward bias and in (c) reverse bias.[47] 19

6.1 Different geometries used in EBIC measurements are shown. A junction perpendicular to the surface is shown for the case of a *p-n* junction in (a) and for the case of a Schottky junction in (b). A configuration with normal junction to the surface is shown in (c) for a *p-n* junction and in (d) for a Schottky junction. [43] 22
6.2 EBIC measurement geometry of a *n*-type well in a *p*-type substrate including a vertical and a horizontal junction. 23
6.3 The experimental measurement set-up. In (a) the nano prober shuttle, in (b) the cross-section prober shuttle and in (c) the controller for the nano prober shuttle and the amplifier. 25

7.1 2D projection of electron-hole pair generation for a 10 keV electron beam. 28
7.2 Depth dose function simulation, comparison between Casino and analytic calculation. 28
7.3 Examples for placement of electron hole pair generation volume across the structure. A 2 dimensional cut through the three-dimensional structure used for simulation is shown. 29
7.4 Output of transient simulation for several x-positions of the electron-hole generation volume. Showing the measured current at one contact in dependence on the time. 31

8.1 Schematic structure of EPI diode in cross-section view and measurement mode shown. 32
8.2 3D Structure generated by simulation. The color coding is showing the doping concentration in cm^{-3} [61] 33
8.3 The simulated carrier density (a) and electric field (b) are shown. The *n*-EPI doping concentration is 10^{16} cm^{-3} and the *p*-doping is 7×10^{14} cm^{-3}. 34

8.4 In (a) the SEM image of the cross-section sample is shown and in (b) the corresponding EBIC signal. 35
8.5 Data extraction from measurement. A 1D line scan is extracted out of the calibrated 2D EBIC signal 36
8.6 Comparison of EBIC line-scan done by simulation and measurement. The electron beam energy is 20 keV and the electron beam current 200 pA. 36
8.7 EBIC line scan of a HF etched and a ground sample. The n-EPI concentration was 10^{16} cm^{-3} and the p-EPI concentration was 7×10^{14} cm^{-3}. The electron beam energy was 20 keV. 37
8.8 Investigation of surface quality using TEM analysis. TEM image of a lamella prepared from (a) a simply cleaved sample, (b) an HF etched sample and (c) a ground sample. In the case of the ground sample an AuPd and Pt layer was used as protection layer. In the case of the cleaved and the HF etched sample only a Pt layer is used. The used electron beam energy was 200 keV. The specimens were oriented so that the [1 0 1] (b) and the [1 0 0] (c) orientation of the silicon substrate could be imaged. [61] The TEM images were done at FELMI-ZFE the austrian center of electron microscopy and nanoanalysis. 38
8.9 Influence of beam current on EBIC signal. (a) Three sub-sequentially measured EBIC line-scans [61] and (b) a 2D EBIC image after a zoomed in measurement in the center of the image showing the degradation of the EBIC signal of an HF etched sample using 1.6 nA electron beam current. The electron beam energy was 20 keV. 39
8.10 Schematic structure of EPI diode in cross-section view and measurement mode used for simulations. 40
8.11 The influence of surface quality on the EBIC signal is shown. In (a) the simulated EBIC signal for surface recombination rates from 0 cm/s to 10^7 cm/s are plotted. In (a) the measurements of and simulation for two surface conditions are shown. The n-EPI doping concentration was 10^{16} cm^{-3} and the p-EPI doping concentration was 7×10^{14} cm^{-3}. [61] . 41
8.12 The influence of n-doping concentration is simulated in (a) for a surface recombination rate of 10^7 cm/s, 10^5 cm/s in (b) and in (c) for 10^3 cm/s. The p-doping is 7×10^{14} cm^{-3}. The electron beam energy used is 20 keV. 42
8.13 The influence of p-doping concentration. Comparison between 7×10^{14} cm^{-3} and 10^{13} cm^{-3}. (a) Measurement of ground sample (b) simulation with a surface recombination velocity of 10^6 cm/s. The n-doping is 10^{16} cm^{-3}. The electron beam energy used is 20 keV. 43
8.14 The influence of the electron beam energy was investigated. (a) The EBIC signal of a ground sample and (b) an HF etched sample is shown. The EBIC signal was normalized to its maximum value. The n-doping concentration was 10^{16} cm^{-3} and the p-doping 7×10^{14} cm^{-3} in both cases. [61] 44
8.15 The influence of the electron beam energy was investigated by simulation. (a) The surface recombination rate is $s_0 = 10^3$ cm/s and in (b) $s_0 = 10^6$ cm/s. The EBIC signal is normalized to its maximum value. The n-doping concentration is 10^{16} cm^{-3} and the p-doping 7×10^{14} cm^{-3} in both cases. [61] 45

8.16 Influence of reverse biasing of the diode on EBIC signal. (a) Measured EBIC signal and (b) simulated. The reverse bias voltage ranged from 0 V to 20 V. The sample surface was ground in the experimental case and $s_0 = 10^5$ in the simulation. The *n*-doping concentration was 10^{16} cm^{-3} and the *p*-doping concentration 10^{13} cm^{-3}. 46
8.17 The simulated electric field distribution at reveres bias voltages from 0 V to 20 V. The *n*-doping concentration was 10^{16} cm^{-3} and the *p*-doping concentration 10^{13} cm^{-3}. 47
8.18 Schematic structure of symmetric design in cross-section view. 48
8.19 The simulated EBIC signal for lifetime values ranging from 10^{-5} s to 10^{-8} s. The *n*- and *p*-type doping concentration is 7×10^{14} cm^{-3}. The electron beam energy is 10 keV 48
8.20 The simulated EBIC signal for surface recombination rate values ranging from 10^3 cm/s to 10^7 cm/s. The *n*- and *p*-type doping concentration is 7×10^{14} cm^{-3}. The electron beam energy is 10 keV 49
8.21 The simulated EBIC signal for various negative and positive charge densitties placed at the silicon/silicon-dioxide interface. In (a) the surface recombination velocity is 10^3 cm/s and in (b) 10^6 cm/s. The electron beam energy was 20 keV. 50
8.22 In (a) the electron density for a positive surface charge density of 10^{11} cm^{-2} is shown. In (b) the hole density for a neative surface charge density of 10^{11} cm^{-2}. 51
8.23 The simulated electric field no surface/interface charge. An overview image and zoomed in to the area of the junction 52
8.24 The simulated electric field for positive interface charge density of 10^{11} cm^{-2}. An overview image and zoomed in to the area of the junction 53
8.25 The simulated electric field for positive interface charge density of 10^{10} cm^{-2}. An overview image and zoomed in to the area of the junction 54
8.26 The simulated electric field for negative interface charge density of 10^{11} cm^{-2}. An overview image and zoomed in to the area of the junction 55
8.27 The simulated electric field for negative interface charge density of 10^{10} cm^{-2}. A overview and zoomed in to the area of the junction 56
8.28 The simulated EBIC signal for various negative and positive charge densities placed at the silicon/silicon-dioxide interface. The *n*- and *p*-type doping concentration is 7×10^{14} cm^{-3}. 56
8.29 The simulated EBIC signal at two x-positions (46 µm is on the *n*-side and 54 µm is on the *p*-side) for a surface recombination rate of 10^3 cm/s and 10^7 cm/s in dependence on the electron beam energy is shown in (a) in (b) the normalized signal is plotted. 57
8.30 The simulated EBIC signal at two x-positions (46 µm is on the *n*-side and 54 µm is on the *p*-side) for electron beam energies of 2 keV and 20 keV in dependence on the surface recombination rate is shown in (a). In (b) the normalized signal is plotted. 58
8.31 In (a) the normalized measured EBIC signal is in dependence on the electron beam energy is shown for a ground sample and an HF etched sample. The x-position is in the *p*-region (10 µm. In (b) the simulated normalized EBIC signal is shown at the same x-position in dependence on surface recombination rate. The electron beam energy is 10 keV and 20 keV. 59

9.1 Top view of schematic structure of test chip. 63

9.2 Cross-section of schematic structure. In (a) the standard *n*-well in p-substrate structure is shown and in (b) the structure with surface passivation included is shown. 63
9.3 Schematic built up of test chip including back end of line stack. 64
9.4 2D EBIC signal of a passivated structure. In (a) the SEM image is shown and in (b) the corresponding EBIC image. 64
9.5 2D EBIC signal of a unpassivated structure of an over-etched sample. In (a) the first recorded image is shown while in (b) the same image was recorded after watching several minutes zoomed in. 65
9.6 2D EBIC signal of a unpassivated structure of a sample with residual oxide. In (a) the first recorded image is shown while in (b) the same image was recorded after watching several minutes. 65
9.7 Spectral responsivity in A/W for an unetched and two etched samples. 66
9.8 Schematic of the test chip including BEOL stack after BEOL etching. . . 67
9.9 Spectral responsivty in A/W of rectangular test diode. Comparison between an unetched sample, a sample with mask etching and a sample with mask etching with subsequent HF etching. 67
9.10 2D EBIC signal used for extraction of diffusion length and extracted linescan. The beam energy was 20 kev and the beam current 200 pA. . . 68
9.11 Comparison of EBIC linescans measured with a beam current of 200 pA and 800 pA respectively. The electron beam energy was 20 keV in both cases. 69
9.12 EBIC linescans of various substrate types. The investigated structures were NW with surface passivation. Electron beam energy was 20 keV and electron beam current was 200 pA. 69
9.13 EBIC linescans of Sample 1 and Sample 5. Comparison between bulk substrate and EPI substrate with same resitivity and from the same supplier. The investigated structures were NW with surface passivation. Electron beam energy was 20 keV and electron beam current was 200 pA. 70
9.14 EBIC linescans of a unpassivated NW design. Electron beam energy was 20 keV and electron beam current was 200 pA and 800 pA respectively. . 71
9.15 EBIC linescans of a NW design with and without passivation. Electron beam energy was 20 keV and electron beam current was 800 pA. 72
9.16 2D EBIC signal of different n-well types in passivated design. Measurement was done with a beam energy of 20 keV and a beam current of 0.8 nA. (a) n+ (b) NW (c) DN and (d) DN2 73
9.17 1D EBIC signal of different n-well types in passivated design. Measurement was done with a beam current of 0.8 nA. Electron beam energy was(a) 10 keV (b) 20 keV and (c) 30 keV 74
9.18 2D EBIC signal of n+-well in passivated design for different electron beam energies. A beam current of 0.8 nA was used. (a)10 keV (b) 20 keV and (c) 30 keV electron beam energy 75
9.19 2D EBIC signal of NW in passivated design for different electron beam energies. A beam current of 0.8 nA was used. (a) 10 keV (b) 20 keV and (c) 30 keV electron beam energy 76
9.20 2D EBIC signal of DN2 in passivated design for different electron beam energies. A beam current of 0.8 nA was used. (a) 10 keV (b) 20 keV and (c) 30 keV electron beam energy 77
9.21 1D EBIC signal of different n-well types in passivated design. Measurement was done using a beam current of 0.8 nA and electron beam energies of 10 keV, 20 keV and 30 keV. (a) n+ (b) NW (c) DN and (d) DN2 79

9.22 The EBIC signal normalized by the electron beam current (0.8 nA) for 10, 20 and 30 keV for different *n*-well types. 79
9.23 2D EBIC signal of a passivated DN structure. No voltage was applied on the contacts.(a) Coloured EBIC plot and (b) contour plot. 80
9.24 2D contour plot of the EBIC signal of passivated DN with different voltage applied to the left contact. (a) -5 V (b) -10 V and (c) -15 V 81
9.25 2D EBIC signal of a passivated DN structure. On the right contact -20 V are applied.(a) Coloured EBIC plot and (b) contour plot. 81
9.26 EBIC measurement of a cross-secton on a cleaved sample. In (a) the SEM image is shown and in (b) the 2D EBIC sginal. Electron beam energy was 10 keV and electron beam current 0.8 nA. 82
9.27 EBIC measurement of a cross-secton on a cleaved sample. The Evolution of the EBIC signal with time is shown. Electron beam energy was 10 keV and electron beam current 0.8 nA. 83
9.28 EBIC measurement of a cross-secton on a cleaved sample. Comparison between unpassivated DN (a) and passivated DN (b). Electron beam energy was 5 keV and electron beam current 0.8 nA. 83
9.29 EBIC measurement on a FIB cross-section. (a) SEM image and (b) corresponding EBIC image. The sample was tilted 45°. [61] 84
9.30 2D EBIC signal of FIB x-sections. (a)Passivated NW and (b) Passivated DN. The electron beam energy was 10 keV, the beam current 0.8 nA and the sample was tilted 55° in both cases. 85
9.31 2D EBIC signal of FIB x-sections.(a) Passivated *n*+ well and (b) zoomed in passivated *n*+ well. The electron beam energy was 10 keV, the beam current 0.8 nA and the sample was tilted 75° in both cases. 86
9.32 Structure generated with Sentaurus SProcess and Sentaurus SDE showing the doping profile. Blue tones are *p*-type and red/yellow tones are *n*-type doping (dark colors high doping concentration, light colors low doping concentration) (a) 3D and (b) 2D. 86
9.33 Structure generated by Sentaurus SProcess and Sentaurus SDE showing the electric field distribution in a 2D cut. 87
9.34 Simulated EBIC linescans of a DN n-well design with passivation for a surface recombination rate of 10^3 cm/s and 10^6 cm/s. Electron beam energy was 20 keV. 87
9.35 Simulated EBIC linescans of a DN n-well design with passivation for a surface recombination rate of 10^3 cm/s and 10^6 cm/s. Electron beam energy was 20 keV and the lifetime in the *p*-well passivation is decreased relative to the substrate lifetime. 88
9.36 (a) SEM image of rectangular *n*-well in *p*-substrate diode and (b) corresponding EBIC image. 88
9.37 2D EBIC signals showing different corner shapes of standard rectengular diodes. (a) 90° corner, (b) beveled corner with 45° and (c) round corner. . 89

List of Tables

6.1 Measured beam current in the stable region of the cold field emission gun of the Hitachi S4800 for an emission current of 10 μA and 20 μA. . . 24

8.1 Normalized measured EBIC signals for different electron beam energies of a ground sample and an HF etched sample. The x-position is 10 µm. . 60
8.2 Normalized simulated EBIC signals for different surface recombination rates. The electron beam energy is 20 keV and the x-position is 10 µm. . 60

9.1 List of designs investigated 62
9.2 Sample description and acronyms. 68
9.3 Extracted diffusion lengths from measurements with a beam current of 200 pA and 800 pA. 70

Chapter 1

Introduction

Even though, the topic of transport porperties of charge carriers in semiconductors is already very old, it is still of utmost interest. In fact, the knowledge of charge carrier transport in semiconductor devices gets more and more important, as the quality of the semiconductor material is improved and the demands on device performance are increased. The higher the quality that bulk material attains, the more effort should be put in understanding the transport and recombination processes at interfaces and surfaces. [1]–[3] One critical parameter influenced by recombination and generation procresses is the dark current in semiconductor devices, which increases with increasing trap density [4], [5]. Another area of interest are crystalline solar cells. Their performance is strongly dependent on recombination in the bulk as well as at the surface [6], [7]. Even though this work will focus on silicon based devices, also in other semiconducting materials like GaN based electronic and opto-electronic devices, transport properties are critical to the functionality [8], [9]. Because of their impact on device characteristics and performance, the knowledge about defects and their influence on carrier transport and recombination is essential for manufacturing process control [10], [11].

There are several ways to measure the minority carrier lifetime and surface recombination rate of wafer substrates. A short introduction to different methods will be given in this work in Chapter 3. But, as pointed out before, one also has to take into account the influence of the process steps during device production. This makes investigations of the transport behavior on device level important. Information about the spatial distribution of defects and recombination centers is of particular interest in semiconductor process as well as in device developement. Electron beam induced current (EBIC) is a measurement method suitable to characterize the transport behavior in processed semiconductor devices including a *p*-*n* junction or a Schottky junction. [12], [13] It can be used to locate regions with high recombination and to measure the minority carrier diffusion length and surface recombination rates. [14]–[16]. Other applications of EBIC are to identify defects and the use for failure analysis of semiconductor devices [17]–[19] and solar cells [20], [21].

In this work, EBIC was used to characterize photodiodes fabricated in a silicon Complementary Metal Oxide Semiconductor (CMOS) process. Typically in photodiode characterization, the photocurrent is measured as a function of bias voltage, light intensity, wavelength, and temperature. The photocurrent is an integral response of the diode to the measurement parameters. In contrast, an EBIC measurement produces a spatially resolved map of the diode's response. Additionally to experimental measurements, a TCAD model is introduced, reproducing the measurement results. The advantage of using a TCAD environment over analytic models [16], [22] is that it can handle complex geometries, high injection conditions, and interface charges.

In the following chapters, first the fundamentals of carrier transport in semiconductors are described, followed by a short introduction to measurement methods of the transport parameters. A main focus of this work is the use of EBIC. In the theory section a stronger focus is put on this method and related theory background. The main interaction of electrons and matter is described, as well as the principle of *p*-*n* junctions, then the measurement method itself will be introduced in more detail. In Chapter 7 basics about TCAD simulation and the developed EBIC TCAD environment are introduced.

Chapter 8 describes rather simple step-junction structures that were manufactured to calibrate the measurement set up as well as the simulation environment. The structures, were produced using large area epitaxial deposition of *p*- and *n*-doped layers on top of a highly *p*-doped substrate. The influence of different measurement and device parameters such as the *n*- and *p*-doping concentration, surface quality, electron beam energy and diode biasing are shown. Finally the EBIC experiments are compared to EBIC TCAD simulations.

In Chapter 9, a dedicated test chip is presented. The influence of wafer processing in a high voltage 0.35 μm CMOS process on transport parameters was shown. The size of the structures is chosen to be suitable for diffusion length extraction. The structures were processed on different substrate materials. Additionally to substrate material, different *n*-well implantations and diffusion wells were processed and compared. The main focus is put on the influence of the surface recombination rate on the EBIC signal, as this can be the dominant recombination process in very high quality bulk materials. To do this, two different designs, one including an additional surface passivation were compared to each other.

Chapter 2

Carrier transport in semiconductors

In semiconductors there are two main transport mechanisms: carrier drift and carrier diffusion. In this chapter both mechanisms will be described. Additionally to the carrier transport, also generation and recombination processes are important to explain the current in a semiconductor.

2.1 Carrier drift

The carrier drift is the movement of charge induced by an external electric field. The electric field forces the electrons as well as the holes to move with an average velocity called drift. In the semi-classical description, in an electric field the hole (electron) accelerates in the crystal until it scatters from a defect or a phonon. It scatters in a random direction and then gets accelerated again by the electric field. This leads to an average drift velocity of the charged particles. The net drift leads to a drift current for electrons and holes respectively, whose densities are defined as follows.

$$\vec{J}_{p,\mathrm{drift}} = e\mu_p p\vec{E} \tag{2.1}$$

$$\vec{J}_{n,\mathrm{drift}} = e\mu_n n\vec{E} \tag{2.2}$$

The net movement of the holes is in the same direction as the applied electric field and the movement of the electrons in the opposite direction. By convention, the hole and the electron drift current is in the direction of the electric field. The proportionality factor between the hole or electron drift velocity and the electric field is the hole and electron mobility $\mu_{p,n}$ respectively. The electron and hole mobilites are dependent on the doping concentration. In silicon, at low doping concentrations, the electron mobilty is about 1500 cm^2/V s and the hole mobility is about 500 cm^2/V s.

The total drift current density is the sum of the electron and hole drift current densities shown in Equation 2.1 and Equation 2.2 because both carrier types contribute to the current.

$$\vec{J}_{\mathrm{drift}} = e(\mu_n n + \mu_p p)\vec{E} \tag{2.3}$$

The conductivity and its inverse, the resistivity, are important parameters of a semiconductor and are calculated from the carrier mobilities and the concentrations. [23]

$$\rho = \frac{1}{\sigma} = \frac{1}{e(\mu_n n + \mu_p p)} \tag{2.4}$$

2.2 Carrier diffusion

The second transport mechanism, in addition to the drift current, is the carrier diffusion due to a carrier density gradient. According to Fick's law, carriers move from a region with high concentration to a region with lower one. This flow results again in a current, defined as diffusion current. In Equation 2.5 and Equation 2.6 the the diffusion current density for holes and electrons respectively are,

$$\vec{J}_{n,\text{diff}} = eD_n \nabla n \tag{2.5}$$

$$\vec{J}_{p,\text{diff}} = -eD_p \nabla p \tag{2.6}$$

$D_{n,p}$ is the electron (hole) diffusion constant. As the mobility indicates how well a carrier moves due to a electric field, the diffusion constant indicates how well the carrier diffuses. The relationship between the diffusion constants and the mobilities is given by the Einstein relation.

$$D_{n,p} = \frac{kT}{q} \mu_{n,p}. \tag{2.7}$$

The total current density is the sum of the diffusion current density terms and the drift current density terms. For the three dimensional case this yields [23]:

$$\vec{J} = en\mu_n \vec{E} + ep\mu_p \vec{E} + eD_n \nabla n - eD_p \nabla p. \tag{2.8}$$

2.3 Carrier recombination and generation

Carrier generation is the process where electrons and holes are created while recombination is the process where they are annihilated. In thermal equilibrium the electron and hole concentration is not dependent on time, thus the generation and recombination rates are the same.

Generation

Any external excitation of the semiconductor, like a light flux or very high electric fields, like in space charge regions, lead to a generation of electron hole pairs. The generated carriers are called excess carriers. [23]

Recombination

Recombination can happen in single or multiple steps. Because of energy conservation, the energy difference between the initial and final state of the electron has to be released during the recombination process. One has to distinguish between different recombination processes. On the one hand there is band to band recombination, where we can further distinguish between two processes. One, where energy is released by the emission of a photon, called radiative recombination and one, were the energy is transfered to a third electron or hole, called Auger recombination. On the other hand trap-assisted recombination is possible, also called Shockley-Read-Hall recombination where the energy is released through one or several phonons which are emitted. In this mechanism an excited electron binds with a trap state, which is an energy level inside the band-gap caused by a foreign atom or a defect. One way to describe this mechanism

is a two step process were the electron recombines with a hole in the valence band in a second step. Another description of the same process assumes that the electron and the hole meet in the trap level and recombine there. A schematic image of these processes is shown in Figure 2.1. [24]

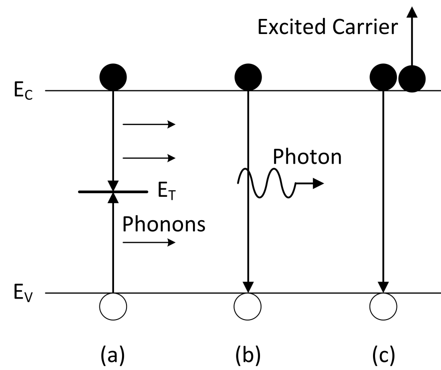

FIGURE 2.1: Different recombination mechanisms: (a) Shockley-Read-Hall recombination, (b) radiative recombination and (c) auger recombination.[25]

2.4 Lifetime and diffusion length

Two very important parameters giving information of the quality of a semiconductor material are the carrier lifetime and the carrier diffusion length. The lifetime is separated into two general categories, the generation lifetime and the recombination lifetime. The generation lifetime occurs when there is a lack of carriers as for example in a reverse-biased space charge region. The generation lifetime τ_g is then defined as the time it takes that an electron-hole pair is generated. For this work the recombination lifetime τ_r is the more interesting parameter. It defines the time it takes until an electron-hole pair is recombined again. Another distinction is made when the recombination or generation occurs at the surface. In this case they are called surface recombination and generation rate (commonly also called velocity because of their unit). In practice it is difficult to distinguish between surface recombination/generation and bulk recombination/generation because they appear simultaneously. Because of this, most measurement methods give an effective lifetime, consisting of a surface and a bulk contribution. [1]

2.4.1 Recombination lifetime

For the following explanation, a p-type semiconductor is used where the minority carriers are electrons. Similar formulas can be defined for the n-type case. The three different recombination mechanisms go along with different contributions to the overall recombination lifetime and will be investigated here in more detail.

As already stated above, the SRH recombination is a trap assisted recombination process with deep-level traps caused by impurities. It is characterized by the trap density N_T, the trap energy level E_T, the thermal velocity v_{th} and the capture cross

sections for electrons and holes σ_n and σ_p. In Equation 2.9 the Shockley-Read-Hall lifetime is given.

$$\tau_{\rm SRH} = \frac{\tau_p(n_0 + n_1 + \Delta n) + \tau_n(p_0 + p_1 + \Delta p)}{p_0 + n_0 + \Delta n} \tag{2.9}$$

p_0 and n_0 are the equilibrium hole and electron densities, τ_p and τ_n the hole and electron lifetimes and Δn and Δp are the excess carrier densities. In Equation 2.10 and Equation 2.11 the definitions for n_1, p_1 and τ_n, τ_p are shown.

$$n_1 = n_i e^{(E_{\rm T} - E_{\rm i})kT}; \qquad p_1 = n_i e^{-(E_{\rm T} - E_{\rm i})kT} \tag{2.10}$$

$$\tau_p = \frac{1}{\sigma_p v_{\rm th} N_{\rm T}}; \qquad \tau_n = \frac{1}{\sigma_n v_{\rm th} N_{\rm T}} \tag{2.11}$$

The radiative lifetime is inversely proportional to the carrier density. Because it is a band-to-band transition, electrons and holes must be present at the same time and k-state. The radiative lifetime is:

$$\tau_{\rm rad} = \frac{1}{B(p_0 + n_0 + \Delta n)} \tag{2.12}$$

with B as the radiative recombination coefficient.

Because of the fact that in Auger recombination three carriers are involved the Auger lifetime is inversely proportional to the square of the carrier density. In (2.13) the auger recombination lifetime is shown for a p-type semiconductor with C_p as the Auger recombination coefficient.

$$\tau_{\rm Auger} = \frac{1}{C_p(p_0^2 + 2p_0\Delta n + \Delta n^2)} \tag{2.13}$$

The total recombination lifetime in a device is a combination of the SRH recombination, the radiative recombination and the Auger recombination.

$$\tau_{\rm r} = \frac{1}{\tau_{\rm SRH}^{-1} + \tau_{\rm rad}^{-1} + \tau_{\rm Auger}^{-1}} \tag{2.14}$$

How big the influence of the single recombination processes is, is dependent on the material and its bandgap. The SRH recombination appears in every semiconductor because it only needs impurities or defects. Radiative recombination on the other hand plays almost no role in indirect bandgap semiconductors like silicon. Auger recombination occurs in direct and indirect bandgap semiconductors but requires either a high doping concentration or a high excess carrier density. It is the dominant effect at high injection levels and for semiconductors with narrow bandgap.

Surface recombination rate

As already stated earlier, not only bulk recombination takes place but also recombination at the surface or at interfaces. Similar to the bulk SRH recombination lifetime with the unit [cm^{-2}s^{-1}], also a SRH surface recombination is given by:

$$S = \frac{s_n s_p (p_{0\mathrm{s}} + n_{0\mathrm{s}} + \Delta n_\mathrm{s})}{s_n (n_{0\mathrm{s}} + n_{1\mathrm{s}} + \Delta n_\mathrm{s}) + s_p (p_{0\mathrm{s}} + p_{1\mathrm{s}} + \Delta p_\mathrm{s})} \tag{2.15}$$

with $s_{n,p}$ as the surface recombination rate for electrons and holes in [cm/s], the carrier densities at the surface and N_it as the interface trap density.

$$s_n = \sigma_{n\mathrm{s}} v_\mathrm{th} N_\mathrm{it}; \qquad s_p = \sigma_{\mathrm{ps}} v_\mathrm{th} N_\mathrm{it} \tag{2.16}$$

For device purposes reasonable values for S are between 10^3 to 10^7 cm/s. Below 10^3 cm/s bulk recombination becomes dominant while above 10^7 cm/s the recombination rate at the surface is essentially the same with the rate of carriers arriving at the surface being defined by the thermal velocity v_th of the carriers [26].

In measurements most of the time a so called effective recombination lifetime is measured that is a combination of the bulk recombination lifetime and the surface recombination rate. There ate many methods measuring the recombination lifetime. These will be explained in Chapter 3. [1]

A parameter related to the carrier lifetime is the diffusion length. It defines the distance a carrier will diffuse before it recombines. The diffusion length for electrons and holes respectively is calculated from the diffusion coefficient and the carrier lifetime. [24]

$$L_n = \sqrt{D_n \tau_n} \tag{2.17}$$

$$L_p = \sqrt{D_p \tau_p} \tag{2.18}$$

2.5 Continuity equation

The rate of change of the carrier concentrations with time is the difference between the incoming and outgoing carrier flux (drift and diffusion current) described above minus the recombination and plus the generation. This is described by the continuity equations for holes and electrons and is shown in Equation 2.19 and Equation 2.20 respectively. [24]

$$\frac{\delta p(x,y,z,t)}{\delta t} = -\frac{1}{q} \nabla \cdot \vec{J}_p(x,y,z,t) + G_p(x,y,z,t) - R_p(x,y,z,t) \tag{2.19}$$

$$\frac{\delta n(x,y,z,t)}{\delta t} = \frac{1}{q} \nabla \cdot \vec{J}_n(x,y,z,t) + G_n(x,y,z,t) - R_n(x,y,z,t) \tag{2.20}$$

Solving the continuity equation for electrons gives:

$$\frac{\partial n}{\partial t} = D\nabla^2 n + G(\vec{r}, t) + \frac{n - n_0}{\tau}. \tag{2.21}$$

For a time independent delta function the generation term is:

$$n - n_0 = \frac{G_0}{4\pi r} \exp\left(-\frac{r}{\sqrt{D\tau}}\right). \tag{2.22}$$

From the point the carriers are generated, they decay exponentially in the form $\exp(-r/L)$ and the diffusion length can be extracted from this decay.

Recombination can be described by the relaxation time approximation:

$$R_p = \frac{\Delta p}{\tau_p} \tag{2.23}$$

$$R_n = \frac{\Delta n}{\tau_n} \tag{2.24}$$

in steady state $\mathrm{d}n/\mathrm{d}t = 0$ and if the current density is uniform, the divergence of J is zero and

$$G_n = R_n = \frac{\Delta n}{\tau_n}. \tag{2.25}$$

In the following chapter it is shown how this relations can be used to determine the minority carrier lifetime and the diffusion length with various different measurement methods.

Chapter 3

Measurement of semiconductor transport properties

The knowledge about the transport behavior of minority carriers, explained in the previous section, is of great interest in device and process development in the CMOS industry. A short introduction to different measurement methods dealing with the determination of minority carrier lifetime and diffusion length is presented here. Two basic approaches to measure minority carrier lifetime can be distinguished. The first is a steady state approach, where a steady state generation rate of electron hole pairs with known value is maintained. In steady state, the recombination and generation rate must be the same. Using this fact in combination with the definition of generation and recombination rate introduced earlier, the minority carrier lifetime can be calculated. It is necessary to measure the absolute excess carrier density and the generation rate. To do so the photo conductance, the photon flux, the fraction of absorbed photons and the thickness of the wafer must be known. Furthermore, the knowledge of electron and hole mobility is necessary. The basic relation for measuring the effective lifetime assuming steady state is:[27]

$$\tau_{\mathrm{eff,steady}}(\Delta n) = \frac{\Delta n}{G}. \tag{3.1}$$

To satisfy this approximation, the excess carrier density Δn must be in equilibrium with the light density in every point and time of the measurement. Thus only short lifetimes can be measured in this mode. To measure longer lifetimes a quasi transient method has to be used. Here short light pulses are used and Equation 3.1 changes to:[28]

$$\tau_{\mathrm{eff,trans}}(\Delta n) = -\frac{\Delta n}{\mathrm{d}\Delta n/\mathrm{d}t}. \tag{3.2}$$

The advantage of this method is that it is not necessary to measure the light intensity.

The second approach, is the transient decay mode. Here the generation of charge carriers is stopped abruptly and the rate at which carriers disappear (recombine) over time is: [27]

$$\frac{\mathrm{d}n}{\mathrm{d}t} = -\frac{\Delta n}{\tau}. \tag{3.3}$$

The advantage of transient methods is that they directly reflect the speed of the recombination process. [29] Another advantage is that no absolute values of the excess carriers are necessary but only relative measurements. The disatvantages, compared to steady state approaches, are first, that fast electronics for signal processing are necessary when measuring short lifetimes and second, a light pulse with a very steep cut-off ramp is required. [28]

In transient as well as in steady state methods, the excess carrier concentration must be known. [27]

There are several parameters affecting the measurement results. One main parameter is, of course, the excess carrier density [29]. Another big influencing factor is the microstructure of the sample surface (its quality). In most techniques the lifetime and the surface recombination rate can not be separated in measurement and the measured parameter is called effective lifetime:

$$\frac{1}{\tau_{\text{eff}}} = \frac{1}{\tau_{\text{bulk}}} + \frac{2s}{d} \tag{3.4}$$

here d is the wafer thickness, τ_{bulk} the bulk recombination lifetime and s the surface recombination rate. By using a surface passivation, the surface recombination can be neglected. One way to measure the surface recombination of semiconductor substrates is to use wafers with different thickness but with same bulk and surface properties. Also already processed wafer should be characterized, because also the processes performed on the wafer will influence surface and bulk properties. Another important parameter is the carrier injection level. The lifetime determined in high and low carrier injection regimes can differ from each other. At lower excess carrier densities up to 3×10^{16} cm^{-3}, Auger and band to band recombination is dominant. With increasing excess carrier density, SRH recombination takes over. [27]

3.1 Measurement Methods

One can distinguish between measurement methods of unprocessed wafers and already processed ones. In the case of semiconductors substrate characterization a number of contactless measurement methods are available. Here a short summary of these methods is shown.

Contactless methods

Common transient measurement methods are microwave reflection photoconductive decay (µPCD) [7] [30] [31], resonance-coupled photoconductive decay (RCPCD) [7] [32] and Time resolved photoluminescence (TRPL) [33]. In these measurements the excess carrier density and the excess conductivity decay are measured. The transient decay rate is measured after a pulse excitation. In photoconductive decay methods like RCPCD and µPCD the transient photoconductive decay $\Delta\sigma(t)$ is measured. A common approximation in these measurements are constant mobilities during the measurement. This is adequate at low level injection but not at higher injection levels. [7] In µPCD a microwave is irradiated onto the silicon wafer and additionally a laser pulse is used to inject excess carriers. This increases the conductivty and results in an increased intensity of the reflected microwave wich is detected. Additionally, the excitation laser power is measured to determine the concentration of injected carriers. [31] In RCPCD

the sample is placed at a variable height above an antenna, forming a coupled antenna array. The primary electromagnetic waves are absorbed and reradiated by the sample in phase with the driving antenna. Again, a pulsed light source is used to generate excess carriers. The intensity of the reradiated electro magnetic waves is a function of the dark and excess carrier concentration generated by the light source. The antenna absorbs the photo-generated electro-magnetic waves and transforms the energy in an AC voltage. Likewise the photoconductive decay is recorded. [7], [32] In quasisteady-state photoconductive techniques, like quasi-steady-state photoconductivity (QSSPC) [7][28] and quasi-steady state photoluminescence technique (QSSPL) [34][35], a very long duration flash lamp is used to photo-excite carriers. The lamp duration should be much longer than the lifetimes measured. The wafer is placed on an insulated platform under a coil that is inductively coupled to the sample. The photoconductive signal of the sample is coupled through the coil into a bridge circuit and converted to an electrical signal that is proportional to the photoconductivity [7]. Additionally, the output flux of the flash lamp during the measurement is recorded. Values measured either from a steady state technique or a transient measurement can vary significantly due to fundamental differences in carrier recombination. The combination of QSSPC and µPCD gives a very powerful unified lifetime measurement. Two illumination sources are used in this case: a pulsed source and a steady state source. Short laser pulses induce small perturbation pulses of excess carriers that decay on the background of the steady-state excitation. [36] [37]

The quasi steady-state photoluminescence records simultaneous the time modulated optical irradiation intensity and the corresponding photoluminescence intensity as a function of time. The effective minority carrier lifetime can be extracted from the time shift between the maxima of irradiation and luminescence intensities. This is only valid under the approximation that the lifetime is not dependent on the injection level. [34] [35]

The big advantage of the microwave phase shift technique [38] [39] is that one can measure the bulk lifetime and the surface recombination rate separately by varying the modulation frequency of the exciting light. The sample is excited by a harmonic modulated laser light, thus, the injection level is quasi constant during the measurement. The phase shift between the modulation and the microwave reflected by the sample is measured. It is a function of the bulk lifetime τ_b, the surface recombination velocity at the front, S_f, and backside, S_b, of the sample, the diffusion constant D, the sample thickness W, the absorption coefficient α and the modulation frequency F:

$$\Phi = f(\tau_p, S_f, S_b, D, W, \alpha, F). \tag{3.5}$$

The sample thickness, the absorption coefficient, the modulation frequency and of course the measured phase shift are known. The bulk lifetime and the surface recombination velocity can be deduced out of the phase shift when using at least three different modulation frequencies. [38]

Methods with contact

To measure the lifetime from diode characteristics the leakage current of area perimeter diode structures is investigated. Current voltage characteristics as well as capacitance voltage characteristics must be performed on structures with varying area and perimeter sizes. To obtain the recombination lifetime the forward current has to be separated

into the area current and the peripheral current. The area component can further be split up in the bulk recombination and the diffusion current density. [40]

The lifetime of devices can also be measured by measuring the impedance at different frequencies. By measuring under reverse and forward bias conditions, the generation and recombination lifetimes respectively are determined. For the measurement, an AC signal with varying frequency and an amplitude lower than the thermal voltage is superimposed across the sample together with a DC bias. [41]

In the open circuit voltage decay measurement, the diode is forward biased and at time $t = 0$ the circuit is opened. Due to the recombination of excess carriers the voltage decays and by a time dependent measurent of the voltage decay the time dependent decrease of carrier density is measured. The recombination lifetime can be evaluated out of the slope of the voltage decay and is an effective lifetime. [25]

The reverse recovery measurement works in two basic regimes. First, the current is abruptly switched from forward to reverse current and second, the current is gradually changed. A forward current flows through the diode for $t < 0$. Excess carriers are injected into the quasi neutral regions, making the device impedance very small. At $t = 0$ the current is switched from forward to reverse direction. The diode voltage is proportional to the logarithm of the excess carrier density at the space charge region edge. The voltage hardly changes during this period and the diode remains forward biased although the current has reversed direction. The excess carrier density decreases during the reverse current phase because they are swept out of the device and recombine. At the edges of the space charge region the excess carrier minority densities are almost zero and the diode becomes zero biased. The voltage approaches the reverse bias voltage and the current approaches the leakage current. [25]

The disadvantage of current-voltage characteristic based methods is that ideal behavior is expected, which is very often not the case in real devices. In Optical Beam Induced Current (OBIC) [42], a laser beam is scanned across the structure instead. The light is absorbed, and electron hole pairs are generated which diffuse to the space charge region of the Schottky or *p-n* junction. There the carriers are collected. The use of different wavelengths enables the possibility to generate excess carriers in different depths of the device. [42] A very similar technique is Electron Beam Induced Current (EBIC). In EBIC an electron beam is scanned across the structure instead of a laser beam. EBIC will be explained more intensively later, as it is the method used within this work. Both methods have their advantages and disadvantage. One advantage of OBIC over EBIC is that oxides used in CMOS processes are transparent for light but not for electrons. The disadvantage of OBIC is the limited resolution compared to EBIC.

Chapter 4

Electron matter interaction

For an understanding of the EBIC method, the interaction of electrons with matter must be understood and will be introduced briefly in this chapter. For more detailed information one can refer to [43]–[45]. The elementary atomic interaction processes between electrons accelerated at a specimen include elastic and inelastic scattering and involve the complete electron diffusion and interaction process due to a gradual energy loss of the primary and secondary electrons along their path through the material. The finite range of the electrons depends on the electron beam energy and the specimen density. The most important interaction processes and the resulting signals are shown in Figure 4.1.

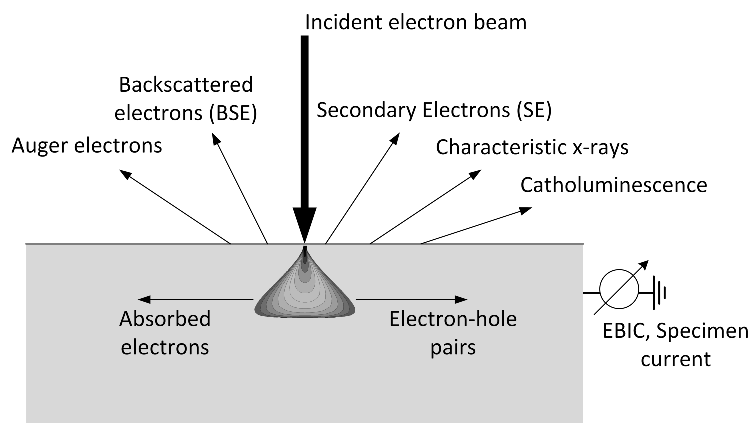

FIGURE 4.1: Schematic showing the interaction between incident electron beam and sample.

The elastic and inelastic scattering processes in the specimen result in zig-zag trajectories of the primary electrons until they stop because of gradual deceleration or because they have left the specimen again. Electrons that leave the sample are separated into Secondary Electrons (SE), Backsacttered Electrons (BSE) and Auger Electrons. Each primary electron transfers its energy to many other electrons through inelastic scattering. The electrons near the surface with sufficient energy to overcome the work function leave the specimen as secondary electrons. BSE are primary electrons which decelerate because of single or multiple energy losses and multiple scattering through large angles and leave the sample again. Auger electrons and characteristic x-rays are generated due to the ionization of inner shells. The de-excitation energy is released in form of an electron or an x-ray which leaves the specimen with a characteristic energy which can be used for elemental analysis. Due to the low energy of SE and Auger electrons, they

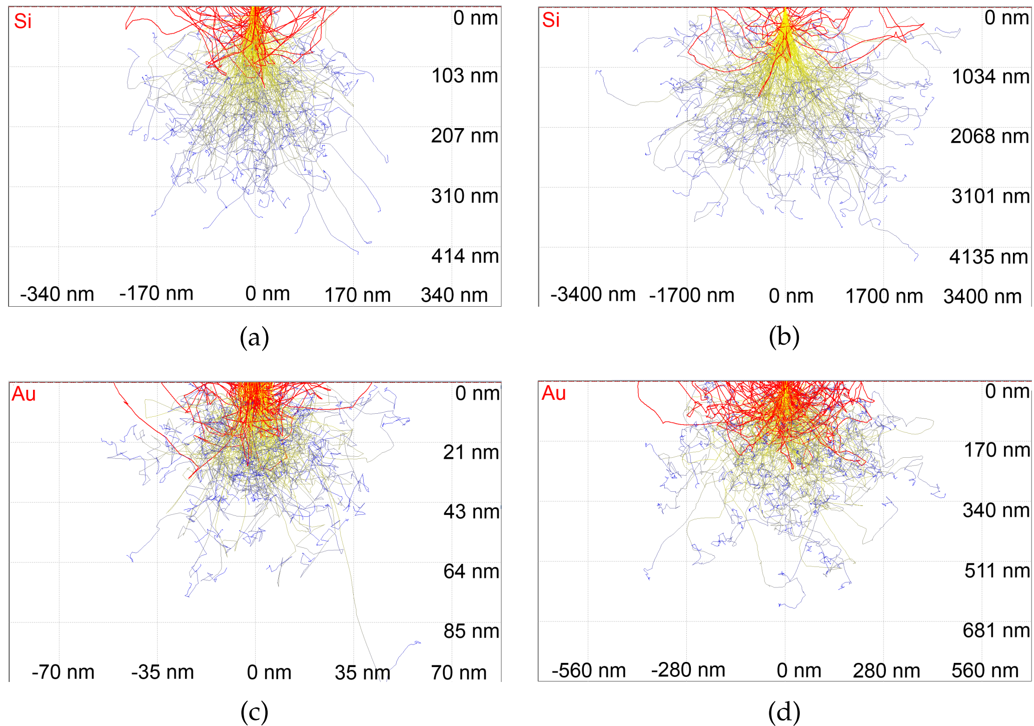

FIGURE 4.2: Monte Carlo simulations of electron trajectory paths using Casino [46] for Silicon and Gold. (a) Silicon the Electron beam energy is 5 keV, (b) Silicon and 20 keV, (c) Gold and 5 keV and (d) Gold and 20 keV.

are very sensitive to further scattering and only electrons from surface near regions, in the order of a few nanometers, can leave the specimen. In addition to the primary electrons, also BSE can generate SE and Auger electrons resulting in a component to the SE signal depending on the backscattering coefficient and decreasing the resolution. In the case of electrons interacting with semiconductors, inelastic scattering results in the generation of electron-hole pairs. If there is an electric field the charge carriers can be are separated and a current flows. This is the so called Electron Beam Induced Current (EBIC). The specimen current results from absorbed electrons which remain in the sample. The biggest part of the primary electron energy that is lost because of inelastic scattering results in heat or phonons. [43]

The vertical and lateral extension of the interaction volume depends on the, material and its atomic number Z, the electron beam energy and the diameter of the spot at the surface of the sample. Because of the angular distribution of the scattering events, beam broadening occurs normal to the electron beam. The broadening is increasing with increasing sample thickness. This leads to a higher resolution in surface near regions compared to deeper regions. When increasing the beam current at a fixed beam energy by increasing the aperture width, the probe diameter is increased and the resolution is decreased. Thus, a trade-off between high beam current and small probe diameter has to be found. The trajectories of the electrons through the specimen can be simulated using a Monte Carlo based simulator such as CASINO [46]. In Figure 4.2 the simulated electron trajectories using 200000 electrons and a beam radius of 10 nm are shown for a 5 keV and a 20 keV electron beam striking a silicon and a gold surface. For materials with low Z, the majority of carriers gets scattered through small angles resulting in less broadening. In high Z materials like gold on the other hand, scattering is in higher angles and the electron trajectory path is broader.

In order to describe the energy loss of a primary electron as it passes through the sample, it is assumed that the energy transfer due to Coulomb interactions to atomic electrons is much smaller than the energy of the incident electron. A sequence of collisions leads to a continuous slowing down of the primary electron. The mean energy loss of an electron along its path can be described by the stopping power or Bethe-loss. [43]

4.1 Electron beam damage and surface charging

The interaction of electrons with a sample leads to damage, charging, and heating of the sample. It is very important to be aware of these effects in order to interpret the measured signals in electron microscopy. In this chapter an overview and a short introduction of damaging and charging effects are given. More detailed information ca be found in [43]–[45]. In general it can be stated that organic materials are more susceptible to electron beam damage. But also inorganic materials suffer beam damage and this has to be taken into account. The different effects can be separated into damage produced due to elastic scattering and due to inelastic scattering. Not all effects mentioned are contributing to the investigations done in this work and are listed for completeness.

4.1.1 Beam damage due to elastic scattering

If the energy exceeds a displacement energy, depending on the specimen material, high angle elastic scattering can lead to atomic displacement, disturbing the crystal structure. This effect, called the knock-on process, is mainly seen in transmission electron microscopes (TEM) as the used beam energy in SEMs is not high enough. Primary energies starting from 100 keV are necessary for atomic displacement. A similar effect is electron-beam sputtering. High angle elastic scattering at an atom near to the surface can lead to a sputtering effect. Again this effect is mainly observed in TEM investigations because of the higher beam energies used. [43]–[45]

4.1.2 Beam damage due to inelastic scattering

Inelastic scattering involves interaction between incoming electrons and particles with a similar mass. Energy is transferred in the process. A big amount of this energy results in heating of the specimen and increases the local temperature. Another effect related to inelastic scattering is ionization damage, also called radiolysis. In this case the energy released due to electron excitation changes the electronic and atomic configuration. While for elastic displacement high energies are necessary, inelastic displacement is more dependent on the current density. The mechanisms discussed now have a higher relevance for this work and their influence will be discussed in the experimental section. The first mechanism concerns hydrocarbon contamination. When hydrocarbon molecules on the surface of a sample are polymerized by the electron beam, they can contaminate the sample surface. The thickness of the contamination layer increases with irradiation time because of the low surface mobility of hydrocarbons. The issue of beam induced contamination decreased a lot due to improvement of pressure and hydrocarbon content in the chamber, but is still not eliminated completely. The specimen itself can act as a local source of hydrocarbon, produced during sample preparation or storage in air. The last, but very important effect discussed, is the electrostatic charging

of insulating layers due to the electron beam. This process involves both, elastic and inelastic scattering and thus depends on the backscattering coefficient η and the yield for secondary electrons δ. Depending on the total electron emission yield σ, which is the sum of backscattering coefficient and yield for secondary electrons, $\sigma = \eta + \delta$, the surface potential of an insulating specimen will be positively or negatively charged. Depending on the primary electron beam energy E, two crossover energies where σ is 1 are measured. In these points no charging occurs. The first crossover is at very low energies about 100 to 200 eV and thus not of interest in our investigations. For the case of $\sigma > 1$ the sum of backscattered and secondary electrons per unit time is bigger than the number of primary electrons hitting the sample. This leads to a positive charging of the sample surface. This state is stable because secondary electrons with low energy can return to the surface, preventing too big surface potentials. If $\sigma < 1$ more electrons hit the sample than leave the sample as secondary or backscattered electrons and a negative charge is formed. In contrast to the positive charge which is only a few volts, negative charging can reach a few kilovolts. In this work, samples with insulating layers of thickness t on top of conductive substrates are of interest. The same conditions, as explained before, are true if the electron range $R(E) < t$. When $R(E) > t$, minority charge carriers are generated through the hole insulating layer resulting in a surface potential between surface and substrate. This results in an electron beam induced current.[43]–[45] In the following chapters it will be shown that all these effects influence the measured EBIC signal and have to be kept in mind when interpreting measurement results.

Chapter 5

p-n Junctions

In the preceding chapter the generation and the transport of carriers in semiconductors was explained. In this chapter a short summary about the theory of *p-n* junctions and carrier transport in *p-n* junction devices is given. All investigations done within this work are based on silicon *p-n*-junction structures. At the interface of a *n*- and a *p*-semiconductor, a diffusion current of holes to the *n*-side and electrons to the *p*-side occurs because of concentration gradient. Because of this diffusion process, a region that is depleted of mobile carriers is formed. This region is called space charge region or depletion region. The net charge in the depletion region, results in an electric field that causes a drift current, which opposes the diffusion current. In the case of thermodynamic equilibrium, with no applied bias, the drift current and the diffusion current are the same and no net current flows. Because of the difference in chemical potential of the *n*- and *p*-type semiconductor an internal potential, the so called, built-in potential is formed. This built-in potential equals the difference of the Fermi level on the *p*- and *n*-side relative to the band edges. Outside of the depletion region, the *n*- and *p*-type regions are charge neutral. The built in potential is [23], [47]:

$$V_{\mathrm{bi}} = V_{\mathrm{th}} ln \frac{N_D N_A}{n_i^2} \tag{5.1}$$

with $V_{\mathrm{th}} = kT/q$ being the thermal voltage and N_a and N_b the acceptor and donor concentrations.

$$\frac{d^2\Phi}{dx^2} = -\frac{\partial \mathcal{E}}{\partial x} = -\frac{\rho}{\epsilon_s} = -\frac{q}{\epsilon_s}(p - n + N_D^+ - N_A^-). \tag{5.2}$$

The relation shown in Equation 5.2 is called the poisson equation and shows the relation between the electric potential Φ, the electric field $\mathcal{E}$ and the charge density ρ. Here the charge density ρ is expressed by the electron and hole density n and p and the densities of ionized dopants N_D^+ and N_A^-. ϵ_s is the permittivity of the semiconductor. Assuming that the depletion region has well defined edges and the *p-n* junction is abrupt following definition for the charge density profile is given.

$$\begin{aligned}
\rho(x) &= 0 & -x_p &\leq x \\
\rho(x) &= -qN_A & -x_p &\leq x < 0 \\
\rho(x) &= qN_D & 0 &< x \leq x_n \\
\rho(x) &= 0 & x &\geq x_n
\end{aligned} \tag{5.3}$$

Because all dopants are ionized, N_A and N_D are the dopant densities. The electric field can be calculated using the relation shown in Equation 5.2. Outside the depletion region the electric field $\mathcal{E}$ has to be zero. This fact is used as boundary condition for the calculation of the electric field.

$$
\begin{aligned}
\mathcal{E}(x) &= 0 & -x_p \leq x \\
\mathcal{E}(x) &= -\frac{qN_A(x+x_p)}{\varepsilon_r\varepsilon_0} & -x_p \leq x < 0 \\
\mathcal{E}(x) &= \frac{qN_D(x+x_n)}{\varepsilon_r\varepsilon_0} & 0 < x \leq x_n \\
\mathcal{E}(x) &= 0 & x \geq x_n
\end{aligned}
\tag{5.4}
$$

By integrating the electric field, the potential across the depletion region can be calculated. The depletion layer width can be calculated under the assumption of the afore mentioned full depletion approximation:

$$
W = \sqrt{\frac{2\varepsilon_r\varepsilon_0}{q}\left(\frac{N_A+N_D}{N_AN_D}\right)V_{\mathrm{bi}}} \tag{5.5}
$$

In Figure 5.1 a schematic showing the space charge distrubution, the electric field distribution and the potential variation of an abrupt *p-n* junction is shown in thermal equilibrium.

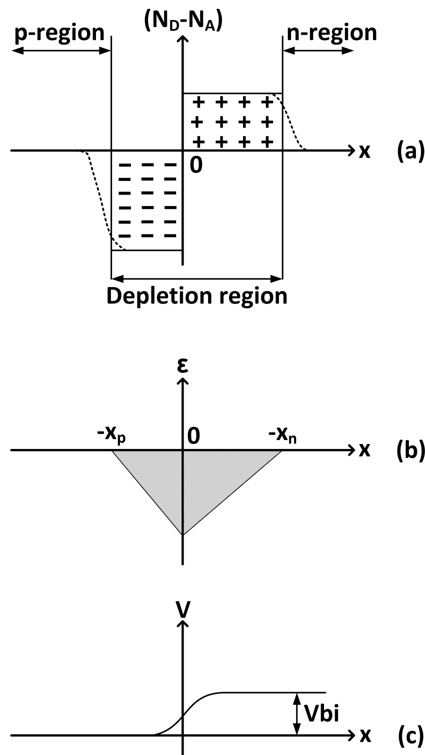

FIGURE 5.1: Abrupt *p-n* junction in thermal equilibrium. In (a) the space charge dirstribution, in (b) the electric field distribution and in (c) the potential variation is shown.[47]

Everything discussed so far is valid without an applied bias to the diode. If a bias is applied the balance between diffusion and drift current is destroyed. In a diode characteristic, one distinguishes between the forward, a positive bias applied to the cathode, and the reverse, a negative bias applied, regime. In the biased case the potential across the devices changes to the built-in potential minus the applied voltage. In the forward regime, the potential across the semiconductor decreases and so does the width of the depletion region. The minority carriers injected control the current and increase exponentially across the junction. In this case the drift current does not completely compensate the diffusion current anymore. In reverse direction, the space charge region width increases and the current saturates. Almost no current flows since the junction voltage is increased. It becomes larger than the built-in voltage and carriers are not able to cross the junction. The small negative current flowing in the reverse bias regime is due to minority carriers which are attracted by the electric field. [24], [48] Furthermore, the applied voltage is proportional to the difference of the quasi Fermi levels of the *n*- and *p*-type quasi neutral regions. In Figure 5.2 the biasing modes and the energy bands are shown schematically for no applied bias and for the forward and reverse bias regime. [24], [48]

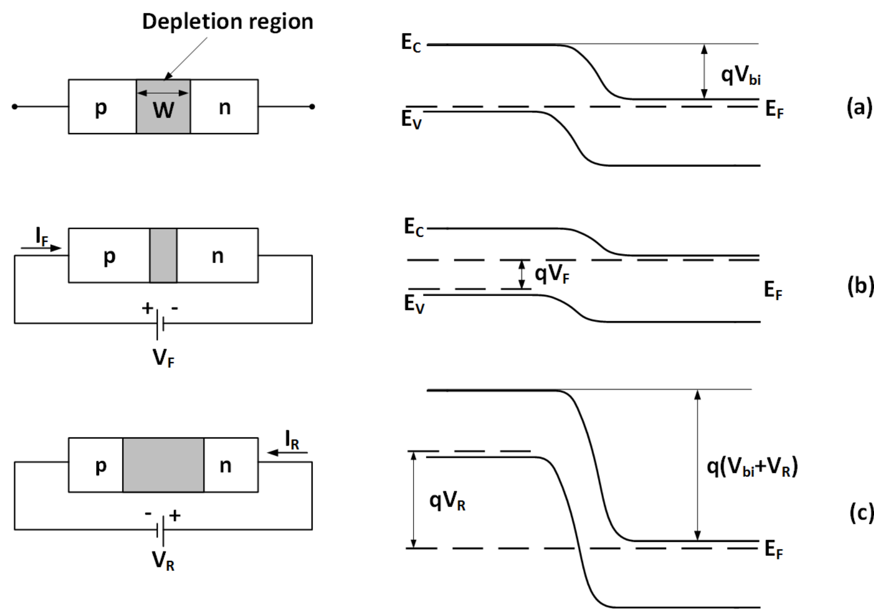

FIGURE 5.2: The biasing modes are shown schematically and the corresponding energy bands. In (a) without applied bias, in (b) forward bias and in (c) reverse bias.[47]

The total current of the ideal diode characteristic under the abrupt depletion layer approximation, the Boltzmann approximation, the low injection assumption and excluding generation current in the depletion layer is:

$$J = J_p + J_n = J_s\left(e^{qV/kT} - 1\right) \text{ with} \tag{5.6}$$

$$J_s = \frac{qD_p p_{n0}}{L_p} + \frac{qD_n n_{p0}}{L_n}. \tag{5.7}$$

Using the ideal diode equation several effects are neglected. Differences to the ideal behavior occur mainly because of surface effects, generation and recombination of carriers in the depletion layer, tunneling of carriers through the depletion width or the series resistance of the leads. Also the low injection condition is not valid in every case. The current resulting from generation in the depletion region is given by:

$$J_{\mathrm{gen}} = \frac{q n_{\mathrm{i}} W}{\tau_{\mathrm{eff}}} \tag{5.8}$$

τ_{eff} is the effective lifetime, depending on the bulk lifetime and the surface recombination rate and was already discussed in Chapter 2. The generation current is dependent on the depletion layer width and thus also on the applied voltage. Including this term to the ideal diode characteristic the reverse current is defined as:

$$J_{\mathrm{R}} = \frac{q D_p p_{n0}}{L_p} + \frac{q D_n n_{p0}}{L_n} + \frac{q n_{\mathrm{i}} W}{\tau_{\mathrm{eff}}}. \tag{5.9}$$

At room temperature the generation current will be dominant. But at sufficently high temperatures the diffusion current (first two terms) will take over. [47]

Everything discussed so far, supports the understanding of processes taking place in EBIC experiments. In the next chapter the methodology of EBIC measurements is presented, based on the theory introduced in the previous sections.

Chapter 6

EBIC measurement methodology

When the primary electrons of an electron beam hit a semiconductor, electron-hole pairs are generated by energy transfer from the primary electrons to electrons in the valence band, like explained in Chapter 4. This fact is used in electron beam induced current (EBIC) measurements. Under the condition that a built-in electric field exists such as within a Schottky diode or a *p-n* junction, the generated carriers get separated and can be collected. One has to distinguish two regions where generation takes place. First, generation inside the space charge region. In this case the generated carriers get separated immediately by the electric field and an electron-beam-induced current or charge-collection current can be measured. These carriers contribute to a very fast component to the EBIC signal. The second region, is outside of the space charge region. Here minority carriers have the possibility to diffuse to the space charge region. The delay due to the diffusion contributes as a slowly decaying component to the EBIC signal. The probability that a minority carrier reaches the space charge region before it recombines again is described by the minority carrier lifetime or the diffusion length. These parameters and the related recombination processes were already discussed in Chapter 2. How many electron-hole pairs are generated depends on the electron energy E. The mean number of electron-hole pairs produced per primary electron is: [43]

$$\overline{n} = \frac{(E - E_{\mathrm{th}})}{\overline{E}_{\mathrm{i}}}. \tag{6.1}$$

$\overline{E}_{\mathrm{i}}$ is the mean energy needed to generate a electron hole pair and E_{th} is a threshold energy because of any metal or insulation films on the surface that need to be penetrated by the electron beam before reaching the semiconductor. For silicon $\overline{E}_{\mathrm{i}}$=3.6 eV. The magnitude of the resulting current (EBIC) is: [43]

$$I_{\mathrm{EBIC}} = I_p(1 - \eta_{\mathrm{c}}) \left[\frac{(E - E_{\mathrm{th}})}{\overline{E}_{\mathrm{i}}} \right] \epsilon_{\mathrm{c}}, \tag{6.2}$$

with η_{c} being the backscattering coefficient describing the loss of electron-hole pair generation because of electron backscattering. I_p is the current of the incident electron beam and ϵ_{c} is the charge-collection efficiency, defining the fraction of generated charge carriers, which are collected by the electrodes.

In Figure 6.1 different measurement geometries are schematically shown. The junction, either a *p-n* junction or a Schottky junction, can be perpendicular (Figure 6.1 (a) and (b)) or normal (Figure 6.1 (c) and (d)) to the surface. In most applications, one deals with structures including both a vertical and horizontal junction. A schematic of the measurement of such a structure is shown in Figure 6.2.

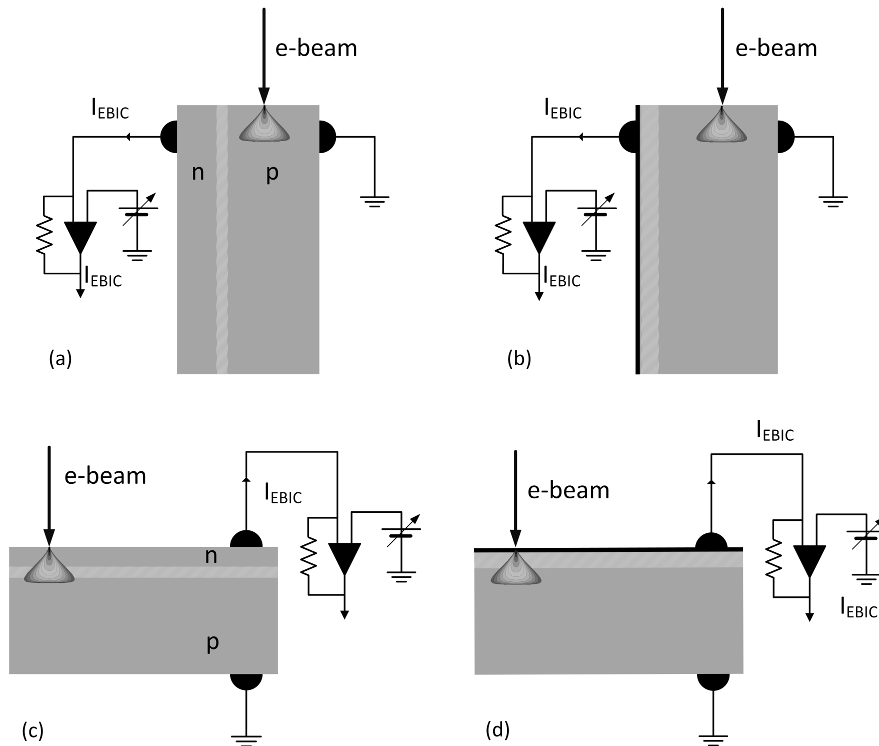

FIGURE 6.1: Different geometries used in EBIC measurements are shown. A junction perpendicular to the surface is shown for the case of a *p*-*n* junction in (a) and for the case of a Schottky junction in (b). A configuration with normal junction to the surface is shown in (c) for a *p*-*n* junction and in (d) for a Schottky junction. [43]

With electrical contacts on both sides of the junction the induced current can be collected and measured. The signal is then amplified by an operational amplifier and recorded as a function of position. It is important to choose a scan speed slow enough that the signal is not dependent on it anymore. This depends on the lifetime of the minority carriers in the investigated region. The longer the lifetime, the longer the dwell time at one position needs to be. Alternatively, a transient EBIC measurement can be made where a chopped beam is used to measure a time dependent EBIC signal at a fixed position [49], [50]. In this case, the beam has to be turned on long enough to ensure steady state condition. Standard EBIC measurements are done without biasing the diode configuration; even without applied bias, a current is flowing because of the built-in electric field of the junction. Nevertheless it is also possible to apply a bias to increase the electric field and enlarge the space charge region like in the case of reverse biasing a *p*-*n* junction.

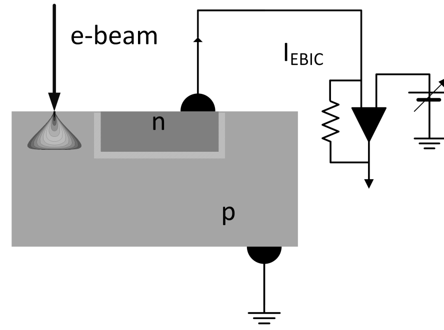

FIGURE 6.2: EBIC measurement geometry of a n-type well in a p-type substrate including a vertical and a horizontal junction.

6.1 Quantitative measurement of semiconductor parameters

The diffusion length L and the minority carrier lifetime τ can be extracted from position and time dependent measurements of the EBIC signal respectivley. The determination of the diffusion length is explained using the configuration shown in Figure 6.1 (a) where the junction is perpendicular to the surface. In the ideal case the relation between EBIC signal and diffusion length can be explained as follows, [43]

$$I_{\mathrm{EBIC}} \propto \exp\left(-\frac{x}{L}\right). \tag{6.3}$$

This is only valid in the case of a perfect surface. As it will be shown later in this work, the surface microstructure and recombination at the surface play a significant role in evaluating the EBIC signal. The decay does not follow an ideal exponential function when there is a finite surface recombination. For the case of not negligible surface recombination Equation 6.3 has to be modified as described in [16], [43], [51].

$$I_{\mathrm{EBIC}} \propto kx^{\alpha} \exp\left(-\frac{x}{L}\right) \tag{6.4}$$

k is a constant and α is a fitting parameter. For an ideal surface without surface recombination α=-1/2 and for a infinite surface recombination rate α=-3/2.

As mentioned above, a chopped electron beam can be used to measure the minority carrier lifetime out of the decay of the EBIC signal after turning off the beam and stopping the carrier generation. This method is presented in [50] and [49] for different kinds of samples. With the SEM equipment available no beam blanking was possible and thus, this measurement method could not be done within this work.

6.2 Experimental set-up and measurement procedure

For the experimental EBIC investigations shown in this work, two different SEMs were used. A Hitachi S-4800 with a cold field emission gun and a FEI Helios focused ion beam (FIB) dual beam SEM. In the FEI tool a Schottky emitter was used. Both systems have their advantages and disadvantages. While the Hitachi SEM has a load lock big enough to load the prober shuttle, the FEI SEM needs to be vented every time the sample is changed. The FEI tool on the other hand has a very stable electron

beam which can be set to a wide range of values from 0.78 pA to 100 nA. An internal beam control ensures a stable beam current over the whole measurement time. The Hitachi SEM suffers from very unstable beam currents. Furthermore the beam current is dependent on the beam energy used. This makes the comparison of non normalized measurements complicated, as the absolute EBIC signal depends strongly on the beam current. In Table 6.1 the beam currents of the Hitachi S4800 SEM is summarized for the stable condition of the cold field emission gun. The values are shown for the case of an emission current of 10 μA and 20 μA. To achieve a good signal to noise ratio and

TABLE 6.1: Measured beam current in the stable region of the cold field emission gun of the Hitachi S4800 for an emission current of 10 μA and 20 μA.

Electron beam energy [keV]	Beam current for emission current set to 10 μA [pA]	Beam current for emission current set to 20 μA [pA]
2	35	65
5	45	82
10	73	132
20	168	275
30	291	460

still keep the possibility to measure with low beam energies most of the measurements were done using an emission current of 20 µA. If the EBIC signals are rather low, the limitation in maximum beam current is problematic. For the electrical connection of the sample, a nano-prober shuttle from Kleindiek was used (Figure 6.3a). The shuttle gives the possibility to contact the sample with 4 probes. Every probe can be moved along 3 Axes. For cross-section measurements, a specially designed prober shuttle (Figure 6.3b) with two copper plates to contact on either side of the junction, was used. To measure the beam current before and after the measurement a Faraday cup was placed on top of the shuttle. The signal was amplified using the EBIC/RCI amplifier from Kleindiek and is then, as a voltage, send back to the SEM as external detector input and a live EBIC image was shown in addition to the SEM image. The amplifier and the control unit of the prober are shown in Figure 6.3c. The EBIC signal can be observed simultaneously with the same image in the same scan speed. To reach steady state of the EBIC signal the scan speed has to be chosen accordingly (in the range of the minority carrier lifetime).

Measuring the EBIC signal either the *n*-side contact is connected to the amplifier or the *p*-side contact and the other contact is grounded. Connecting the *n*-contact results in a negative EBIC signal as the electron current is measured, while using the *p*-contact leads to a positive EBIC signal being the hole current. Both measured signals should be the same despite of the sign as electrons and holes are generated in pairs. Differences between the absolute values are due to the specimen current and is in the range of the beam current. To get the real EBIC signal it would be necessary to measure both signals to eliminate the specimen current.

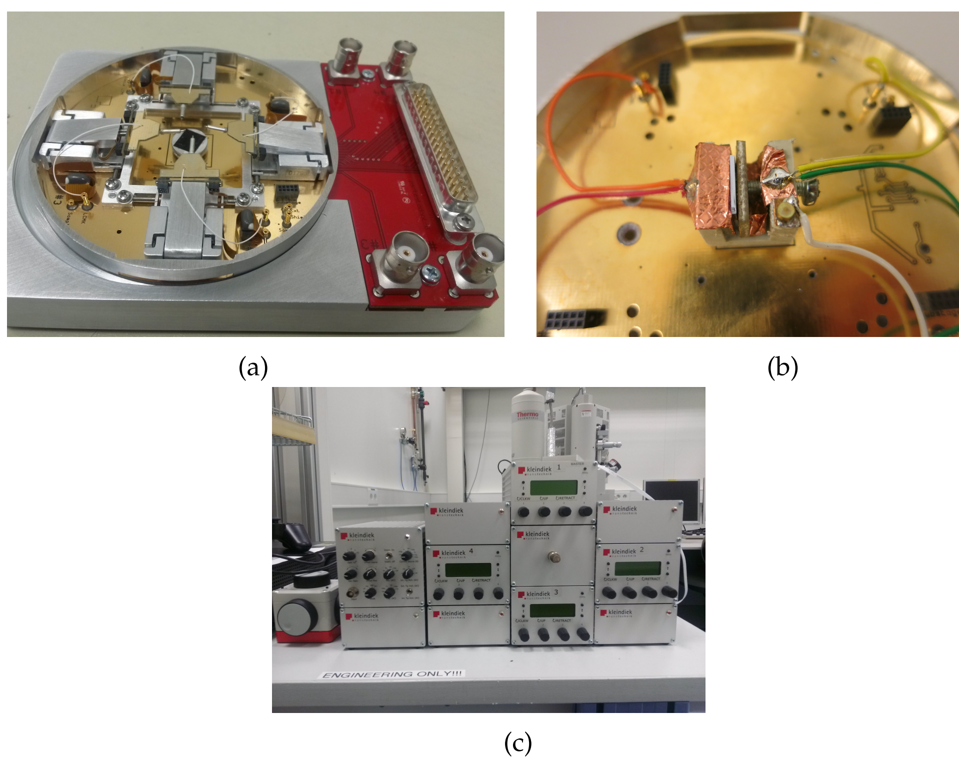

(a) (b)

(c)

FIGURE 6.3: The experimental measurement set-up. In (a) the nano prober shuttle, in (b) the cross-section prober shuttle and in (c) the controller for the nano prober shuttle and the amplifier.

Chapter 7

EBIC TCAD simulation

7.1 Introduction to TCAD

In this work, a very brief introduction to Technology Computer Aided Design (TCAD) is given. A more detailed description can be found in [52] and [53]. TCAD is a purely physics-based simulation procedure. In TCAD tools, semiconductor device behavior is simulated. This is done by using fundamental physical models like drift-diffusion and the Poisson equation. TCAD simulations can basically be divided into two main packages. The process simulation and the device simulation. The process simulator models the effects of semiconductor fabrication and follows the procedures used in fabrication of the device. This includes numerical solving of equations describing the physics of doping and dopant diffusion, oxidation, lithography, ion implantation, etching, deposition and many more. The final output of the process simulation is a data set describing the geometry and doping profile of a specific device with or without its close neighbouring devices. In the case of structures, where more simple doping profiles are sufficient, the structure generation can be done by the device simulator itself, or as in the case of the Synopsys TCAD environment, used in this work, a structure generator called Sentaurs SDE [54] is available. The structures either produced by process simulation or by alternative structure generation are then fed into the device simulator for further simulation. Device simulators give the possibility to model the electrical, optical and thermal properties of a device. The basic equations solved in a device simulator, discretisized on a grid, are the Poisson equation and the current continuity equations for electrons and holes. These equations describe the electrical behavior of a semiconductor device and were already introduced in Chapter 2. [52][53]

7.2 TCAD Simulation of EBIC measurements

7.2.1 Electron beam generation

The electron-hole pair generation distribution describes where electron-hole pairs are generated when an energetic electron beam strikes the surface of a semiconductor. It was modeled by using a lateral-dose function $F(r, z, E)$ and a depth-dose function $h(z, E)$ as discussed in [55],[56] and [57]. Here $r = \sqrt{x^2 + y^2}$ is the radial distance from the electron beam in cm, z is the depth from the surface in cm, and E is the energy of the electron beam in eV. The generation term is,

$$G(\vec{r}) = G_0 F(r, z, E) h(z, E) \tag{7.1}$$

where G_0 $[s^{-1}]$ is the surface rate of the electron-hole pair generation at the position where the beam strikes the specimen. The total generation rate G_0 depends on the electron beam energy E [eV] and the electron beam current I_{b} [A], the electron charge q [C], the electron backscattering coefficient η and the energy threshold of carrier pair generation $\epsilon_{\mathrm{i}} = 2.596E_{\mathrm{g}} + 0.7144$ [eV] where E_g [eV] is the bandgap energy. This yields for G_0 $[s^{-1}]$, [57]

$$G_0 = \frac{EI_{\mathrm{b}}(1-\eta)}{\epsilon_{\mathrm{i}}q}. \tag{7.2}$$

The electrons penetrate to about a depth called the electron range $R(E)$ [cm],

$$R(E) = \left(\frac{3.98 \times 10^{-6}}{\rho}\right) E^{1.75} \tag{7.3}$$

where ρ is the density [55]. Defining $\xi = z/R(E)$, the depth dose function for $0 \leq \xi \leq 1.1445$ is,

$$\begin{aligned} h(z,E) = \Lambda(\xi) = 0.69829 + 5.49973\xi \\ - 11.20945\xi^2 + 5.12975\xi^3. \end{aligned} \tag{7.4}$$

The coefficients have been slightly modified from the form originally used in [56] and [57] to ensure that $h = 0$ at $\xi = 1.1445$ and that the normalization condition, $\int F(r,z,E)h(z,E)d^3r = 1$ is satisfied.

The lateral dose function as stated by [56] is,

$$F(r,z,E) = \frac{1}{2\pi\sigma^2 R(E)} \exp\left[-\frac{r^2}{2\sigma^2}\right] \tag{7.5}$$

where the width σ [cm] is given by,

$$\sigma^2 = 0.36d^2 + 0.11\frac{z^3}{R(E)}. \tag{7.6}$$

Here d is the diameter of the electron beam in cm [55][56][57].

In Figure 7.1 the resulting 2D projection of the electron-hole pair generation volume is shown for a 10 keV electron beam. To check the accuracy of the analytical model, the depth dose function was compared to the result obtained through CASINO [46] simulations in Figure 7.2. It can be seen that the simulation result matches the result from Casino very well.

The above described electron-hole pair generation volume is placed at dedicated positions across the sample in the structure generation to model the effect of an electron beam at those positions. Examples are shown in Figure 7.3.

7.2.2 Parameters included in model

In the device simulator a large variety of models defining mechanisms in the device and the used materials are available and can be specified accordingly. In this chapter, only parameters which are crucial for this work are described in more detail. Using doped materials, like in this work, the standard phonon scattering model for mobility has to be

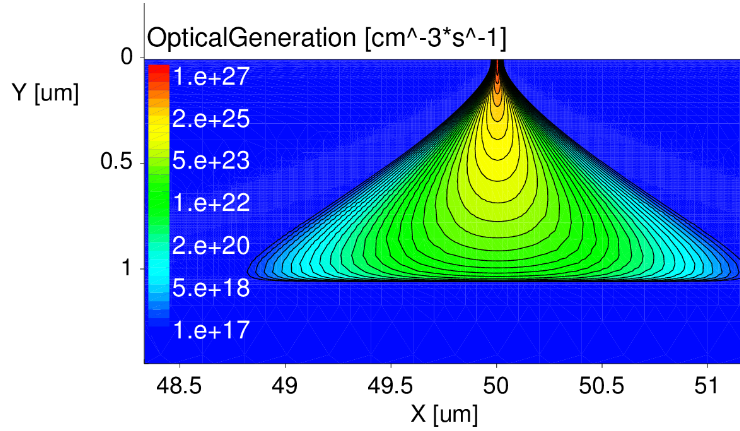

FIGURE 7.1: 2D projection of electron-hole pair generation for a 10 keV electron beam.

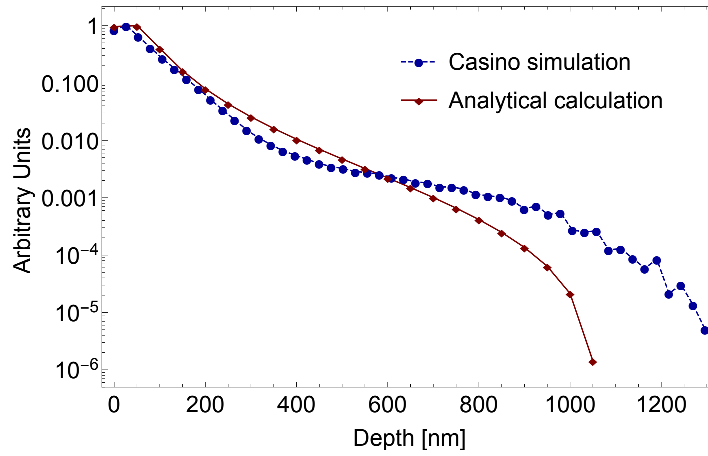

FIGURE 7.2: Depth dose function simulation, comparison between Casino and analytic calculation.

extended using a doping dependence. The default model used by the device simulator, for silicon is the Masetti model and describes the carrier scattering at impurities. Additionally, high field saturation is defined. With high fields the carrier drift is no longer proportional to the electric field and saturates to finite velocity. To also take into account mobility degradation at interfaces the Enormal (default model for silicon is Lombardi) model is activated. The details to these models can be found in [58]. The influence of doping concentration of the n- and p-type silicon was not only investigated in the mobility model, but also in the recombination model. For recombination in the bulk region a Shockley Read Hall (SRH) and Auger model was used. The SRH model describes recombination through deep defect levels in the band gap. It is implemented in Sentaurus Device like the following: [58]

$$R_{\mathrm{net}}^{\mathrm{SRH}} = \frac{np - n_{\mathrm{i}}^2}{\tau_p(n + n_1) + \tau_n(p + p_1)} \tag{7.7}$$

with

$$n_1 = n_{\mathrm{i}} \exp\left(\frac{E_{\mathrm{trap}}}{kT}\right) \quad \text{and} \quad p_1 = n_{\mathrm{i}} \exp\left(-\frac{E_{\mathrm{trap}}}{kT}\right) \tag{7.8}$$

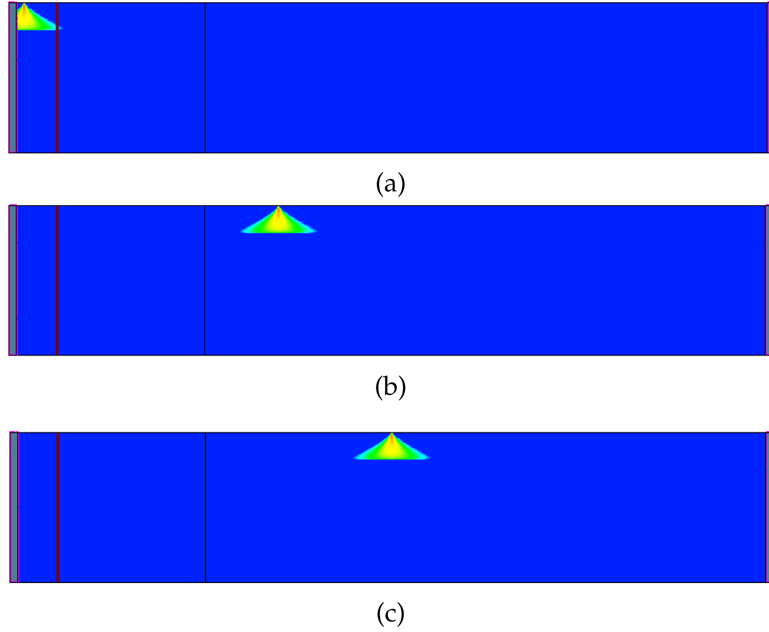

FIGURE 7.3: Examples for placement of electron hole pair generation volume across the structure. A 2 dimensional cut through the three-dimensional structure used for simulation is shown.

where E_{trap} is the energy difference between the defect and the intrinsic level. The lifetimes $\tau_{n,p}$ contain a doping-dependent, a field dependent and a temperature dependent part.

$$\tau_{n,p} = \tau_{\mathrm{dop}} \frac{f(T)}{1 + g_{n,p}(F)} \tag{7.9}$$

The doping dependence and the temperatrue dependence are shown in Equation 7.10 and Equation 7.11 respectively.

$$\tau_{\mathrm{dop}} \left(N_{A,0} + N_{D,0}\right) = \tau_{\mathrm{min}} + \frac{\tau_{\mathrm{max}} - \tau_{\mathrm{min}}}{1 + \left(\frac{N_{A,0}+N_{D,0}}{N_{\mathrm{ref}}}\right)^{\gamma}} \tag{7.10}$$

$$\tau(T) = \tau_0 \left(\frac{T}{300K}\right)^{\alpha} \tag{7.11}$$

In the simulation, the surface recombination was described by a surface Shockley-Read-Hall recombination model depending on the hole and electron densities p and n and the surface recombination rates s_n and s_p for electrons and holes. The relation for the case of silicon is shown in Equation 7.12 [58]

$$R_{\mathrm{surf,net}}^{\mathrm{SRH}} = \frac{n_{\mathrm{s}} p_{\mathrm{s}} - n_{\mathrm{i}}^2}{(n_{\mathrm{s}} + n_{\mathrm{i}})/s_p + (p_{\mathrm{s}} + n_{\mathrm{i}})/s_n}. \tag{7.12}$$

With n_{i} being the intrinsic carrier concentration, n_{s} and p_{s} the electron and hole concentration at the surface. The parameter that was varied in the simulation is the surface

recombination rate. Its doping dependency is modeled as shown in Equation 7.13 [58]

$$s = s_0 \left[1 + s_{\mathrm{ref}} \left(\frac{N_{\mathrm{i}}}{N_{\mathrm{ref}}} \right)^{\gamma} \right]. \tag{7.13}$$

In the simulations, s_{ref} was set to 10^{-3}, N_{ref} to 10^{16} cm^{-3} and γ to 1. N_{i} is the doping concentration [58], [59]. Models like the SRH recombination model depend on traps but do not actually model them. In device physics they are important as they increase recombination and leakage. Sentaurus Device offers different ways of implementing traps specified either as electron and hole traps or fixed charges with different energetic distribution models. In this work we focused on fixed charges, which are uniformly distributed placed at the interface between silicon and silicon-dioxide. Fixed charge traps are always occupied and can either be negative or positive. The trap concentration N_0 for uniform energetic distribution is defined as:

$$E_0 - 0.5E_S < E < E_0 + 0.5E_S \tag{7.14}$$

In the case of interface fixed charges N_0 is given in $\mathrm{eV}^{-1}\mathrm{cm}^{-2}$. The Sentaurus Device package offers a lot more possibilites to include traps and charges to the simulation than shown here. More information can be found in [58]. On the measurement parameter side, the electron beam energy is changed within the structure generation, influencing the electron-hole pair generation volume. Furthermore, reverse biasing of the investigated diodes was examined.

7.2.3 Structure Generation

The structures investigated in this work were simulated using the two procedures described above. For the first part of the experimental work, where simpler structures were used, the structure generation was done by Synopsys SDE [54]. Simple, almost step junction like, doping profiles were investigated in this case. For the more complex structures, investigated in the second part of this work, process simulations were used to generate the doping profiles. In both cases it was necessary to generate three-dimensional structures as the symmetry of the investigated problem (cylindrical symmetry for the beam and perpendicular mirror symmetry for the sample) demanded this. One disadvantage of using three-dimensional structures is the extensive simulation time needed. According to this, the structure sizes were chosen in a way to find a good trade-off between simulation time, minimum necessary size and information gain. Additionally to the definition of geometry, materials and doping of the structure also the meshing for the further simulation was defined within the structure generation. Here again a trade-off between mesh size and computation time had to be found. In areas of special interest or were parameters like doping dependence change a lot, a finer mesh had to be chosen. The simulated structures will be shown in the experimental part of this work where also the simulation results are discussed and are compared with the measurements. Additional to the structure and its definitions also the electron beam generation is done using the structure editor. As there is no model, handling the carrier generation for an electron beam included to the simulator, the generation was defined as optical generation with a special generation volume defined.

7.2.4 Transient simulation and EBIC line scan

The output of the device generation, a mesh file defining the structure, is then used within Synopsys Sentaurs Device [58], the Device simulator used within this work. There the electrode definitions are set and the output parameters are defined. In the physics section the used models are specified and the ramping specification of the "optical" generation is done. In the Math section the parameters for the transient simulation are set. The last section is the Solve section. In this work, the transient simulation was performed in this part. At the beginning the Poisson equation was solved for electrons and holes. Followed by the transient part, where the time steps are specified. In this specific case the turning on and off of the electron beam and the biasing of the sample was done. Minimum and maximum step sizes were defined together with initial and final time. Furthermore, special turning points can be implemented for critical positions. At the end, again the Poisson equation was solved for electrons and holes. The carriers collected from the contacts are integrated to calculate the total current. A series of transient simulation current outputs for different x-positions of the electron beam generation volume is shown in Figure 7.4. On the x-axis the time is

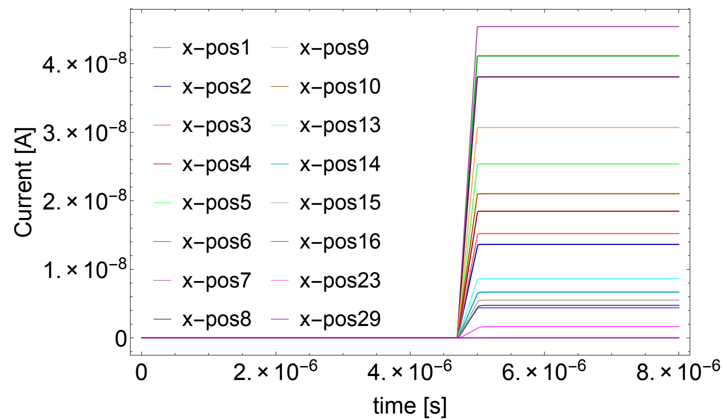

FIGURE 7.4: Output of transient simulation for several x-positions of the electron-hole generation volume. Showing the measured current at one contact in dependence on the time.

shown while at the y-axis the current collected at one contact is plotted. The electron beam was turned on at 0.5×10^{-5} s and the current saturates to a constant value after some time. This saturation time depends on the minority carrier lifetime in the region where the carriers are generated. The longer the lifetime and the bigger the region from where carriers can diffuse, the longer the time until saturation is reached. The current value of the last point in the saturation regime is then extracted for each position of the electron-hole generation volume and a simulated EBIC line scan is created. Additionally, to the total current collected by the contacts a variety of other output parameters can be specified such as the doping concentration, electric field, carrier density and the SRH recombination to name just a few.

Chapter 8

EPI diodes

With the goal of setting-up the EBIC measurement system and the TCAD environment, rather simple diode structures were designed. The main idea was to get an understanding of the measurement method and the influence of different parameters concerning the sample and the measurement. Additionally, it was convenient to calibrate the simulated and experimental EBIC set up with a well understood design that can be verified with analytic expressions. In the following, sample parameters like doping concentration of the *n*-type and the *p*-type silicon, surface preparation methods and measurement parameters like electron beam energy and diode biasing were investigated. Parts of this chapter were already published in [60] and [61].

8.1 Structure

The diodes were built up in form of a stack configuration with the junction parallel to the sample surface. On top of a *p*++ doped substrate with a doping concentration of 10^{19} cm^{-3} first a 20 µm thick *p*-doped layer (*p*-EPI) was grown epitaxially followed by a 5 µm epitaxially grown *n*-doped layer (*n*-EPI). Finally a 100 nm *n*+-doped contact layer with a doping concentration of 10^{19} cm^{-3} was deposited. During deposition care was taken to minimize the thermal budget to get abrupt junctions. The *n*+-contact layer was heavily doped to form tunnel contacts with low ohmic resistance in the case of the *p*+-contact the already heavily doped *p*++ substrate was used. Wafers with varying *n*- and *p*-doping concentrations were produced. In Figure 8.1, the schematic built up of the structure and the measurement set up is shown. The wafer surface, next to the *n*+-region, is defined as x-position x=0.

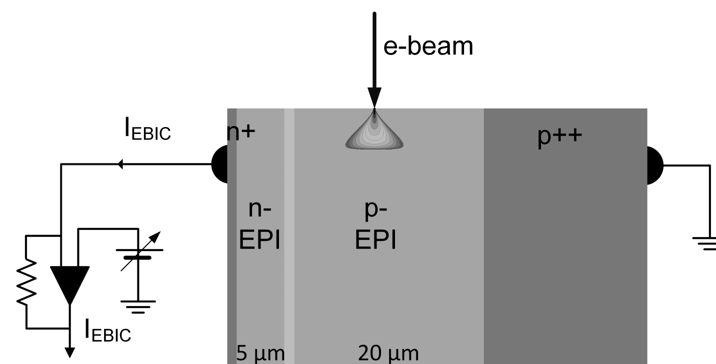

FIGURE 8.1: Schematic structure of EPI diode in cross-section view and measurement mode shown.

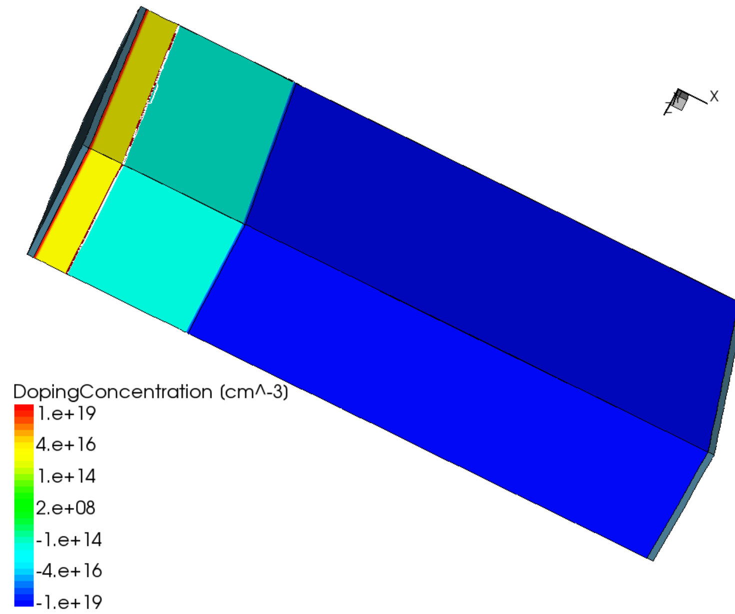

FIGURE 8.2: 3D Structure generated by simulation. The color coding is showing the doping concentration in cm^{-3} [61]

The n-EPI doping concentrations processed were 5×10^{14} cm^{-3}, 10^{15} cm^{-3}, 10^{16} cm^{-3} and 5×10^{16} cm^{-3}. The p-EPI layers investigated had either a doping concentration of 7×10^{14} cm^{-3} or an almost intrinsic doping (10^{13} cm^{-3}). Both p-type variations are standard for CMOS EPI wafers. The structure was also rebuilt for simulation using Sentaurus SDE [54]. In Figure 8.2 the generated 3D structure, including the doping profile, is presented.

In Figure 8.3a the simulated acceptor and donor concentrations across the structure are shown and compared to boron and phosphorus concentrations from Secondary Ion Mass Spectrometry (SIMS) measurements performed on an experimental investigated structure. In the case shown the n-EPI doping concentration is 10^{16} cm^{-3} and the p-doping is 7×10^{14} cm^{-3}. Additionally, the electric field distribution extracted from simulation is shown in Figure 8.3b. There are electric fields at the $n+/n$ interface, the n/p interface, and the $p/p{+}{+}$ interface. The field strengths are dependent on the the doping concentrations on n- and p-side. All electric fields point towards the $p{+}{+}$ region. The electric fields at the $n+/n$ interface and the $p{+}{+}/p$ interface reflect the minority carriers and prevent them from diffusing in the heavily doped contacts.

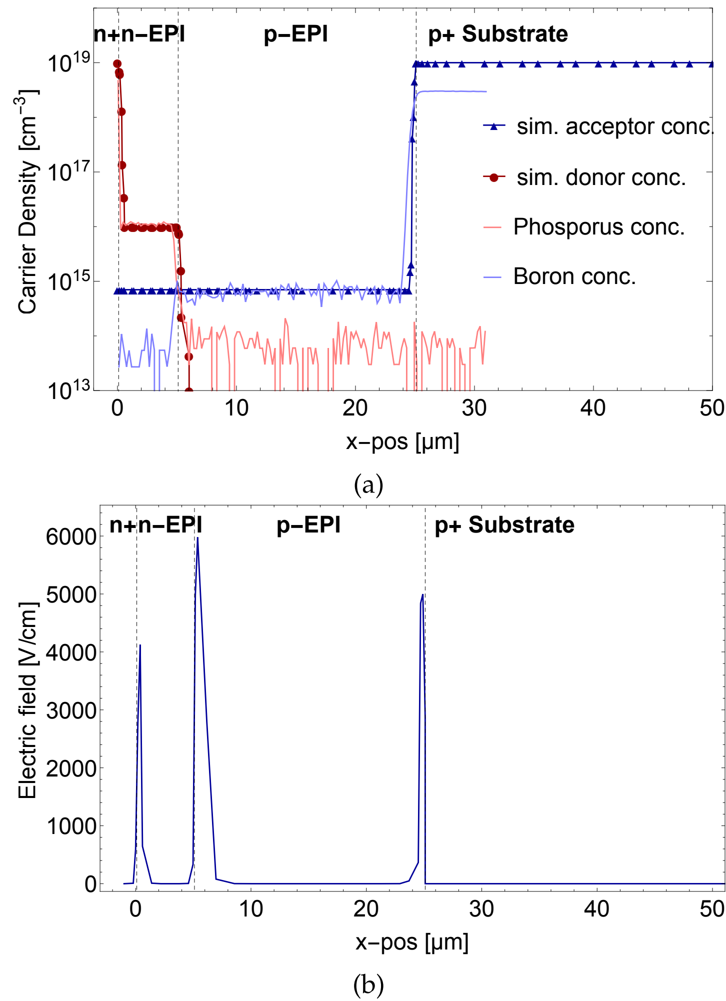

FIGURE 8.3: The simulated carrier density (a) and electric field (b) are shown. The *n*-EPI doping concentration is 10^{16} cm^{-3} and the *p*-doping is 7×10^{14} cm^{-3}.

8.2 Sample preparation

The measurements were done in cross-section mode as shown in Chapter 6 in Figure 6.1 (a) and Figure 8.1. In this case the *p*-*n* junction is perpendicular to the scanned surface. To get this measurement configuration the wafer was cleaved into pieces of about one times one cm^2 and the resulting cross-sections were investigated. Three different sample treatments and their influence on the EBIC signal were compared to each other. One time the sample was simply cleaved and no further treatment was done. In this case a thin layer of native oxide is on the surface that is formed right after the cleaving process. A second set of samples is ground and polished after cleaving. The grinding and polishing is done using a Sagitta Centar polishing system with decreasing granulation. The last polishing step was done using a 0.1 µm diamond lapping film. The last set of samples is etched with hydrofluoric acid (HF) after the cleaving. The idea of the HF etching is to remove the native oxide on top of the cleaved surface. Additionally, the surface is passivated after the HF treatment as shown by [62] and [63]. Yablonovitch et al [63] found that an HF etched silicon surface is very inacitve from an electronic point of view. They measured a surface recombination rate of 0.25 cm/s on a Si[111] surface after HF etching. The passivation is achieved by Si-H bonds, leaving no dangling bonds at the surface which could act as recombination centers.

This was shown again by Trucks et al [62] using ab initio molecular-orbital theory. The measurements were done from some minutes after etching up to 3 weeks after etching. After storage times in air longer than 3 weeks the passivation effect of the HF etch seemed to be expired.

8.3 Mesurement and simulation results

In the measurement, the electron beam is scanned across the sample and the EBIC signal is measured. The contact is made by pressing two copper plates on either side of the cleaved sample. Because of the high doping of the surface and the starting material almost perfect ohmic contacts can be made. From the position dependent EBIC signal a two dimensional EBIC image is recorded. In Figure 8.4 a SEM image and the corresponding EBIC image are shown. Using an implemented calibration procedure, a map of the EBIC signal in ampere is produced out of the gray scale image recorded with the SEM system. For better illustration and comparison between the

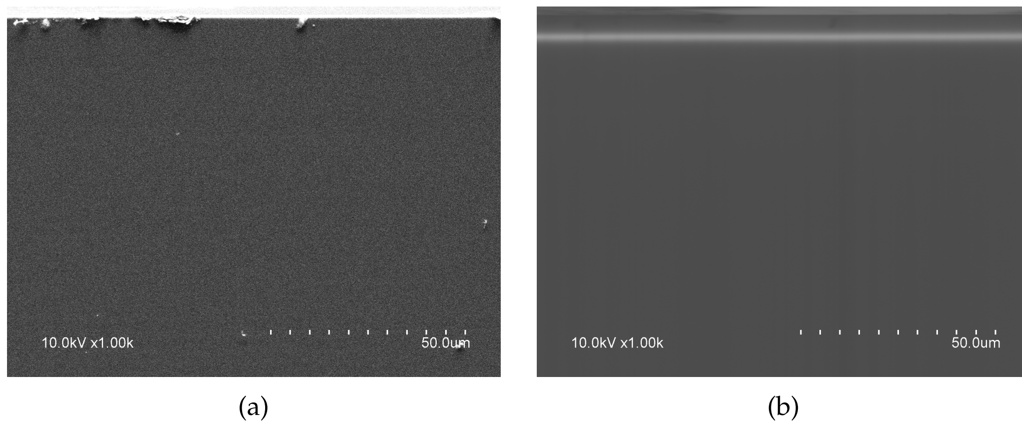

(a) (b)

FIGURE 8.4: In (a) the SEM image of the cross-section sample is shown and in (b) the corresponding EBIC signal.

different measurements and simulation out of these 2D images, 1D line-scans are extracted (Figure 8.5) for the following discussions.

Line scans were also simulated. The beam was placed on several x-positions across the structure and the transient simulation as explained in Chapter 7 was performed for each position. In Figure 8.6 the line-scans extracted from simulation and measurement are compared with each other. In both cases the electron beam energy was 20 keV and the electron beam current 200 pA. The absolute values of simulation and measurement are in very good agreement, demonstrating the suitability of the analytic model used for the beam generation discussed in Subsection 7.2.1. The shape of the 1D signals and how the simulation is fit to the measurement will be discussed later in this chapter.

8.3.1 Influence of surface recombination rate

To experimentally investigate the influence of surface quality, the aforementioned sets of samples with different surface preparations were compared with each other.

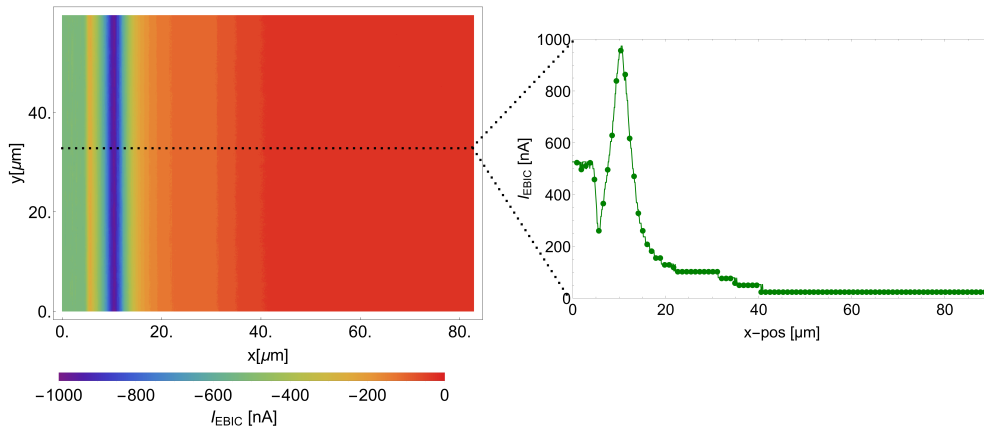

FIGURE 8.5: Data extraction from measurement. A 1D line scan is extracted out of the calibrated 2D EBIC signal

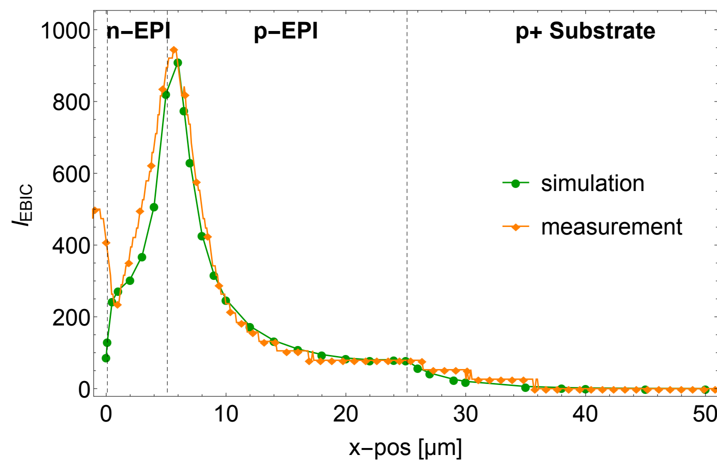

FIGURE 8.6: Comparison of EBIC line-scan done by simulation and measurement. The electron beam energy is 20 keV and the electron beam current 200 pA.

Measurements performed on purely cleaved samples that were not treated with HF or ground were unstable. The longer one is scanning over an area, the bigger gets the area with significant EBIC signal and is spreading even into the region of the highly doped substrate where high recombination is expected. Apparently, the electron beam changes the surface recombination during the measurement. One explanation could be the introduction to charges into the oxide and the silicon/silicon-dioxide interface by the electron beam. A positive charge on the p-side would lead to an inversion of the surface due to accumulation of electrons at the silicon surface resulting into a surface depletion region.This point is discussed in more detail later in this chapter. Several tests were performed concerning the influence of time between etching and measurement. Measurements were done right after etching as well as after some time of storage. After longer times of storage (about three weeks) before being measured, the HF etched samples also become unstable and behave like the simply cleaved ones.

In Figure 8.7 line scans of a ground and an HF etched sample are plotted. The electron beam energy used in the measurement was 20 keV and the beam current about 200 pA. The n-EPI concentration was 10^{16} cm^{-3} and the p-EPI concentration was 7×10^{14} cm^{-3} in both cases. Because of the long term instability of the beam current (i.e. over the time interval of a few hours), the EBIC signal was normalized to its maximum value. For the ground sample, a sharp peak of the EBIC signal was observed at the position

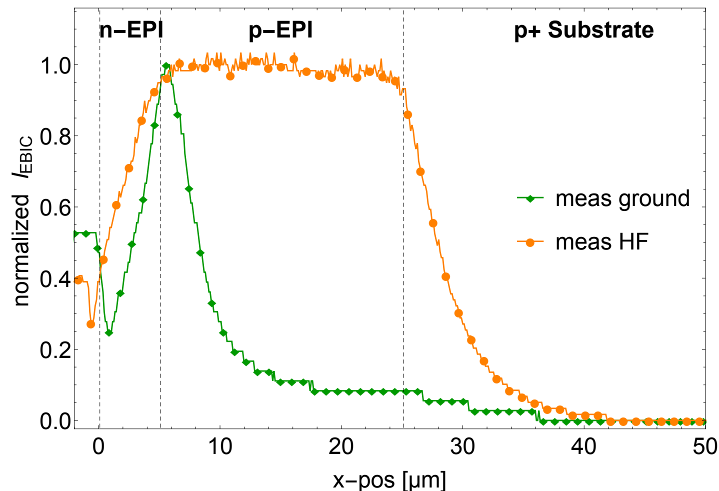

FIGURE 8.7: EBIC line scan of a HF etched and a ground sample. The n-EPI concentration was 10^{16} cm^{-3} and the p-EPI concentration was 7×10^{14} cm^{-3}. The electron beam energy was 20 keV.

of the p-n junction. The n-EPI is located on the left side of the peak and the p-EPI followed by the p++ substrate is located on the right side. The different regions of the sample are indicated and separated with dashed lines in the plot. The signal decays fast with distance from the position of the junction in the regions of the n- and p-EPI layers. A plateau at the position of the p-p++ junction can be observed. Inside the p++ substrate the EBIC current drops to zero exponentially. The HF etched sample shows a more or less constant value over the whole region of the p-EPI layer followed by a decay in the contact regions because of the high bulk recombination rate due to high doping. The different behavior between the two samples can be explained by the difference in surface quality resulting from the different surface preparation methods. To get a better idea of the surface quality, a Transmission Electron Microscopy (TEM) analysis was made for a ground, a HF etched and a simply cleaved sample. The TEM lamella preparation, images and the further analysis was done at Felmi-Zfe the austrian center of microscopy and nanoanalysis. The comparison of the three TEM images of the cross-section lamellas are shown in Figure 8.8. The lamellas were prepared with a Focused Ion Beam (FIB). In the case of the ground sample, a combination of a AuPd layer and Pt layer was used as a protection layer. In the case of the HF etched sample, only a Pt layer was used for protection [64]. The used electron beam energy was 200 keV. The specimens were oriented so that the [1 0 0] (a) and the [1 0 1] (b) orientation of the silicon substrate could be imaged.

Comparing the TEM images one can see the large surface roughness of the ground sample (Figure 8.8c). The disturbance of the lattice reaches deeper than 200 nm. On top of the crystalline silicon a layer of amorphous silicon is formed. On top of that an about 5 nm thick native oxide has formed. This information is provided by energy filtered TEM (EFTEM) images and EDS spectra. The cleaved (Figure 8.8a) and HF etched (Figure 8.8b) sample have a very smooth surface and the single crystal structure is preserved throughout the whole sample up to the interface between surface and the native oxide. The only difference between these two samples is in the thickness of the native oxide that is very thin in the case of the HF etched sample. It was assumed that there is no native oxide on the HF etched sample, when measuring right after etching. It is very likely that the oxide seen in the TEM images developed because of the depositions done for the lamella preparation. The knowledge gained from the TEM

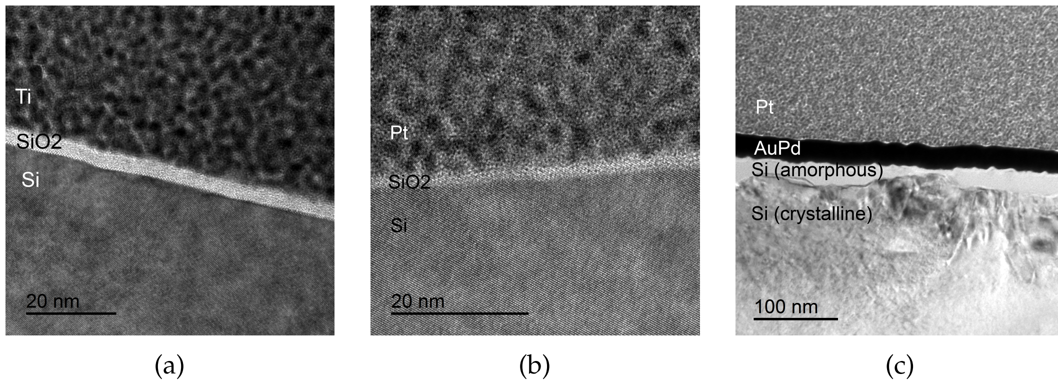

(a) (b) (c)

FIGURE 8.8: Investigation of surface quality using TEM analysis. TEM image of a lamella prepared from (a) a simply cleaved sample, (b) an HF etched sample and (c) a ground sample. In the case of the ground sample an AuPd and Pt layer was used as protection layer. In the case of the cleaved and the HF etched sample only a Pt layer is used. The used electron beam energy was 200 keV. The specimens were oriented so that the [1 0 1] (b) and the [1 0 0] (c) orientation of the silicon substrate could be imaged. [61] The TEM images were done at FELMI-ZFE the austrian center of electron microscopy and nanoanalysis.

analysis confirms the assumption that grinding is damaging the surface and the EBIC measurements hinting to an increased surface recombination, are supported by these results. Another interesting effect was observed when performing EBIC measurements using different beam currents. While the EBIC signal stays constant with a beam current of 0.8 nA or less, even for long exposure times, a drastic decrease in EBIC signal, for consecutive measurements in the same area, is observed when a beam current of 1.6 nA is used. The evolution of the EBIC signal with time is shown in Figure 8.9a. In Figure 8.9b the 2D EBIC signal is shown. The image was recorded, after doing several measurements zoomed in to the region in the center of the image, resulting in a region with degraded EBIC signal. This effect can have several reasons. One possibility is carbon contamination or amorphisation of the surface what increases the surface recombination rate [44], [45].

The quality of the surface is related to the density of recombination centers at the silicon surface or the silicon/silicon-dioxide interface. The recombination there is described by a surface recombination rate which is defined for holes s_p and electrons s_n respectively,

$$s_p = \sigma_{ps} v_{\text{th}} N_{\text{it}} \text{ and } s_n = \sigma_{ns} v_{\text{th}} N_{\text{it}}. \tag{8.1}$$

Here σ_{ps} and σ_{ns} are the capture cross sections in cm^2 for holes and electrons at the surface respectively, v_{th} [cm/s] is the thermal velocity and N_{it} is the interface trap density in cm^{-2}. If the concentration of recombination centers at the surface is very high, the recombination in this region can be higher than in bulk regions and can even be the dominant recombination process for devices with a low quality surface. [26], [59], [65], [66] The influence of the silicon surface and its recombination properties was also investigated by simulations. The advantage of the simulation is that dedicated surface properties can be set and compared. The surface recombination model used in the simulations was introduced in Subsection 7.2.2 and is defined by Equation 7.12 and Equation 7.13. Simulations were done for six different surface recombination rates ranging from a perfect surface with no surface recombination rate (s_0=0 cm/s) to a very high surface recombination rate ($s_0 = 10^7$ cm/s). The results are shown in Figure 8.11a. In the case of silicon $s_0 = 10^3$ cm/s is the default value used in TCAD simulations

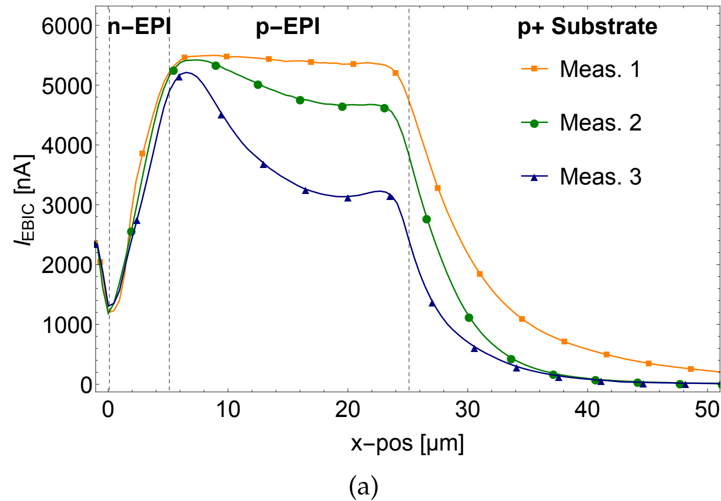

(a)

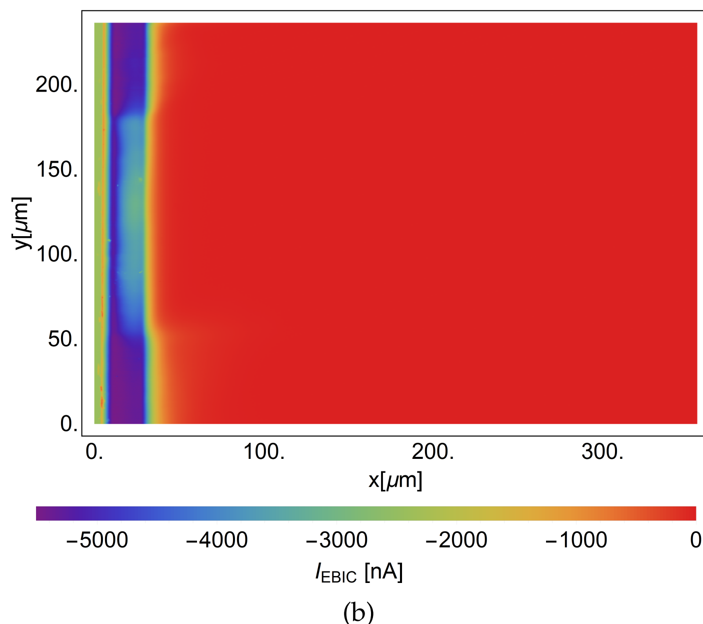

(b)

FIGURE 8.9: Influence of beam current on EBIC signal. (a) Three subsequentially measured EBIC line-scans [61] and (b) a 2D EBIC image after a zoomed in measurement in the center of the image showing the degradation of the EBIC signal of an HF etched sample using 1.6 nA electron beam current. The electron beam energy was 20 keV.

[58]. The simulations were done using the same structure as the experimental one for comparison, but also for a slightly changed structure shown in Figure 8.10.

In this structure the n-EPI region was expanded to 50 µm to show the decay of the EBIC signal in this region more clearly. The EBIC signal decays steeply as the electron beam moves away from the p-n junction for higher surface recombination rates. In Figure 8.11b the measured EBIC results are compared to simulated ones. For the comparison between measurement and simulation the structure generated for the simulation is the same as experimentally investigated. The simulation using a recombination rate of $s_0 = 10^6$ cm/s matches very well the measurement of the ground sample and the simulation using the recombination rate of $s_0 = 10^3$ cm/s fits well to the HF etched sample in the p-doped regions but not in the n-doped region. The bulk lifetime set in these simulations is 3×10^{-4} s for holes and electrons. These values are chosen due to

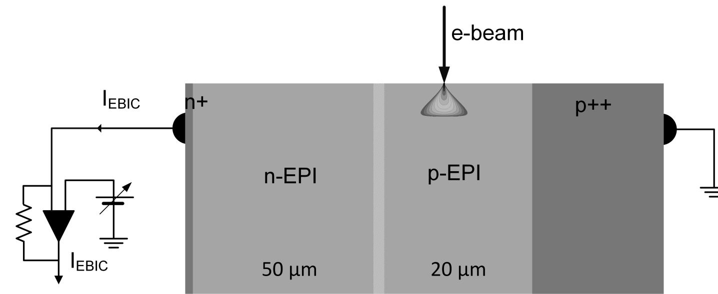

FIGURE 8.10: Schematic structure of EPI diode in cross-section view and measurement mode used for simulations.

experience of EPI devices gained through former simulation. In reality the minority carrier lifetime is different for holes and electrons. To keep the model as simple as possible this difference is left aside in the investigations.

Fitting the decay of the signal after the junction to an exponential function results in an effective diffusion length which is a combination of surface and bulk effects. The experiments show that grinding increases the surface recombination drastically. If the bulk diffusion length is to be determined experimentally from an EBIC measurement, HF etching is a far superior surface preparation than grinding and polishing. On the other hand, if EBIC is used to determine the location of a *p*-*n* junction, a ground surface will show the location more clearly. Applications to more enhanced structures are shown later in the next section.

8.3.2 Influence of doping concentration

With increasing doping concentration the minority carrier lifetime decreases [67]. This is reflected in a decreased diffusion length and should be visible in the EBIC signal in field free regions. Furthermore, the space charge region width decreases. In the experiment *n*-doping concentrations ranging from 5×10^{14} cm^{-3} to 5×10^{16} cm^{-3} are investigated. In the simulation *n*-doping concentrations from 10^{15} cm^{-3} to 10^{18} cm^{-3} are compared. The simulations are done for surface recombination rate values of 10^{7} cm/s, 10^{5} cm/s and 10^{3} cm/s and are shown in Figure 8.12 respectively. The *p*-doping concentration was 7×10^{14} cm^{-3} in both cases. A large influence of the surface recombination on the *n*-doping concentration dependence can be seen. The higher the surface recombination rate, the smaller is the effect of the doping concentration. In the measurements, no significant difference was observed when the doping concentration was varied on the *n*-side. This can have two explanations. The very poor surface quality of the ground samples as proven before or because of an influence of the contact region that is in the case of the experimental samples very close to the junction. In the case of low surface quality the surface recombination is the dominant recombination process in the device as shown in the section before. This reduces the effect of the doping concentration on recombination and thus diffusion length because it is a bulk effect.

Also the influence of *p*-EPI doping concentration was investigated. As already mentioned before two standard doping concentrations used in EPI wafers for CMOS devices are compared. The *n*-doping concentration is 10^{16} cm^{-3} and the low *p*-EPI doping concentrations are 10^{13} cm^{-3} and 7×10^{14} cm^{-3}. The measured EBIC line scans of a ground sample are shown in Figure 8.13a and the simulated line scan with a surface recombination rate $s_0 = 10^{6}$ in Figure 8.13b.

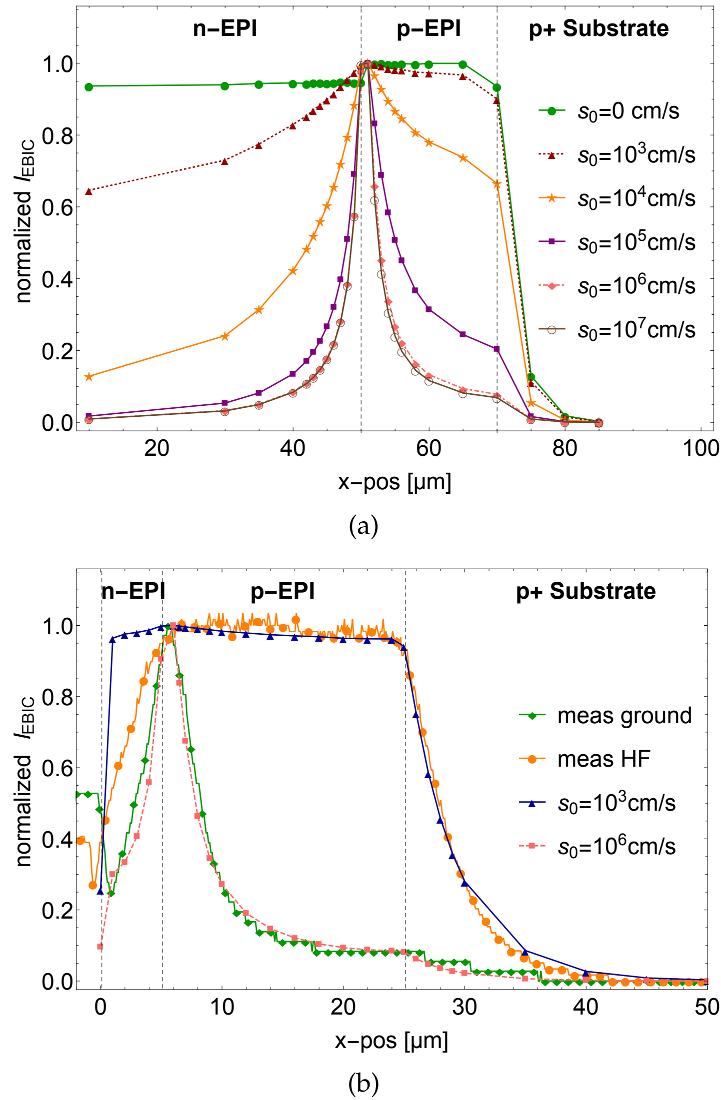

FIGURE 8.11: The influence of surface quality on the EBIC signal is shown. In (a) the simulated EBIC signal for surface recombination rates from 0 cm/s to 10^7 cm/s are plotted. In (a) the measurements of and simulation for two surface conditions are shown. The *n*-EPI doping concentration was 10^{16} cm^{-3} and the *p*-EPI doping concentration was 7×10^{14} cm^{-3}. [61]

A strong difference was observed upon changing the *p*-type doping in the simulation as well as in the measurement, even though they do not fit perfectly. A broadening of the peak at the position of the *p*-*n*-junction can be seen for the lower doped *p*-EPI (Figure 8.13). This is due to an increased space charge region because of lower doping on the *p*-side. Furthermore, the minority carrier diffusion length is higher in the lightly doped *p*-EPI than in the more heavily doped one. This is visible in the decreased slope of the EBIC signal on the *p*-side. Especially in the measurement, also the influence of the *p*-*p*++ junction seems to be stronger in the 10^{13} cm^{-3} in comparison to the higher *p*-EPI doping of 7×10^{13} cm^{-3} (Figure 8.13a). Contrary to the measurements, the peak at the *p*-*p*++ junction is less prominent in the simulation and the shape of it is more similar to the plateau seen in the structures with higher *p*-doping.

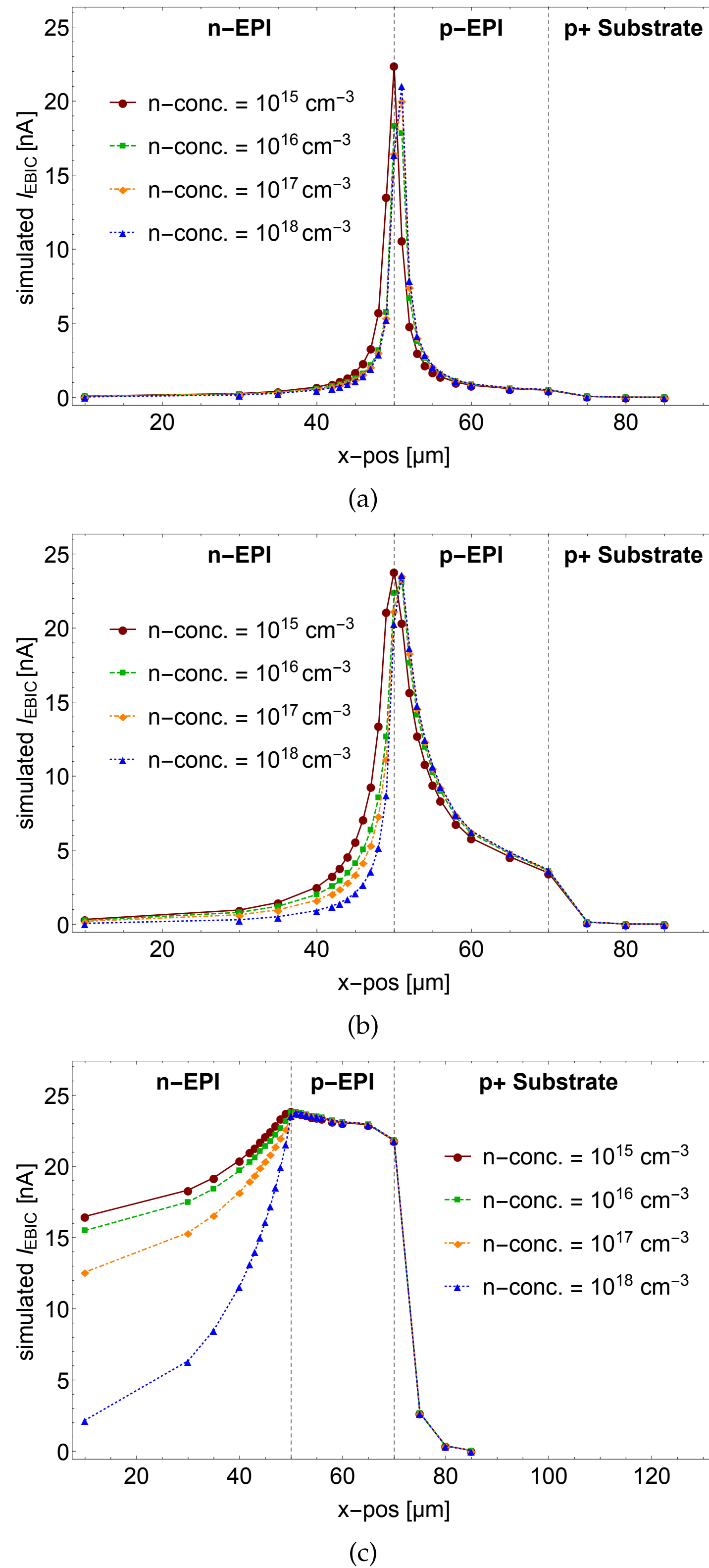

FIGURE 8.12: The influence of n-doping concentration is simulated in (a) for a surface recombination rate of 10^7 cm/s, 10^5 cm/s in (b) and in (c) for 10^3 cm/s. The p-doping is 7×10^{14} cm^{-3}. The electron beam energy used is 20 keV.

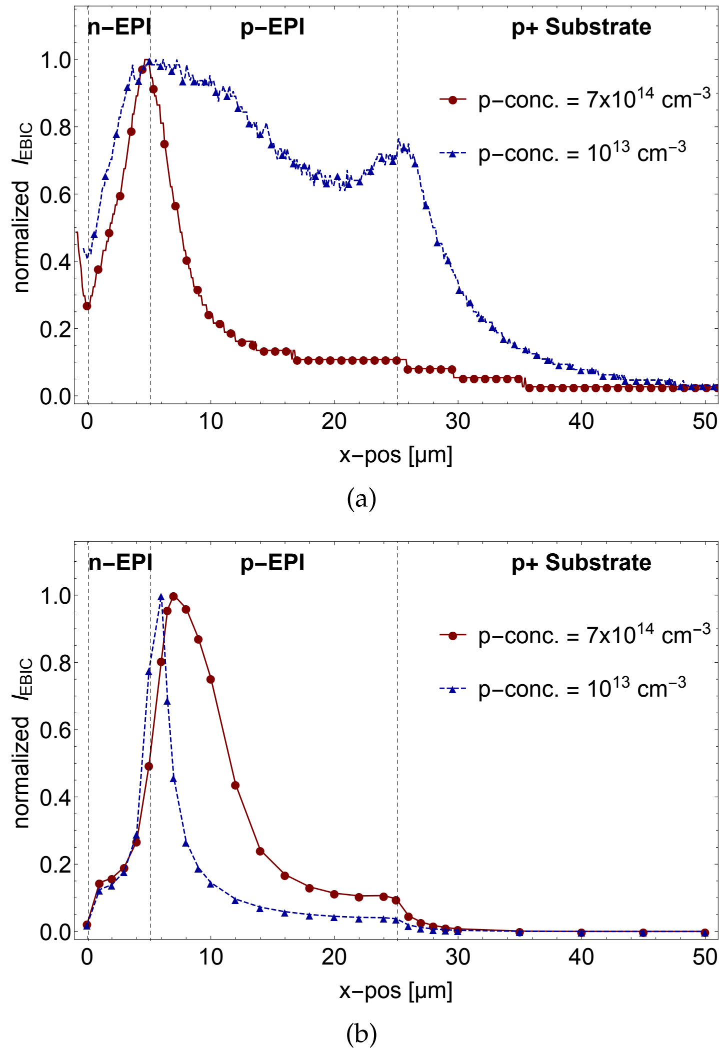

FIGURE 8.13: The influence of p-doping concentration. Comparison between 7×10^{14} cm^{-3} and 10^{13} cm^{-3}. (a) Measurement of ground sample (b) simulation with a surface recombination velocity of 10^6 cm/s. The n-doping is 10^{16} cm^{-3}. The electron beam energy used is 20 keV.

8.3.3 Influence of electron beam energy

By increasing the electron beam energy, the interaction volume of the electrons gets bigger in lateral and vertical direction as shown in Chapter 4. More charge carriers are generated because of the higher energy of the primary electrons resulting in a higher EBIC signal. A higher electron beam energy is an advantage in measurements with low signal outputs. The drawback of a high electron beam energy is the reduced resolution. Depending on the SEM used, also the electron beam current increases with increasing electron beam energy which also leads to an increased EBIC signal. To eliminate this factor, the measurement results are normalized to their maximum value. In Figure 8.14a and Figure 8.14b the measured influence of electron beam energy is shown for a ground and an HF etched sample respectively. The measurements were done with electron beam energies of 10 keV, 15 keV, 20 keV, and 30 keV. In the case of the ground sample a strong energy dependence was observed. The influence of the electron beam energy on the EBIC signal of the HF etched sample is much smaller.

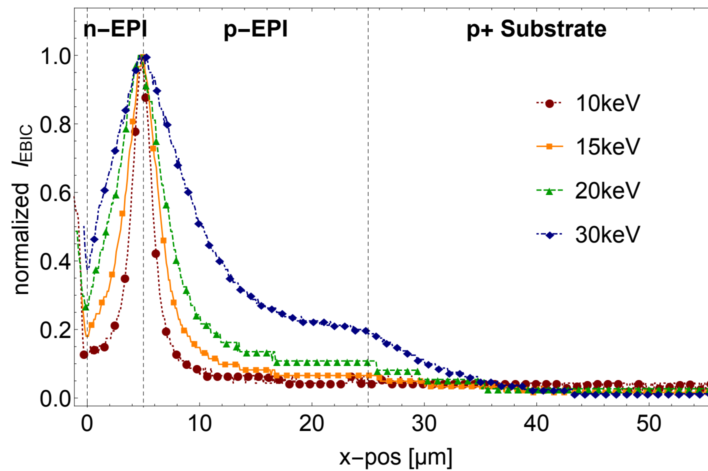

(a)

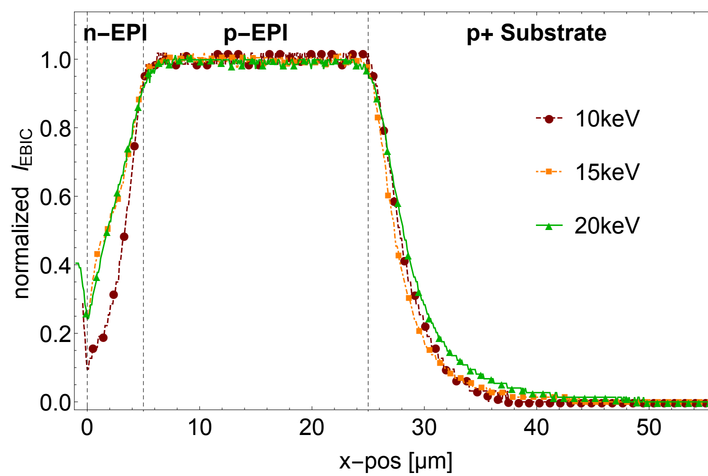

(b)

FIGURE 8.14: The influence of the electron beam energy was investigated. (a) The EBIC signal of a ground sample and (b) an HF etched sample is shown. The EBIC signal was normalized to its maximum value. The n-doping concentration was 10^{16} cm^{-3} and the p-doping 7×10^{14} cm^{-3} in both cases. [61]

The influence of electron beam energy is also reproduced by simulation. In Figure 8.15b the simulation for a surface recombination rate of 10^6 cm/s and in Figure 8.15a for 10^3 cms/s are shown for electron beam energies of 2 keV, 5 keV, 10 keV, 15 keV and 20 keV. The simulated signal matches the behavior already observed by measurement very well.

The effect seen in measurement and simulation was explained in [68] and [14]. The lower the electron beam energy is, the smaller the interaction volume is and more of the carrier generation is closer to the surface where they recombine quickly in the case of low surface quality. With higher beam energies, the maximum generation rate is deeper in the material and is not so strongly affected by surface properties. From the measurement and the simulation one can see that in the case of lower electron beam energies the decay of the EBIC signal after the junction is steeper and thus the effective diffusion length extracted is smaller [14], [68]. When the surface quality is high, having a low surface recombination rate, the depth of generation does not play a big role and no influence of electron beam energy can be seen. In this case the

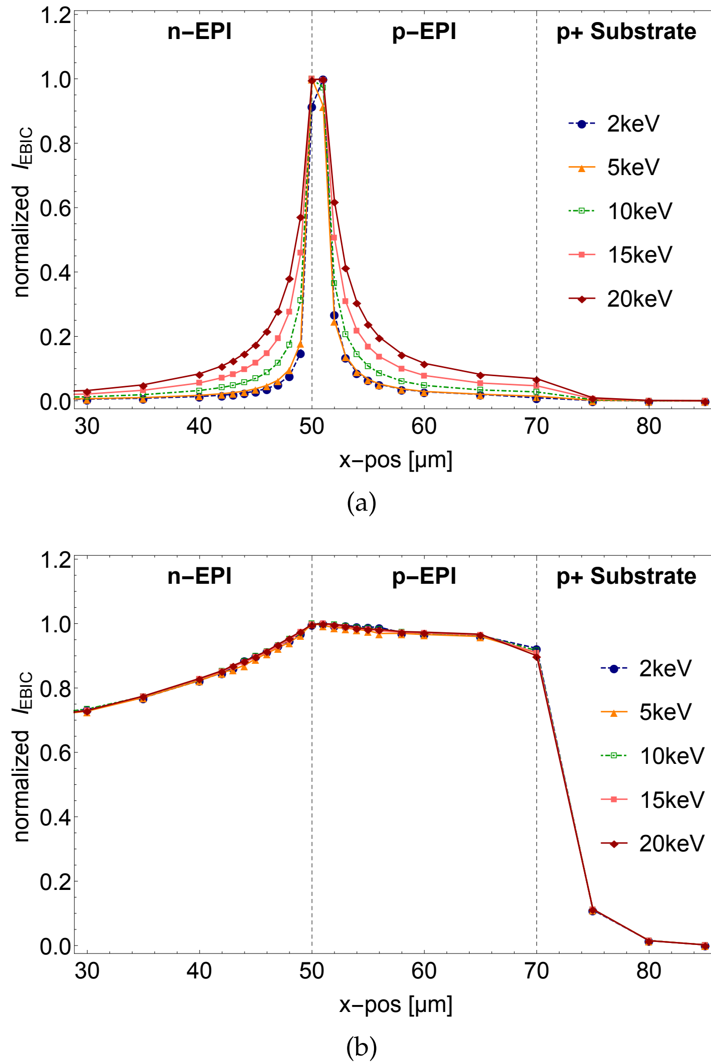

FIGURE 8.15: The influence of the electron beam energy was investigated by simulation. (a) The surface recombination rate is $s_0 = 10^3$ cm/s and in (b) $s_0 = 10^6$ cm/s. The EBIC signal is normalized to its maximum value. The n-doping concentration is 10^{16} cm^{-3} and the p-doping 7×10^{14} cm^{-3} in both cases. [61]

extracted diffusion length is the bulk diffusion length. Varying the beam energy in EBIC measurements gives a very good indication about surface quality. If there is no beam energy dependence, the surface is perfect. An observation of a beam energy dependence is an indication for a high surface recombination rate.

8.3.4 Biasing of the diode

Since the EBIC signal depends on the internal electric fields, it can be used to monitor changes in the device if a bias voltage is applied. Measurements and simulations applying different bias voltages are performed and are shown for a sample with a n-doping concentration of 10^{16} cm^{-3} and a p-doping concentration of 10^{13} cm^{-3}. In this case the high ohmic p-EPI was used as the investigated effect is more prominent the lower the doping concentration is. Reverse bias voltages from 0 V to 20 V were applied to the diode. The measured and simulated results are shown in Figure 8.16.

For the measurement a sample with a ground surface was used and in the simulation the surface recombination rate was set to $s_0 = 10^5$ cm/s.

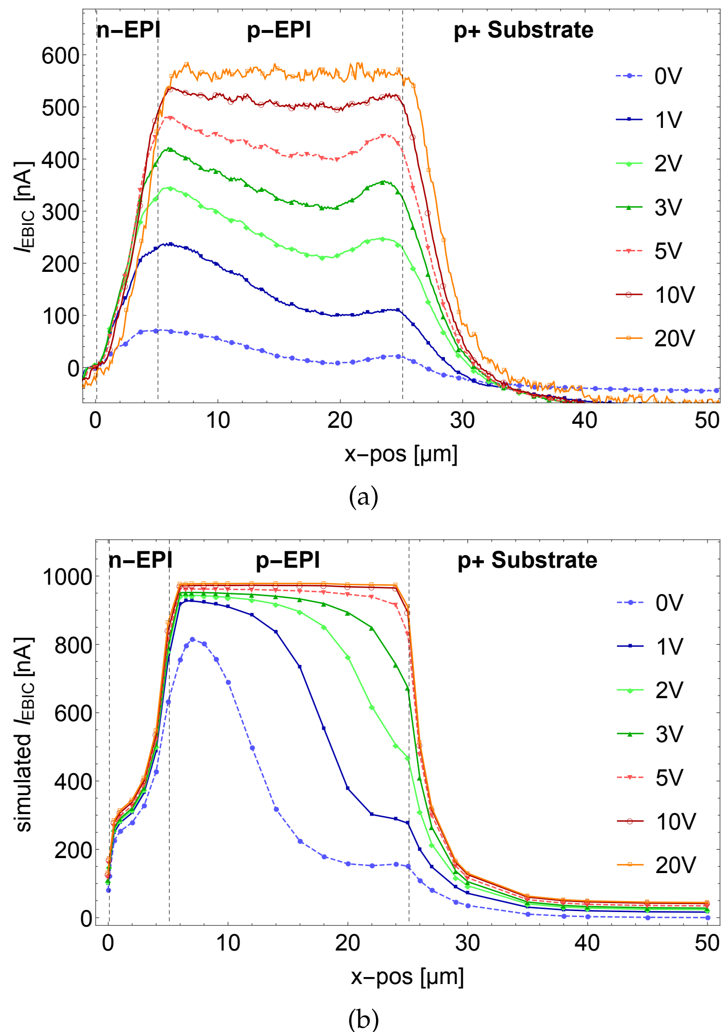

FIGURE 8.16: Influence of reverse biasing of the diode on EBIC signal. (a) Measured EBIC signal and (b) simulated. The reverse bias voltage ranged from 0 V to 20 V. The sample surface was ground in the experimental case and $s_0 = 10^5$ in the simulation. The n-doping concentration was 10^{16} cm^{-3} and the p-doping concentration 10^{13} cm^{-3}.

By applying a voltage in reverse direction the electric field is increased. This goes along with an increase of the space charge region width depending on the doping concentration. The lower the doping concentration the higher the effect. In Figure 8.16 one can also see an increase of the absolute EBIC signal with increasing bias voltage until it saturates between 10 V and 20 V bias. This increase happens due to the increase of dark current with applied reverse bias and the increase of the electric field. The electric field for each bias condition out of simulation is plotted in Figure 8.17.

One would assume that all carriers generated inside the space charge region get separated and no recombination is taking place. But that would also mean that the EBIC signal should be constant inside the space charge region. But looking at Figure 8.17 already starting with 3 V the whole p-EPI region seems to be depleted, as the electric

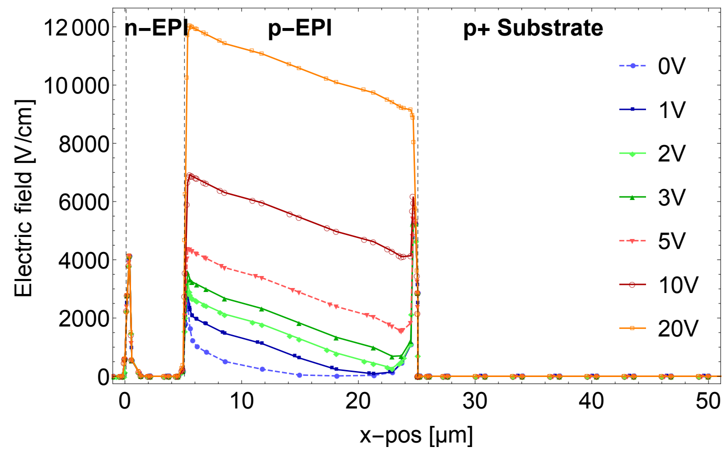

FIGURE 8.17: The simulated electric field distribution at reveres bias voltages from 0 V to 20 V. The n-doping concentration was 10^{16} cm^{-3} and the p-doping concentration 10^{13} cm^{-3}.

field is not zero in the whole p-EPI region. But, the EBIC signal in Figure 8.16 is not constant until 10 V. It seems like a critical electric field, and thus a critical voltage is necessary that all electron-hole pairs are separated and the EBIC signal saturates. The generation of electron-hole pairs by the incoming electron beam remains constant but more charge carriers get separated when the electric field increases.

8.4 Simulation of influence of interface charge and bulk lifetime

Parameters like bulk minority carrier lifetime and charges at the silicon/silicon-dioxide interface and the oxide are hard to investigate experimentally as it is difficult to vary and influence them in a controlled way. However, these parameters will influence the measured EBIC signal. To get an better idea of their influence on the measurement result simulations are done to see the resulting effect. The simulations are done for the experimentally investigated structure and also for a slightly changed structure.

8.4.1 Minority carrier lifetime

To investigate the influence of minority carrier lifetime a symmetric structure, shown in Figure 8.18, is used to cancel out doping and geometry effects. The n-region as well as the p-region were 50 µm thick and the doping concentration was 7×10^{14} cm^{-3} on both sides. In Figure 8.19 the simulated EBIC line-scans for minority carrier lifetime values ranging from 10^{-5} s to 10^{-8} s is shown. The surface recombination rate was fixed to 10^{7} cm/s. One can see that, as expected, the smaller the lifetime the steeper the decay after the junction. A similar effect was already shown in Subsection 8.3.1 investigating the influence of surface recombination rate. Taking a closer look, one can see that the decay is exponential, or linear in a logarithmic plot as stated in Section 6.1. To compare the effect of minority carrier lifetime to surface recombination rate the influence of surface recombination rate is simulated for this symmetric structure. In Figure 8.20 the simulated EBIC signal for surface recombination rates varied from 10^{3} cm/s to 10^{7} cm/s is shown. The used lifetime value was 10^{-5} s. Similar as when varying the

lifetime, the decay gets steeper the higher the recombination rate is. But additionally, also the the deviation from exponential behavior increases. This was already stated in Section 6.1 in theory. These simulation results prove, that even though at first sight, it seems that an decreased lifetime has the same effect on the signal as a increased surface recombination rate, it is possible to distinguish between the two effects by plotting the line-scans in a logarithmic scale.

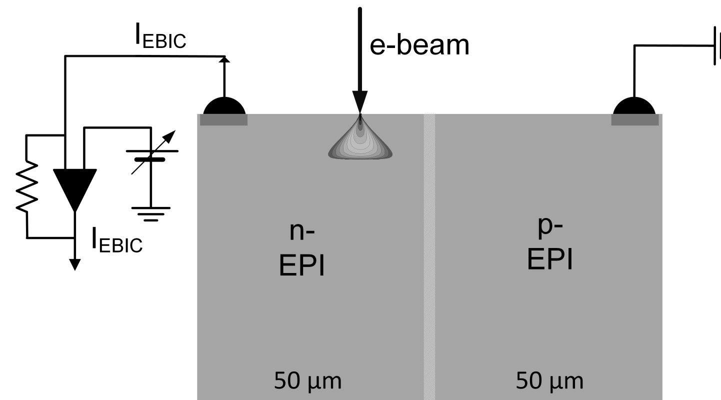

FIGURE 8.18: Schematic structure of symmetric design in cross-section view.

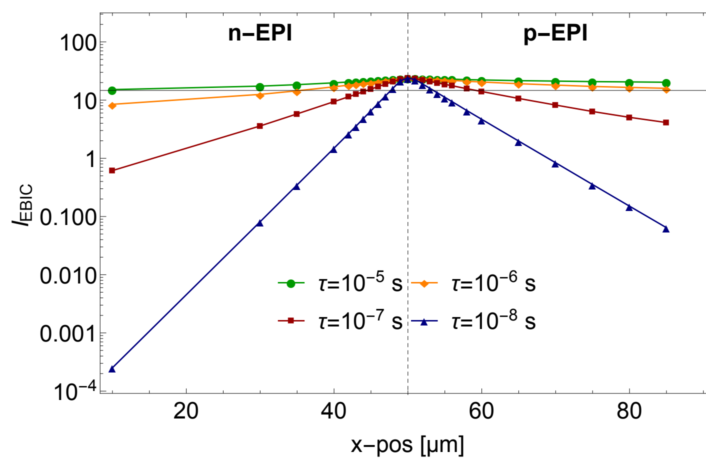

FIGURE 8.19: The simulated EBIC signal for lifetime values ranging from 10^{-5} s to 10^{-8} s. The n- and p-type doping concentration is 7×10^{14} cm^{-3}. The electron beam energy is 10 keV

8.4.2 Surface Charge

Next, the influence of interface charge, which was already shortly introduced in Chapter 4, was investigated. In Figure 8.21 the simulated EBIC signal for the structure used in the experimental measurements (Figure 8.2) is shown for different interface charge values set as positive or negative fixed charges with a uniform distribution [58]. In Figure 8.21a the surface recombination velocity is 10^3 cm/s and in in Figure 8.21b

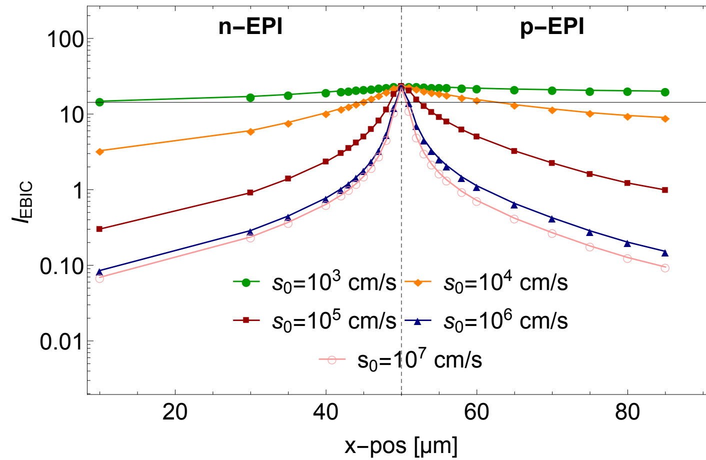

FIGURE 8.20: The simulated EBIC signal for surface recombination rate values ranging from 10^3 cm/s to 10^7 cm/s. The n- and p-type doping concentration is 7×10^{14} cm^{-3}. The electron beam energy is 10 keV

it is 10^6 cm/s. The chosen electron beam energy was 20 keV. Comparing the two plots one can see that the influence of surface/interface charge is more significant in combination with a high surface recombination velocity. The trend shows that on the n-side a positive charge results in an increased EBIC signal. But a very high negative charge of 10^{12} cm^{-3} has the strongest effect. A negative charge with the concentration of 10^{11} cm^{-3} even leads to a slightly decreased signal. The same trend is visible on the p-side with the opposite sign. The charge resulting in a decreased signal is there positive and has a concentration of 10^{10} cm^{-3}. This is one order of magnitude smaller than on the n-side. This asymmetry can be explained by the difference in doping concentration on the two sides. The maximum values are achieved with high positive charges, without a significant difference between a concentration of 10^{11} cm^{-3} and 10^{12} cm^{-3}. In Figure 8.21a the effect seems to be smaller. This is because of the already high signal due to the lack of surface recombination. Still, again a decrease of EBIC signal can be seen on either side of the structure for the same charge types as for the low quality surface. For a better understanding of this behavior, the electron and hole densities and the electric fields were investigated.

At the beginning let us assume a positive charge. A positive charge leads to an accumulation of electrons (Figure 8.22a). The density of electrons accumulated depends on the charge concentration. On the n-side the increased number of electrons acts like a region with higher doping. This results in an electric field pushing down the minority carriers. On the p-side on the other hand the accumulation of electrons leads to the formation of an inversion layer and a field induced junction is formed. [69] This results in a bending of the space charge region towards the p-side and a surface space charge region is formed. The extent of the bending is dependent on the amount of charge placed at the interface. The higher the charge density, the more significant is the bending, and also the depth of the space charge region at the surface. In Figure 8.24 the electric field for the case of a positive surface charge with a density of 10^{11} cm^{-2} is shown for comparison to the case without charge as shown in Figure 8.23. In the case of negative charges the effects are inverted. Instead of electron accumulation there is hole accumulation (Figure 8.22b). This leads to a surface space charge region on the n-side and an electric field because of the higher hole density on the p-side. The explanation given so far would lead to an increased EBIC signal no matter what kind of charge is placed on the n- and p-side, as in all cases the diffusion of minority carriers

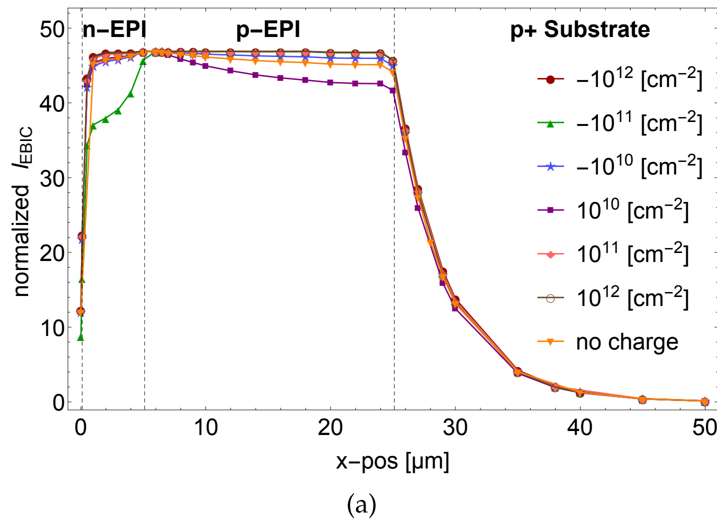

(a)

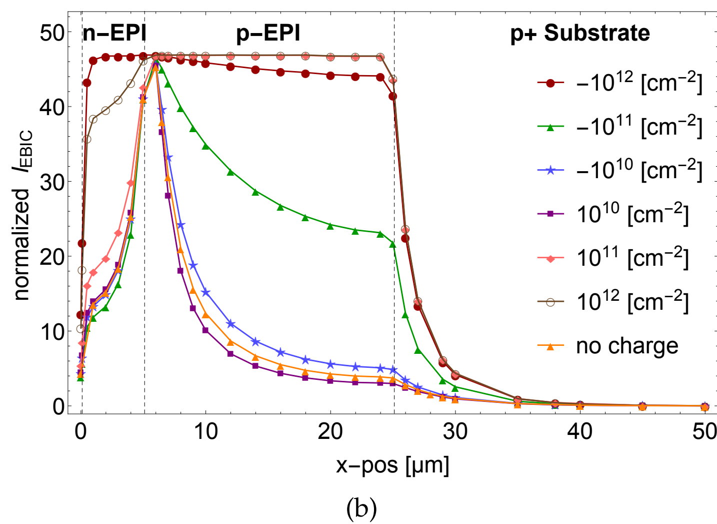

(b)

FIGURE 8.21: The simulated EBIC signal for various negative and positive charge densitties placed at the silicon/silicon-dioxide interface. In (a) the surface recombination velocity is 10^3 cm/s and in (b) 10^6 cm/s. The electron beam energy was 20 keV.

to the surface is restricted or a surface space charge region is formed where no free carriers exist to recombine with. But, looking at the simulation results there are on the *n*- as well as on the *p*-side configurations where the EBIC signal is decreased as shown before. In the case of a positive interface charge density of 10^{10} cm^{-2} the surface depletion region is not very distinct and there is no accumulation of electrons. Still there is a weak electric field (Figure 8.25) due to the charge at the surface. One explanation of the increased surface recombination could be the recombination of the minority carriers, electrons in this case, with the positive charge at the interface as there is no force pushing them away from the interface. This is also supported by the simulation results. The surface recombination is slightly increased in the case of the structure having a interface charge density of 10^{10} cm^{-2}, with respect to a structure without charges placed. In the case of a positive interface charge density of 10^{11} cm^{-2}, there is no surface recombination component as expected. The same observation was made in the case of a negative interface charge density of 10^{11} cm^{-2} (electric field is shown in Figure 8.26), in comparison to a negative interface charge density of 10^{12} cm^{-2} on the *n*-side. The surface recombination, at the *n*-side, of a negative interface charge density

of 10^{10} cm^{-2} (Figure 8.27) is in between the two cases mentioned before.

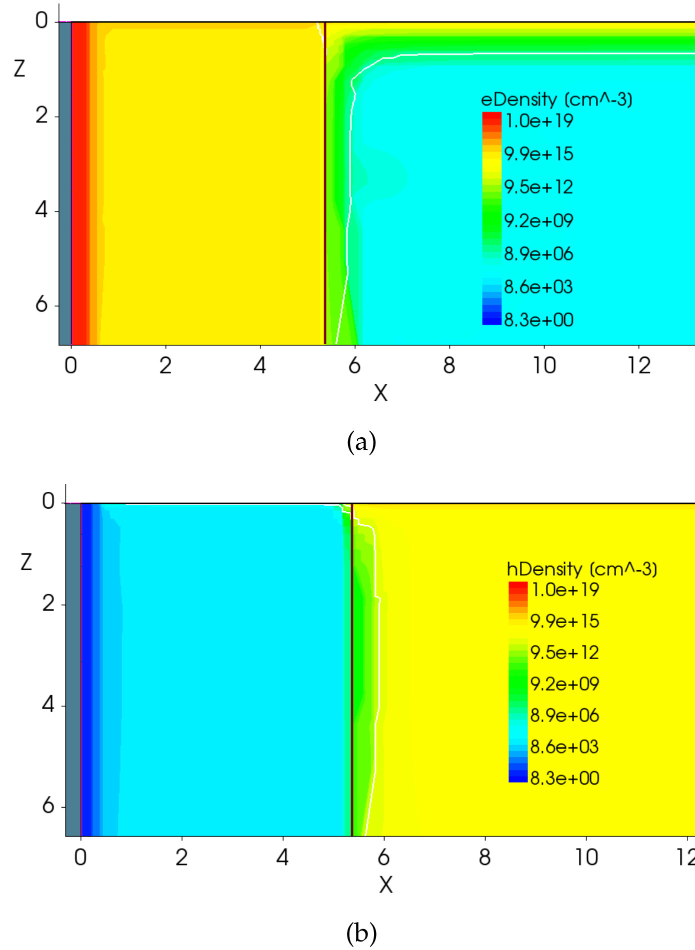

FIGURE 8.22: In (a) the electron density for a positive surface charge density of 10^{11} cm^{-2} is shown. In (b) the hole density for a neative surface charge density of 10^{11} cm^{-2}.

To cancel out the influence of doping concentration and structure asymmetry some simulations were repeated for the symmetric structure introduced before. Due to the long simulation time, an electron beam energy of 10 keV was used for the simulations. In Figure 8.28 the EBIC linescan for positive and negative charge densities of 10^{10} cm^{-2} and 10^{11} cm^{-2} are shown. One can see that with a symmetric structure also the influence of charge on the n-side and the p-side is symmetric.

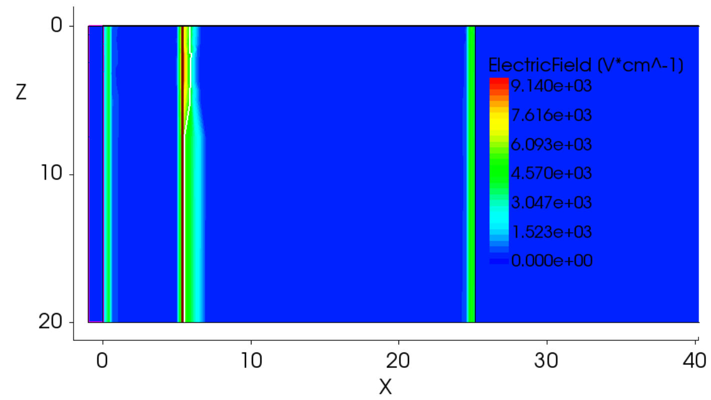

(a)

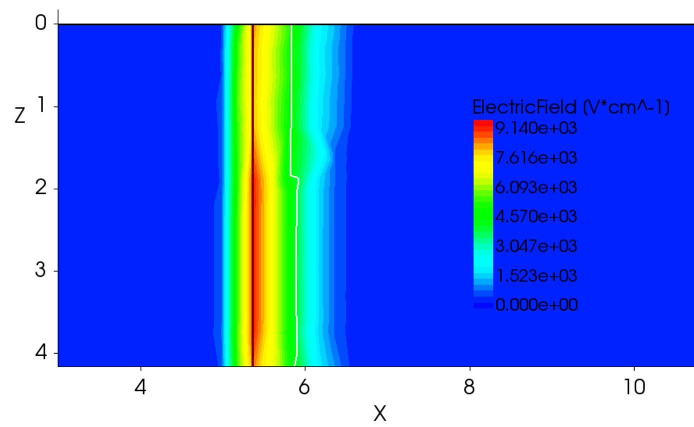

(b)

FIGURE 8.23: The simulated electric field no surface/interface charge. An overview image and zoomed in to the area of the junction

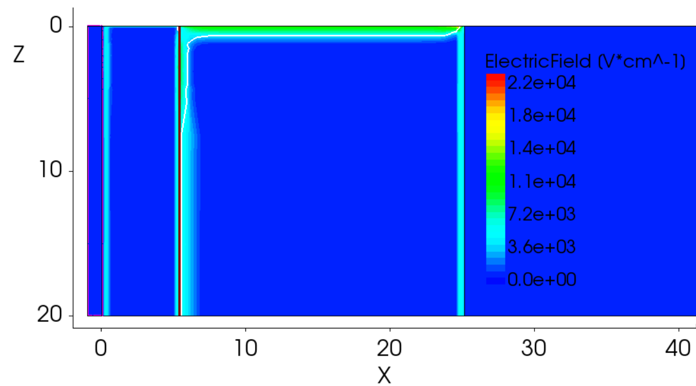

(a)

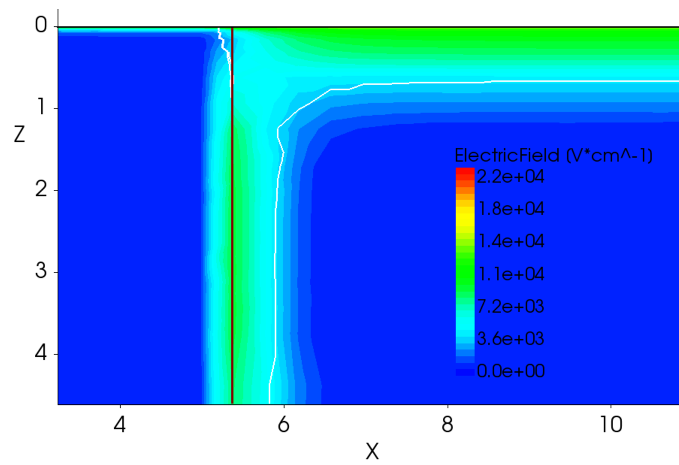

(b)

FIGURE 8.24: The simulated electric field for positive interface charge density of 10^{11} cm^{-2}. An overview image and zoomed in to the area of the junction

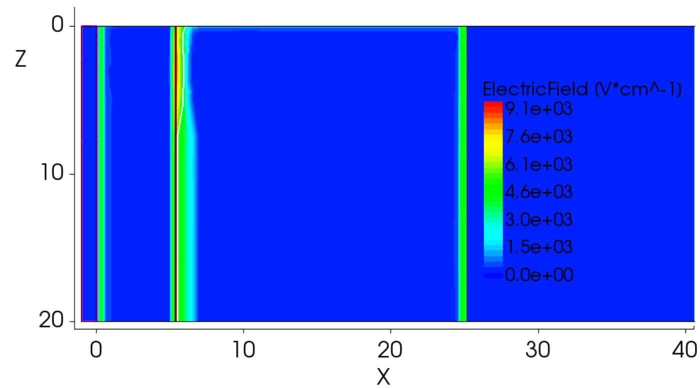

(a)

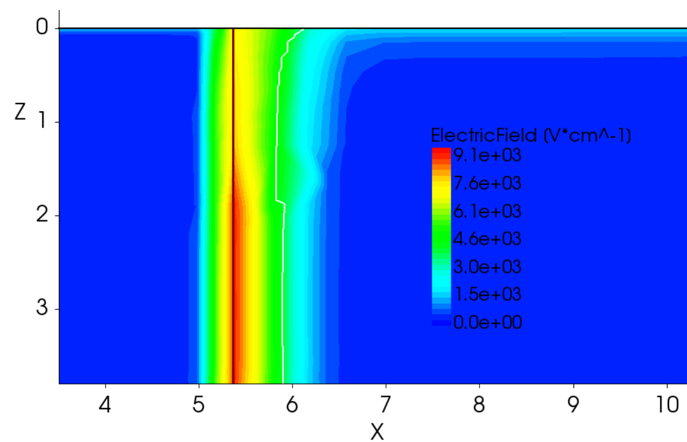

(b)

FIGURE 8.25: The simulated electric field for positive interface charge density of 10^{10} cm^{-2}. An overview image and zoomed in to the area of the junction

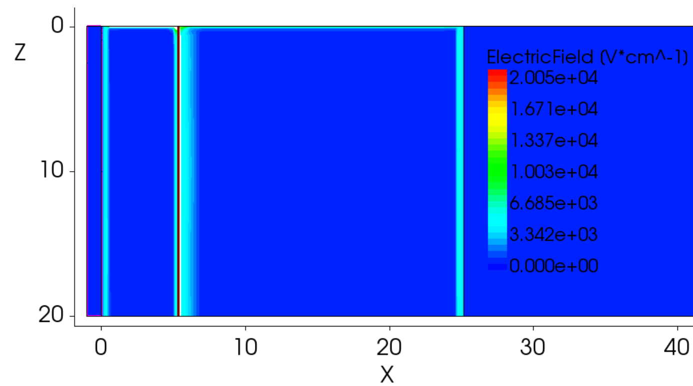

(a)

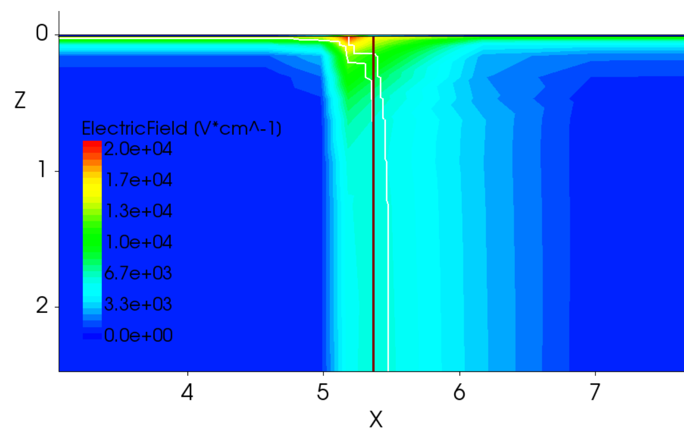

(b)

FIGURE 8.26: The simulated electric field for negative interface charge density of 10^{11} cm^{-2}. An overview image and zoomed in to the area of the junction

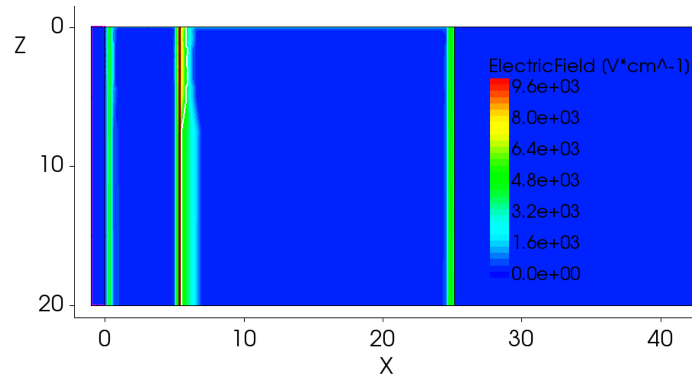

(a)

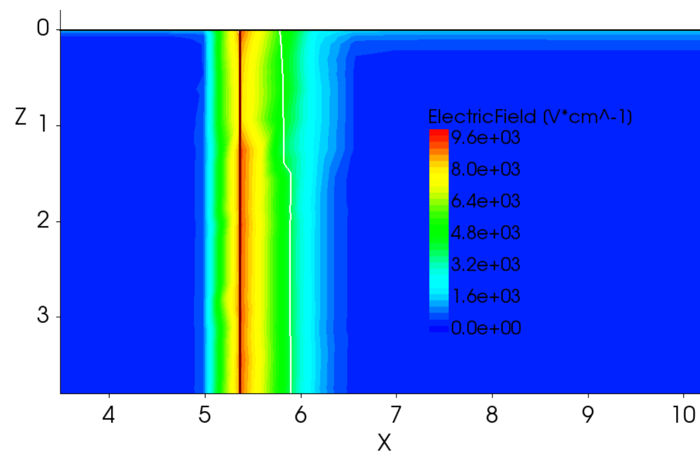

(b)

FIGURE 8.27: The simulated electric field for negative interface charge density of 10^{10} cm^{-2}. A overview and zoomed in to the area of the junction

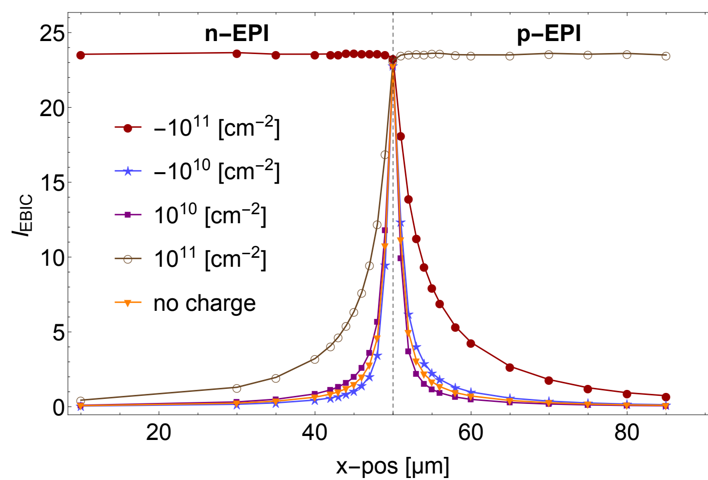

FIGURE 8.28: The simulated EBIC signal for various negative and positive charge densities placed at the silicon/silicon-dioxide interface. The *n*- and *p*-type doping concentration is 7×10^{14} cm^{-3}.

8.5 Extraction of surface recombination velocity

As already mentioned earlier, it is hard to separate recombination at the bulk from recombination at the surface or interface. In the previous sections it was shown how the existence of surface recombination because of a low quality surface can be proven. In this section it is shown how out of a combination of measurement and simulation a quantitative value for the surface recombination rate is extracted. First the method is explained using simulated data and then the concept is applied to experimental data. In Figure 8.29 the simulated EBIC signal in dependence on the electron beam energy (2 keV to 20 keV) is shown for two x-positions. The used structure is the one shown in Figure 8.10. One x-position (46 µm) is on the *n*-side and one (54 µm) on the *p*-side. Furthermore, two surface conditions are compared. A surface recombination rate of 10^3 cm/s and the extreme case of 10^7 cm/s are shown. In Figure 8.29b the normalized EBIC signal is used. This is done to eliminate the influence of increased electron hole pair generation because of the higher energy of the electron beam and thus an increased EBIC current.

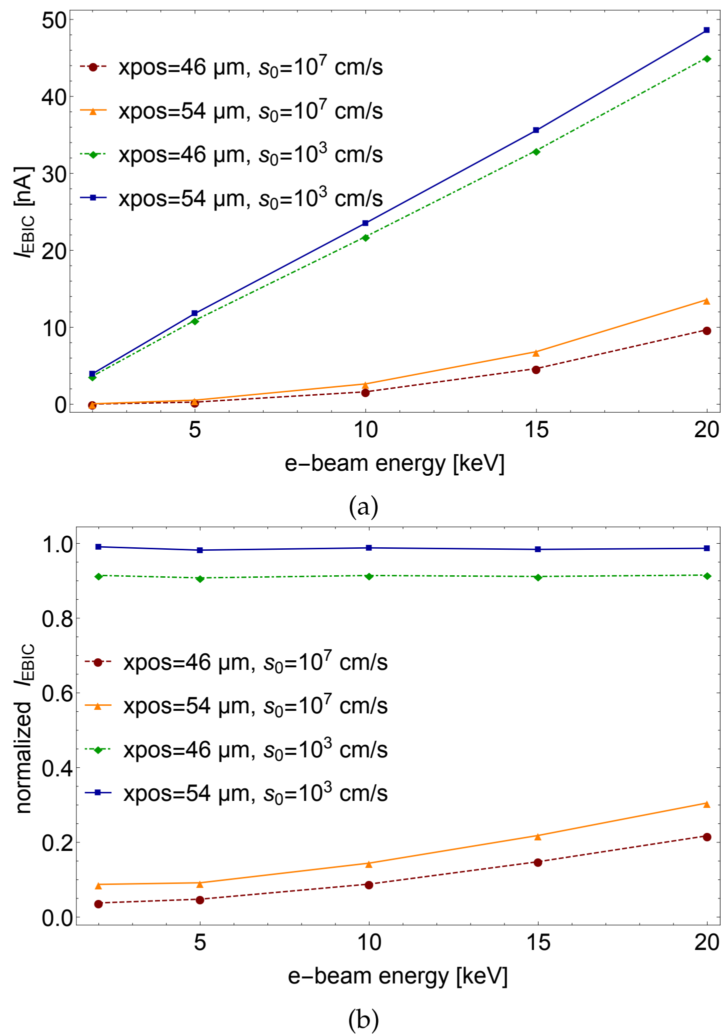

FIGURE 8.29: The simulated EBIC signal at two x-positions (46 µm is on the *n*-side and 54 µm is on the *p*-side) for a surface recombination rate of 10^3 cm/s and 10^7 cm/s in dependence on the electron beam energy is shown in (a) in (b) the normalized signal is plotted.

In Figure 8.29 it can be seen that a low surface recombination rate is leading to a linear dependence on electron beam energy and a constant value in the normalized case. The EBIC signal of a sample with high surface recombination rate shows a non linear behavior, which is also visible using normalized EBIC signals. An increase of EBIC signal with increasing electron beam energy can be seen which is expected according to the results presented in Subsection 8.3.3. In Figure 8.30 the simulated EBIC signal is shown as a function of surface recombination rate for electron beam energies of 2 keV and 20 keV again at the same x-positions.

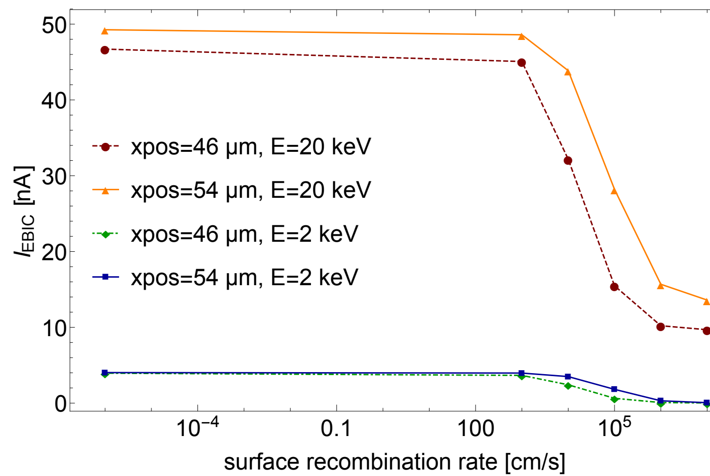

(a)

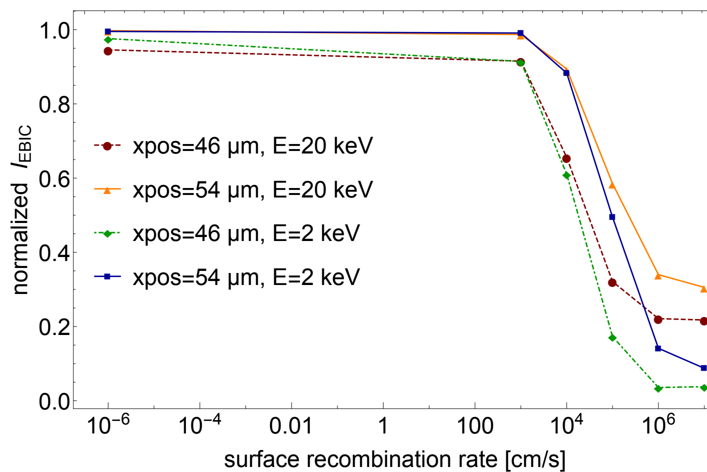

(b)

FIGURE 8.30: The simulated EBIC signal at two x-positions (46 μm is on the *n*-side and 54 μm is on the *p*-side) for electron beam energies of 2 keV and 20 keV in dependence on the surface recombination rate is shown in (a). In (b) the normalized signal is plotted.

By comparing the EBIC signals or the normalized EBIC signals in Figure 8.29 and Figure 8.30 the surface recombination rate can be determined when unknown. This is shown in an example. For this the measurements and simulation of the experimentally investigated structure introduced in earlier sections (Figure 8.1 and Figure 8.2) was used.

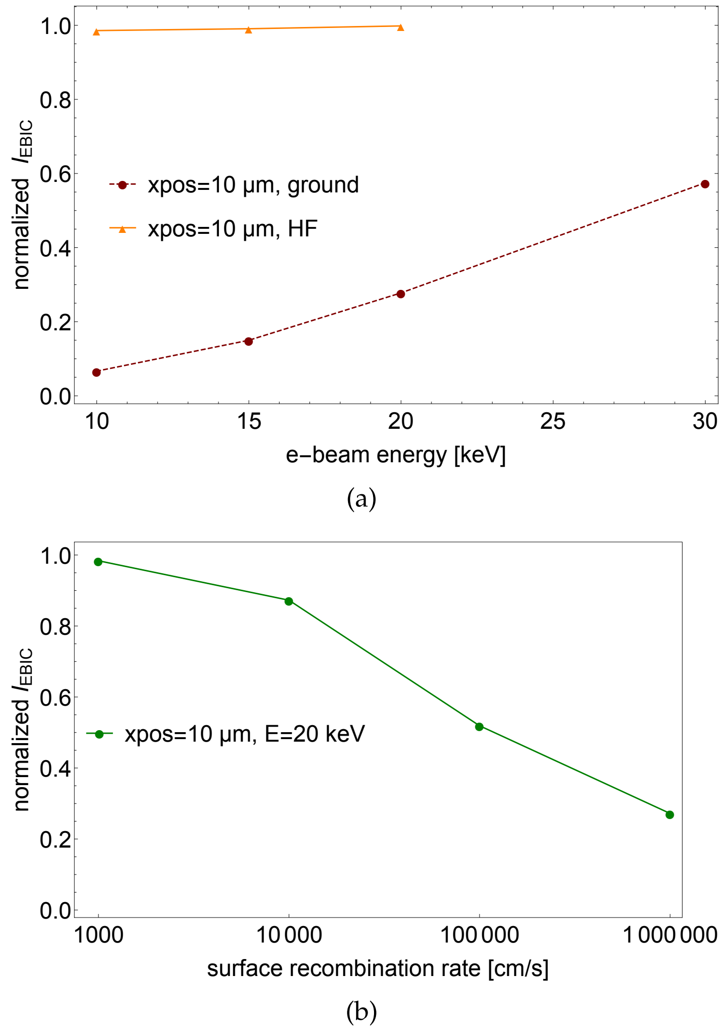

FIGURE 8.31: In (a) the normalized measured EBIC signal is in dependence on the electron beam energy is shown for a ground sample and an HF etched sample. The x-position is in the *p*-region (10 μm. In (b) the simulated normalized EBIC signal is shown at the same x-position in dependence on surface recombination rate. The electron beam energy is 10 keV and 20 keV.

In Figure 8.31a the normalized EBIC values in dependence on the electron beam energy are shown for a ground sample and an HF etched sample and the values ranging from 10 keV to 30 keV are listed in Table 8.1. The x-position is chosen in the *p*-EPI region 4 μm away from the junction in the field free region (x-pos=10 μm). In Figure 8.31b the normalized simulated EBIC values for an electron beam energy of 20 keV is shown for different surface recombination rates (values listed in Table 8.2). The x-position is again 10 μm. In this case the experimental structure shown in Figure 8.1 is used for the simulation.

Comparing now the values listed in the two tables the HF etched sample is in accordance with the surface recombination rate of 10^3 cm/s and the ground sample 10^6 cm/s. At this point this is no new information as already a comparison of the line scans was done earlier (Figure 8.11b). But, in the future with this method it is not necessary to simulate the whole line scan which is very time consuming. It is enough to simulate dedicated points for several surface conditions to fit the surface recombination rate.

TABLE 8.1: Normalized measured EBIC signals for different electron beam energies of a ground sample and an HF etched sample. The x-position is 10 µm.

Electron beam energy [keV]	norm I_{EBIC} ground sample	norm I_{EBIC} HF etched sample
10	0.067	0.986
15	0.15	0.991
20	0.278	0.998
30	0.575	

TABLE 8.2: Normalized simulated EBIC signals for different surface recombination rates. The electron beam energy is 20 keV and the x-position is 10 µm.

Surface recombination rate [cm/s]	norm I_{EBIC} 20 keV
10^3	0.984
10^4	0.873
10^5	0.529
10^6	0.272

8.6 Conclusions from EPI diode investigations

In this chapter, measurements and simulations on simple step junction like EPI photodiodes were shown. The rather simple structure was very suitable to calibrate and test the simulation set up. It was shown that measurements and simulation are in very good agreement. A very big influence of the surface preparation on the EBIC signal was observed and reproduced by varying the surface recombination rate in simulations. Using this knowledge the electron beam energy dependence of the EBIC signal can be used as indicator for surface quality. In further investigations special care has to be taken on which surface treatment to use, depending on the goal of the investigation.

Chapter 9

EBIC testchip

The results achieved from the EPI diodes and presented in Chapter 8 gave a very good first impression of the EBIC measurement method. A lot of information could be gained about factors influencing the EBIC signal and thus the recombination mechanisms in a sample. With the help of these quite simple structures, the EBIC TCAD environment was calibrated and is well understood at this point. The next step was to investigate structures reflecting real process conditions and their influence on carrier transport and to avoid the neccessity of measuring on a cross-section. For this reason a dedicated EBIC testchip was developed and processed in a CMOS 0.35 high voltage process flow [70]. This process offers a lot of possible well combinations which can be used as photodiode structures [71]. This test-chip was used to investigate the carrier transport depending on substrate type, doping concentration and diode design variations. In order to be able to measure diffusion lengths in high quality substrates in an EBIC top-view mode, the structure size had to be chosen accordingly.

9.1 The test structure

Circular diffusion *n*-wells were fabricated in variously doped *p*-substrates. Four of the investigated substrates were EPI Wafers with varying *p*-EPI doping concentration. In addition, also a standard wafer with a resistivity of 20 Ωcm was processed. The *p*-EPI resistivities were 20, 100 and 200 Ωcm respectively. On either side of the circular wells, substrate contacts that stretch over the whole region were placed. The structure is shown in Figure 9.1. Two size variations were processed for different investigations. In the smaller structure the distance between *n*-well and substrate contact is 100 µm while in the larger structure the distance is 700 µm.

Three different *n*-well configurations were processed which vary in doping concentration and depth. The shallowest and highest doped is the *n*+-well. The NW well is a bit deeper and lower doped. Followed by the DN and DN2 diffusions. They have the same depth and are deeper than the NW. The difference is the lower doping concentration of the DN2 compared to the DN. The investigations done until now showed a very strong influence of surface condition on the recombination processes. To further investigate this, two design variations were developed. In one case, to avoid surface recombination, a surface passivation was done. The surface passivation was achieved by a shallow very highly doped *p*-layer at the surface. This surface layer results in an electric field pointing from the surface to the bulk that forces the minority carriers, in this case electrons, away from the surface towards the bulk. For comparison, also structures without surface passivation were processed. In Figure 9.2 (a) and (b) respectively the two design variations are shown.

TABLE 9.1: List of designs investigated

Surface	n-well	Substrate
unpassivated	n+	bulk 20 Ωcm supplier 1 18 µm EPI 20 Ωcm supplier 1 14 µm EPI 20 Ωcm supplier 2 14 µm EPI 100 Ωcm supplier 2 14 µm EPI 200 Ωcm supplier 2
	NW	bulk 20 Ωcm supplier 1 18 µm EPI 20 Ωcm supplier 1 14 µm EPI 20 Ωcm supplier 2 14 µm EPI 100 Ωcm supplier 2 14 µm EPI 200 Ωcm supplier 2
	DN	bulk 20 Ωcm supplier 1 18 µm EPI 20 Ωcm supplier 1 14 µm EPI 20 Ωcm supplier 2 14 µm EPI 100 Ωcm supplier 2 14 µm EPI 200 Ωcm supplier 2
	DN2	bulk 20 Ωcm supplier 1 18 µm EPI 20 Ωcm supplier 1 14 µm EPI 20 Ωcm supplier 2 14 µm EPI 100 Ωcm supplier 2 14 µm EPI 200 Ωcm supplier 2
passivated	n+	bulk 20 Ωcm supplier 1 18 µm EPI 20 Ωcm supplier 1 14 µm EPI 20 Ωcm supplier 2 14 µm EPI 100 Ωcm supplier 2 14 µm EPI 200 Ωcm supplier 2
	NW	bulk 20 Ωcm supplier 1 18 µm EPI 20 Ωcm supplier 1 14 µm EPI 20 Ωcm supplier 2 14 µm EPI 100 Ωcm supplier 2 14 µm EPI 200 Ωcm supplier 2
	DN	bulk 20 Ωcm supplier 1 18 µm EPI 20 Ωcm supplier 1 14 µm EPI 20 Ωcm supplier 2 14 µm EPI 100 Ωcm supplier 2 14 µm EPI 200 Ωcm supplier 2
	DN2	bulk 20 Ωcm supplier 1 18 µm EPI 20 Ωcm supplier 1 14 µm EPI 20 Ωcm supplier 2 14 µm EPI 100 Ωcm supplier 2 14 µm EPI 200 Ωcm supplier 2

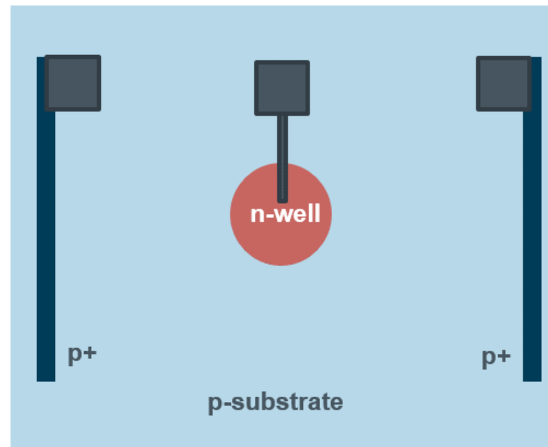

FIGURE 9.1: Top view of schematic structure of test chip.

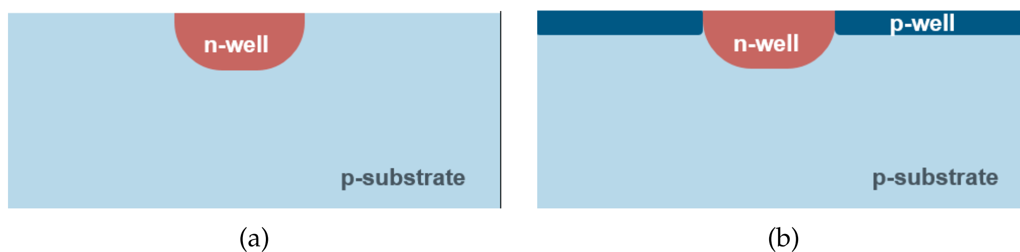

(a) (b)

FIGURE 9.2: Cross-section of schematic structure. In (a) the standard *n*-well in p-substrate structure is shown and in (b) the structure with surface passivation included is shown.

9.2 Sample preparation

A challenge of EBIC investigation of samples gone through a full CMOS process flow lies in the back end of line (BEOL) oxide stack. This stack consists, depending on the process, of multiple layers of silicon dioxide. The so called inter-metal-dielectric (IMD) is used to separate the different metal layers of an integrated circuit. A schematic built-up of the BEOL on top of a photodiode structure is shown in Figure 9.3.

The thickness of this stack can be up to several µm of silicon dioxide. During an EBIC measurement, the incident electrons from the beam could not pass through this oxide layer and no EBIC signal is generated. Because of this, a way has to be found to eliminate this stack in the region of interest, without influencing the silicon surface. The first approach was to use anisotropic plasma etching as a first etch step. In plasma etching silicon dioxide is etched selectively without harming the contact metalization. As plasma etching is a very destructive process that would significantly influence the silicon surface, the process is stopped before reaching the silicon surface. The remaining oxide is eliminated by a short dip in HF. Special care has to be taken not to etch too long as this is an isotropic etching process with the danger of an under-etch of the contacts. The right timing has to be found to ensure good contact properties with maximum removal of the oxide.

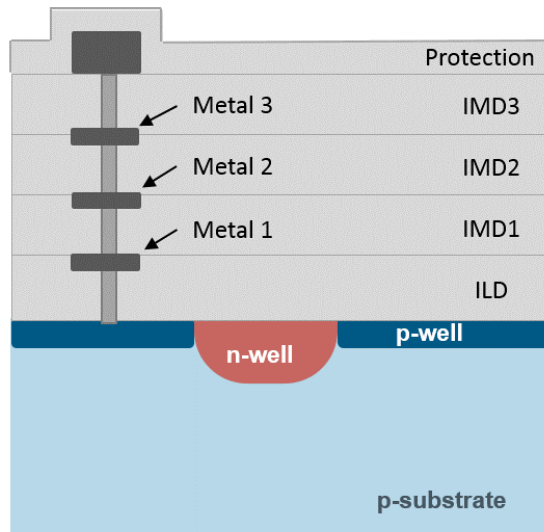

FIGURE 9.3: Schematic built up of test chip including back end of line stack.

9.3 Influence of sample preparation

For first tests and a calibration of the etching process, several samples of one type were etched. EBIC measurements were performed on several test structure types on several samples. Test structures including the surface passivation layer showed the same result for every tested sample. Structures without surface passivation on the other hand showed a big variance over tested samples. From this, two conclusion are drawn. First that the etching process is not very reproducible and second that the surface passivation is working very well. While with surface passivation there is no influence of surface treatment on the EBIC signal the influence is severe in the case of the unpassivated structure. In Figure 9.4 the SEM image and the corresponding EBIC image of a surface passivated test structure is shown. The structure is a lightly doped deep n-well and the electron beam energy was 20 keV.

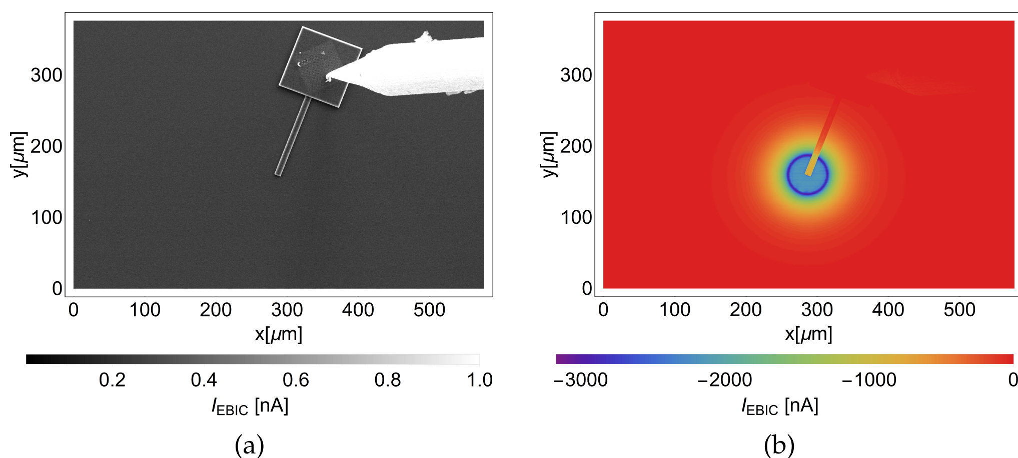

FIGURE 9.4: 2D EBIC signal of a passivated structure. In (a) the SEM image is shown and in (b) the corresponding EBIC image.

In Figure 9.5 the first example of a structure without surface passivation is shown. The

diffusion length seems to be much shorter than for the surface passivated structure. Additionally, the diffusion region is not as homogeneous. In Figure 9.5a the first recorded image is shown while in Figure 9.5b the same area is shown but with some time scanning across the sample zoomed in on the center of the structure. One can see that the observed region shows an increased EBIC signal. From this, an influence of the electron beam on the surface has to be concluded. For the case of the surface passivated structure such a behavior was not observed. In Figure 9.6 the EBIC signal of a a unpassivated structure on a second sample is shown. Again Figure 9.6a shows the first recorded and Figure 9.6b shows the signal after scanning some time with the electron beam over the sample. Again the area from which a significant EBIC signal is collected has grown.

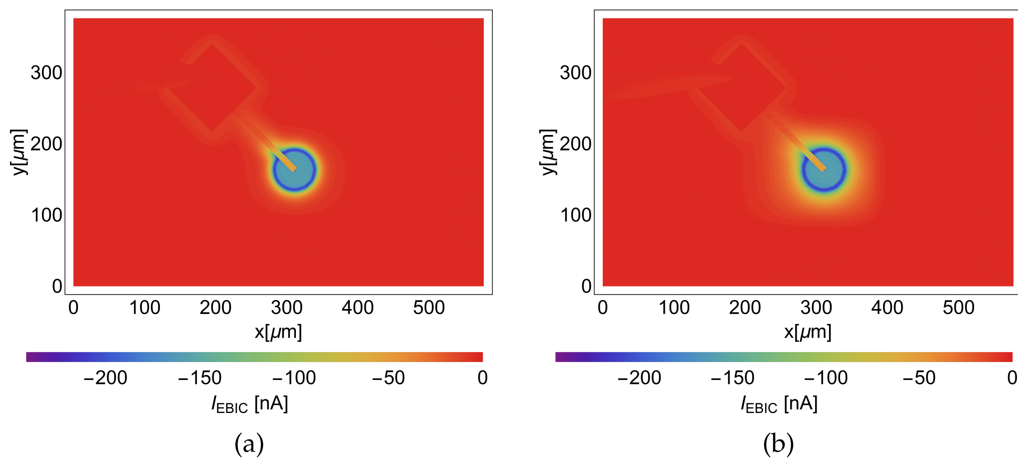

FIGURE 9.5: 2D EBIC signal of a unpassivated structure of an over-etched sample. In (a) the first recorded image is shown while in (b) the same image was recorded after watching several minutes zoomed in.

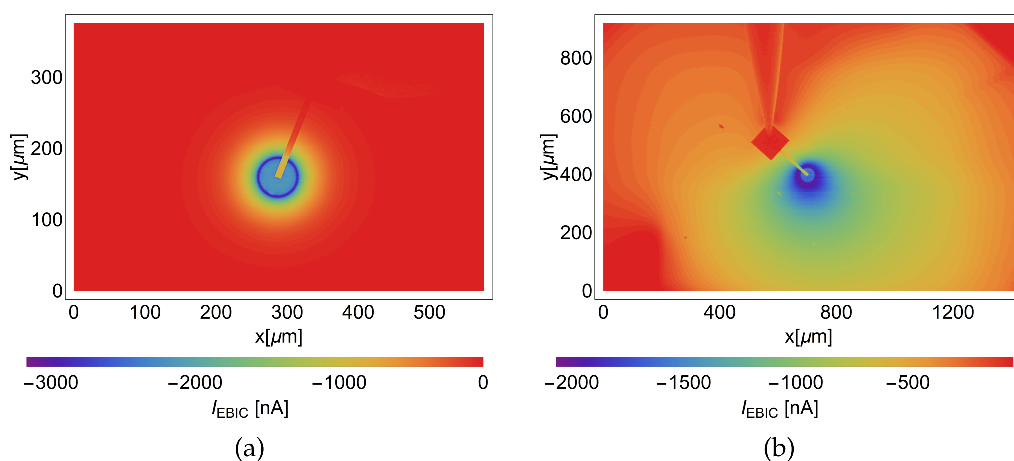

FIGURE 9.6: 2D EBIC signal of a unpassivated structure of a sample with residual oxide. In (a) the first recorded image is shown while in (b) the same image was recorded after watching several minutes.

Additionally to the EBIC structures, also standard *n*-well in *p*-substrate photodiode structures were placed on the test chip. Theses structures can be used to investigate the photodiode behavior in the classical way after different sample treatments. Spectral responsivity measurements were done on an unetched sample and two different etched samples. The result of the optical responsivity measurements give first of all information about the thickness of the oxide which is influencing the interference pattern of the signal. The interference pattern is due to reflection of the incoming light at the air/silicondioxide and silicondioxide/silicon interface [72]. The modulation of the pattern is dependent on the thickness of the oxide. The thicker the oxide the more fringes are observed. A second effect that can be seen in the measurement shown in Figure 9.7 is that the two etched samples show differences in responsivity at short wavelengths. This provides further evidence for the difference in surface quality of these two samples. A reduced spectral responsivity in the blue region corresponds to higher recombination in the surface area as this is the region were light in this wavelength range is absorbed. At longer wavelengths were the absorption takes place in deeper regions in the bulk, the surface damage has only very little effect [23].

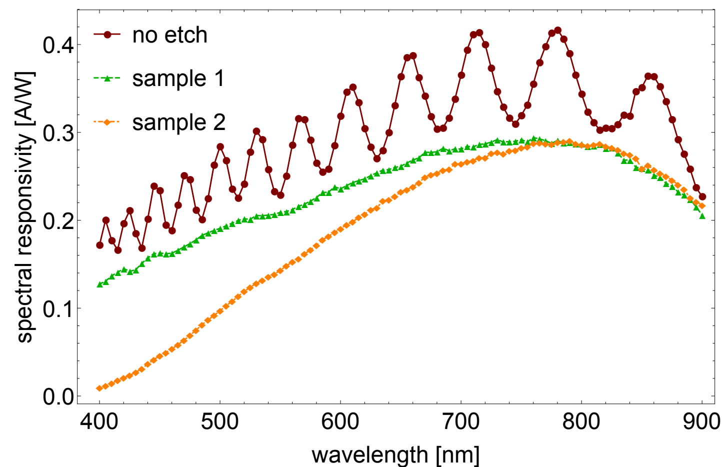

FIGURE 9.7: Spectral responsivity in A/W for an unetched and two etched samples.

In order to eliminate the uncertainty of the etching process. A more controlled etching procedure was implemented during the fabrication of the wafer. A mask supported oxide etch process was used to eliminate the BEOL oxide in the areas of interest but to keep it in the contact areas (see schematic in Figure 9.8). The plasma etching stops several 100 nanometers before the silicon. Thus, a protective oxide remains but it is thin enough to perform EBIC measurements. Additionally, a sample group was produced where the residual oxide left after plasma etching was removed by an HF dip.

In Figure 9.9 the spectral responsivity, measured on the rectangular test diodes is shown. The aforementioned preparation methods are compared. The difference in oxide thickness can be seen in the variation of the interference pattern as explained above. The mask etched sample has fewer fringes but still a interference pattern is visible because of the residual oxide left. The sample after HF dip shows no interference pattern anymore. This indicates that there is no oxide left. Furthermore, a severe reduction in the short wavelength region can be seen leading to the conclusion that the surface region is disturbed by the etching. This is quite unexpected as in Chapter 8 it

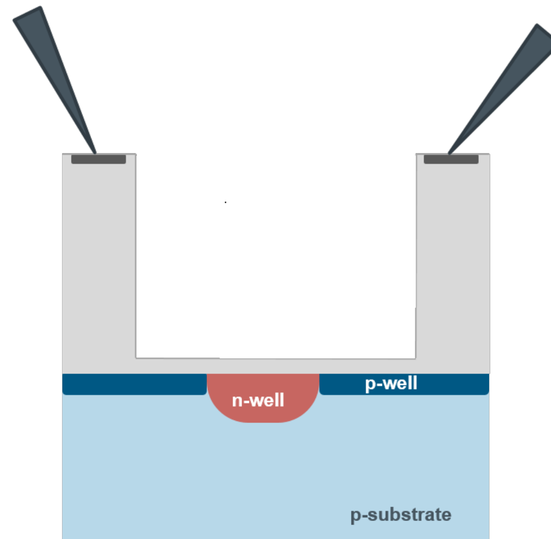

FIGURE 9.8: Schematic of the test chip including BEOL stack after BEOL etching.

was shown that HF etching results in a very high quality surface.

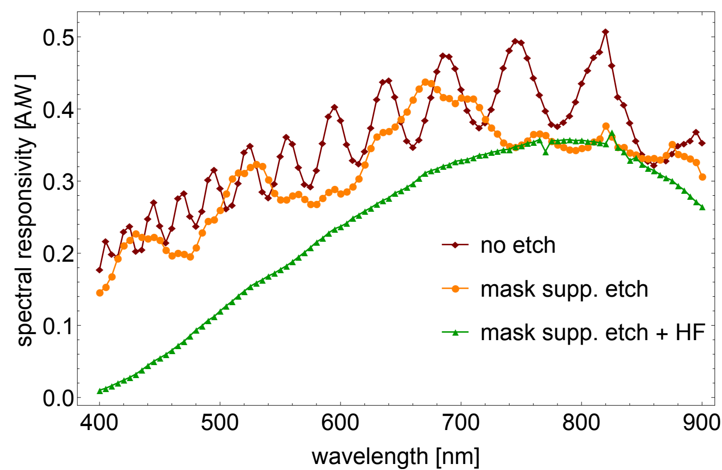

FIGURE 9.9: Spectral responsivty in A/W of rectangular test diode. Comparison between an unetched sample, a sample with mask etching and a sample with mask etching with subsequent HF etching.

With this dedicated etching process a reproducible sample preparation method is developed making the comparison of different samples possible.

9.4 Determination of diffusion length

In the next step the influence of different p-substrates was investigated. The comparison is done between the different substrate types introduced in Section 9.1 in Table 9.1 and the influence of preparation method was investigated. To extract the diffusion length out of the measurements, line scans are extracted from the 2D measurements and the diffusion length is determined as proposed in Section 6.1 using Equation 6.3.

TABLE 9.2: Sample description and acronyms.

Acronym	Substrate	Preparation method
Sample 1	18 µm EPI 20 Ωcm supplier 1	Mask etching
Sample 2	14 µm EPI 20 Ωcm supplier 2	Mask etching
Sample 3	14 µm EPI 100 Ωcm supplier 2	Mask etching
Sample 4	14 µm EPI 200 Ωcm supplier 2	Mask etching
Sample 5	Bulk substrate 20 Ωcm supplier 1	Mask etching
Sample 6	18 µm EPI 20 Ωcm supplier 1	no etching
Sample 7	18 µm EPI 20 Ωcm supplier 1	Plasma etching + HF etching

As we are using very high quality material very long lifetimes are expected. In order to collect all generated carriers long measurement times have to be used (at least in the order of the minority carrier lifetime). First measurements were done on samples without any surface treatment processed in an only two metal process. In this process the BEOL oxide is thin enough to allow reasonably high EBIC signals, using a 20 keV electron beam energy. These results are further compared with measurements done on samples with dedicated mask etching and a measurement done on a sample with Plasma etching followed by HF etching. The different samples discussed in this section are listed in Table 9.2.

In Figure 9.10 an example is shown how the line scan is extracted from the 2D EBIC signal. Using the analytical model, introduced in Section 6.1, the influence of the injection level and thus the used electron beam current has to be taken into account as discussed by [22]. As also already pointed out by Marcelot et al, rather high beam currents are necessary to ensure a good signal to noise ratio which can result in operation in high injection. In Figure 9.11 the EBIC linescans of an exemplary sample are shown for 200 pA and 800 pA electron beam current respectively. The differences in extracted

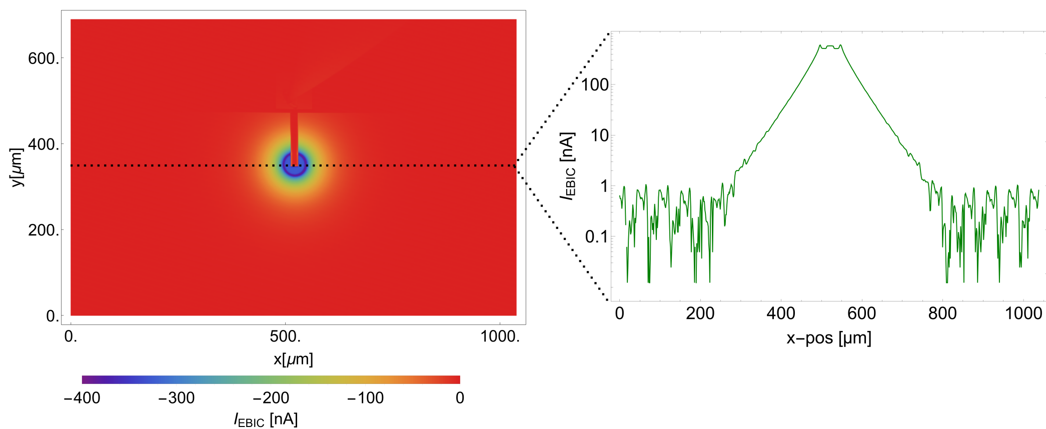

FIGURE 9.10: 2D EBIC signal used for extraction of diffusion length and extracted linescan. The beam energy was 20 kev and the beam current 200 pA.

values are insignificantly small. They vary between 0.5 µm and 2 µm. These differences are within the differences between different measurements of same samples done on different days. No clear trend of a higher recombination length extracted when using a higher beam current as discussed in [22] was observed.

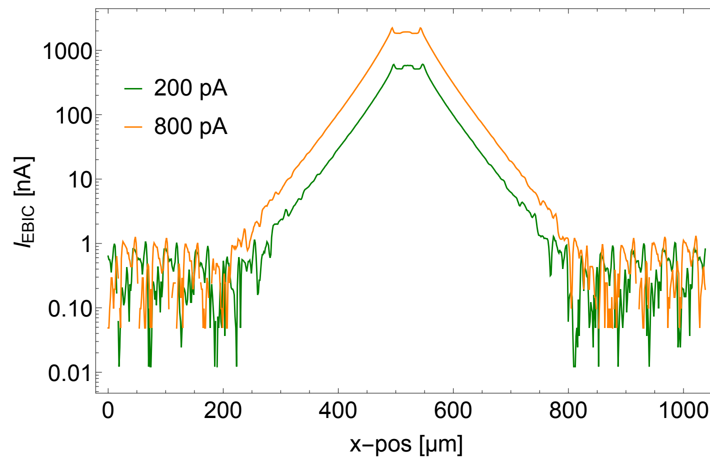

FIGURE 9.11: Comparison of EBIC linescans measured with a beam current of 200 pA and 800 pA respectively. The electron beam energy was 20 keV in both cases.

For the comparison of different starting materials and the extraction of diffusion lengths, an electron beam energy of 20 keV was used. The comparison of the extracted line scans, done with a beam current of 200 pA, for samples with dedicated mask etching and surface passivation are shown in Figure 9.12.

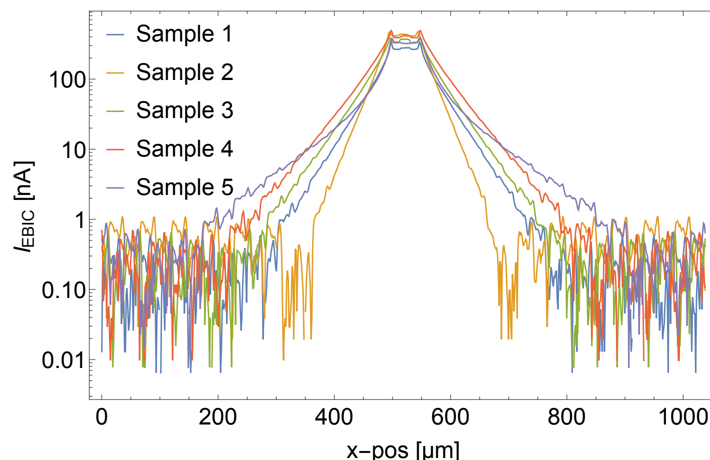

FIGURE 9.12: EBIC linescans of various substrate types. The investigated structures were NW with surface passivation. Electron beam energy was 20 keV and electron beam current was 200 pA.

In Figure 9.13 the line scans of the bulk substrate is compared to the line scan of the EPI substrate of the same supplier with same resistivity. The shape of the decay of the bulk substrate (Sample 5) varies significant from the one of the EPI substrate and

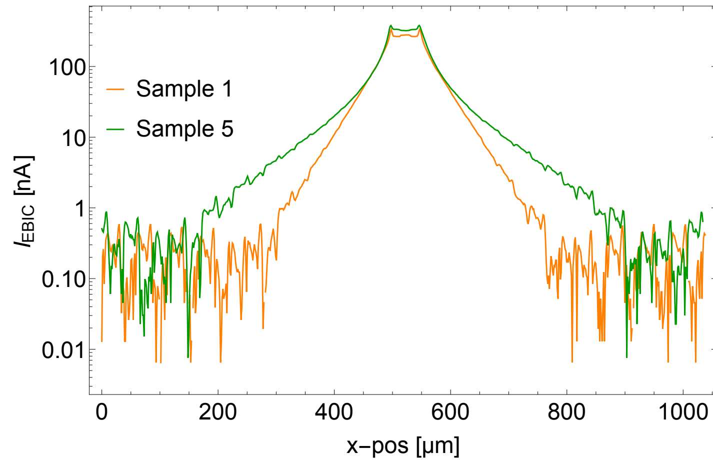

FIGURE 9.13: EBIC linescans of Sample 1 and Sample 5. Comparison between bulk substrate and EPI substrate with same resitivity and from the same supplier. The investigated structures were NW with surface passivation. Electron beam energy was 20 keV and electron beam current was 200 pA.

TABLE 9.3: Extracted diffusion lengths from measurements with a beam current of 200 pA and 800 pA.

Sample	extr. diffusion length 200 pA	extr. diffusion length 800 pA
Sample 1	32 µm	33 µm
Sample 2	21 µm	20 µm
Sample 3	36 µm	36 µm
Sample 4	43 µm	44 µm
Sample 5	69 µm	63 µm
Sample 6	27 µm	27 µm
Sample 7	20 µm	23 µm

is not exponential anymore. The diffusion length is extracted from the region further away from the junction where it follows an exponential decay. As expected the higher the substrate resistivity, and thus the lower the doping concentration, the longer is the extracted diffusion length. The extracted diffusion lengths listed in Table 9.3 are shorter as expected according to lifetime specifications of the wafer supplier. One has to take into account that the diffusion length within the EPI material is not only restricted by lifetime in the EPI layer but also by the thickness of the EPI layer. This can explain the rather short diffusion lengths as diffusion is limited by the vertical extension of the EPI layer. Comparing Sample 1 and Sample 2 one can see a quite significant difference in diffusion length even though the resistivity is the same. One explanation can be the difference in quality between the two suppliers. The second possible explanation which is more likely is the difference in EPI thickness. While Sample 1 has a thickness of 18 µm, Samples 2 to 4 have a EPI thickness of 14 µm. As expected the diffusion length of the bulk substrate is longer than for the EPI substrates as the diffusion is not limited by the EPI thickness. Additionally to diffusion lengths extracted from mask etched samples, also the values for a not etched sample and a sample after large area plasma etching with subsequent HF dip are shown. The diffusion length values vary a bit, depending on the preparation method. It seems like that even though the surface is passivated, a small effect on the extracted diffusion length is observed.

In the case of structures with surface passivation, the decay of the EBIC signal after the space charge region follows the theoretically expected exponential decay. As stated in Section 6.1 this is another indication for a good surface quality. A deviation from this shape is an indication that the surface recombination rate influences the overall diffusion process. Also unpassivated structures were investigated according to diffusion length and line scans are extracted. Again the measurements were done using 200 pA and 800 pA. As already shown before, structures without surface passivation are very sensitive to measurement conditions. In Figure 9.14 the extracted line scans are shown for a measurement done with 200 pA and 800 pA. Using 800 pA the EBIC signal changed with time of observation. To show this effect two linescans recorded with 800 pA are shown. The two images were recorded right after each other. This shows the fast increase in surface recombination at this high electron currents. Furthermore the non-ideal behavior of the unpassivated structure can be seen in the shape of the decay.

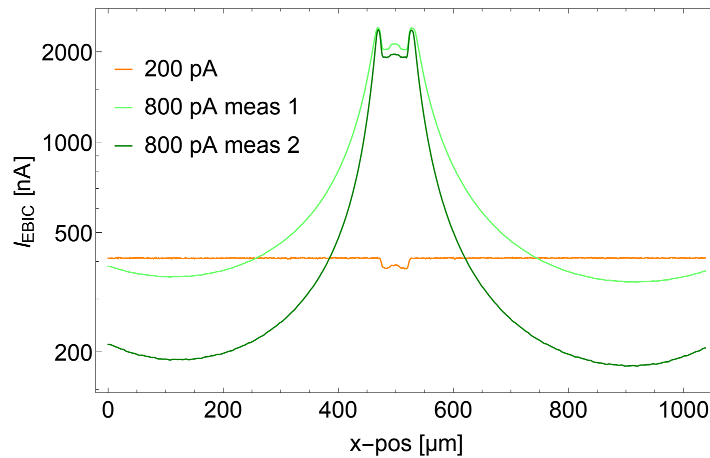

FIGURE 9.14: EBIC linescans of a unpassivated NW design. Electron beam energy was 20 keV and electron beam current was 200 pA and 800 pA respectively.

Comparing these results with the line scans extracted from the measurements of the unpassivated structures, a non-ideal behavior is shown very clear. In Figure 9.15 the comparison of a NW structure for the passivated and unpassivated case is shown. The shape of the decay is very different.

These results show that the unpassivated structure is not suitable to extract the diffusion length of substrate materials as the influence of the electron beam on the surface recombination and thus on the extracted diffusion length, is very strong. The passivated structures on the other hand show a very stable signal not depending on surface preparation or electron beam current. But, one has to be aware that the surface passivation layer still influences measured diffusion lengths as with 20 keV electron beam, a big part of the generated electron hole pairs are generated inside the highly doped surface region. Another point one has to be aware of is that in the case of EPI wafers, not just the diffusion length in the EPI region is measured but also the influence of EPI thickness which is limiting the diffusion in vertical direction.

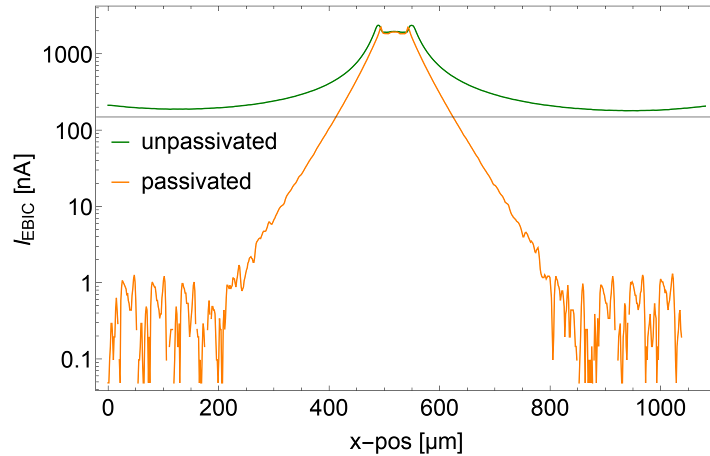

FIGURE 9.15: EBIC linescans of a NW design with and without passivation. Electron beam energy was 20 keV and electron beam current was 800 pA.

9.5 Influence of *n*-well type

As already described in Section 9.1, different *n*-well types were processed. The *n*-wells are processed as diffusion wells. Both, the difference in doping concentration and the well depth, influence the EBIC signal. Measuring these diodes in top-view mode, as already shown in Chapter 6 in Figure 6.2 one has to distinguish two different regions of the junction. One region is the vertical junction formed at the surface and the other region is the horizontal junction in the bulk. By examining the vertical junction, the influence of the doping concentration can be investigated. Measuring with a fixed electron beam energy and comparing the different *n*-well structures, doping dependent differences affecting the space charge region width can be seen. In Figure 9.16 the 2D EBIC signals for all *n*-well types are shown at a fixed electron beam energy of 20 keV and a beam current of 0.8 nA. Comparing Figure 9.16 (b) to (d) the increase of space charge region width with decreasing doping concentration can be seen. The EBIC signal of the *n*+-well structure (Figure 9.16a) does not show the significant ring shaped area with maximum signal, indicating the space charge region. This is because the *n*+-well is very shallow and the vertical junction as well as the horizontal junction contribute the same way at this electron beam energy. Furthermore, even though the *n*-well size is not big enough to show the complete decay after the junction, differences are visible especially between the DN and DN2 where the well depth is the same and only the doping concentration is different. The deeper the well the lower is the signal coming from generation inside the *n*-region. This can be seen comparing Figure 9.16 (a) to (c). Looking at Figure 9.16 (c) and (d) one can see, that independent of the well depth, with lower doping concentration the collected current coming from the *n*-region gets higher. This can be explained by the minority carrier lifetime dependence on doping concentration. In Figure 9.17 the comparison between the different *n*-well types is done using line scans for an electron beam energy of 10 keV, 20 keV and 30 keV respectively.

The second parameter, the well depth, can be investigated in more detail by measuring one well type using different electron beam energies. The higher the electron beam energy, the larger the EBIC signal coming from the horizontal junction region, up until the point where it is the same as for the vertical junction region. This point is of course also dependent on the depth of the well and thus the junction. The closer the junction is to the surface, the smaller the electron beam energy needed to generate electron

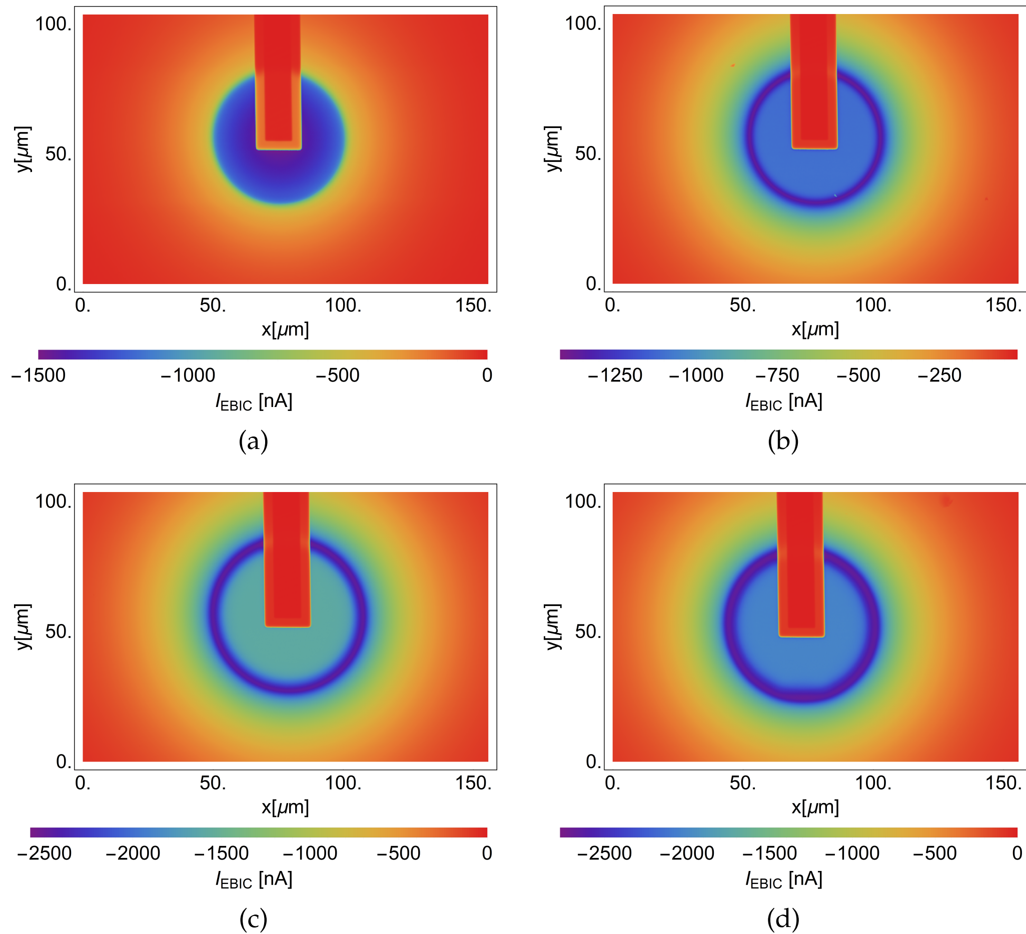

FIGURE 9.16: 2D EBIC signal of different n-well types in passivated design. Measurement was done with a beam energy of 20 keV and a beam current of 0.8 nA. (a) n+ (b) NW (c) DN and (d) DN2

hole pairs at the depth of the junction. Series of measurements with electron beam energies of 10 keV, 20 keV and 30 keV for *n*+-well (Figure 9.18), NW (Figure 9.19) and DN2 (Figure 9.20) are shown respectively. In Figure 9.21 the extracted line scans for the different *n*-wells for different beam energies are shown.

In Figure 9.21 the extracted linescans for the different structures and electron beam energies are shown.

Plotting the EBIC signal in the *n*-well region for different electron beam energies, shows how the EBIC signal is, depending on the junction depth, increasing with increasing electron beam energy. One would assume a maximum of EBIC signal, when the main generation takes place in the junction region, followed by a decrease of the EBIC signal with increasing generation depth. In Figure 9.22 the EBIC signal in dependence on the electron beam energy in the *n*-region is shown for all investigated *n*-wells. The expected increase with electron beam energy is observed, but not a peak value followed by a decay, even though, at least for the *n*+ and the NW structure the generation with 30 keV should be deeper than the position of the space charge region. This asymmetry in the behavior can be explained by the low doping of the substrate in comparison to the *n*-well. Carriers generated just several μm underneath the junction will still diffuse to the junction.

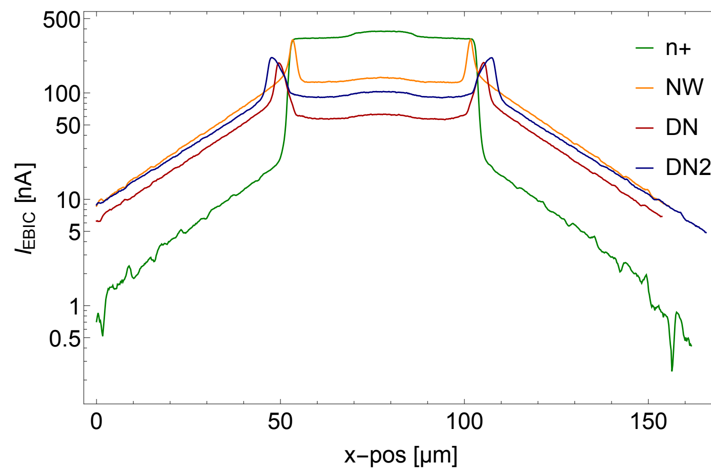

(a)

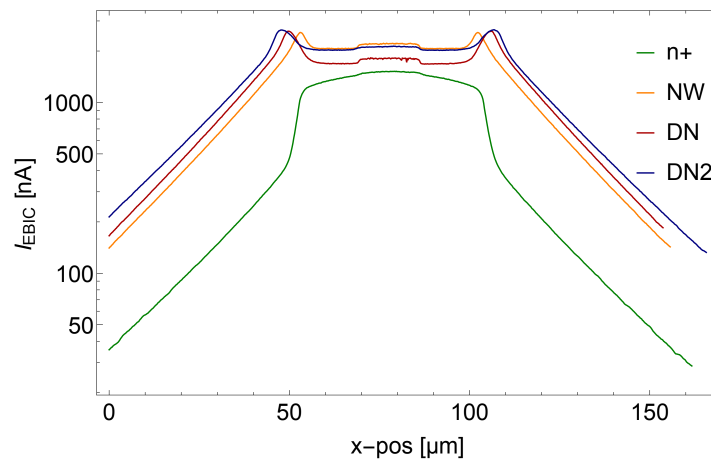

(b)

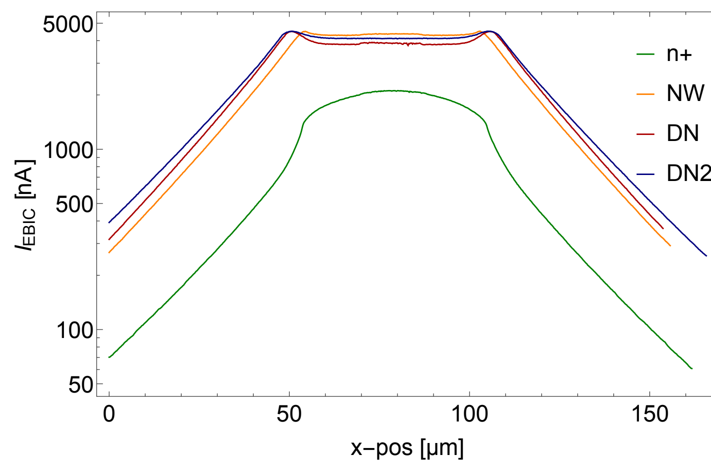

(c)

FIGURE 9.17: 1D EBIC signal of different n-well types in passivated design. Measurement was done with a beam current of 0.8 nA. Electron beam energy was(a) 10 keV (b) 20 keV and (c) 30 keV

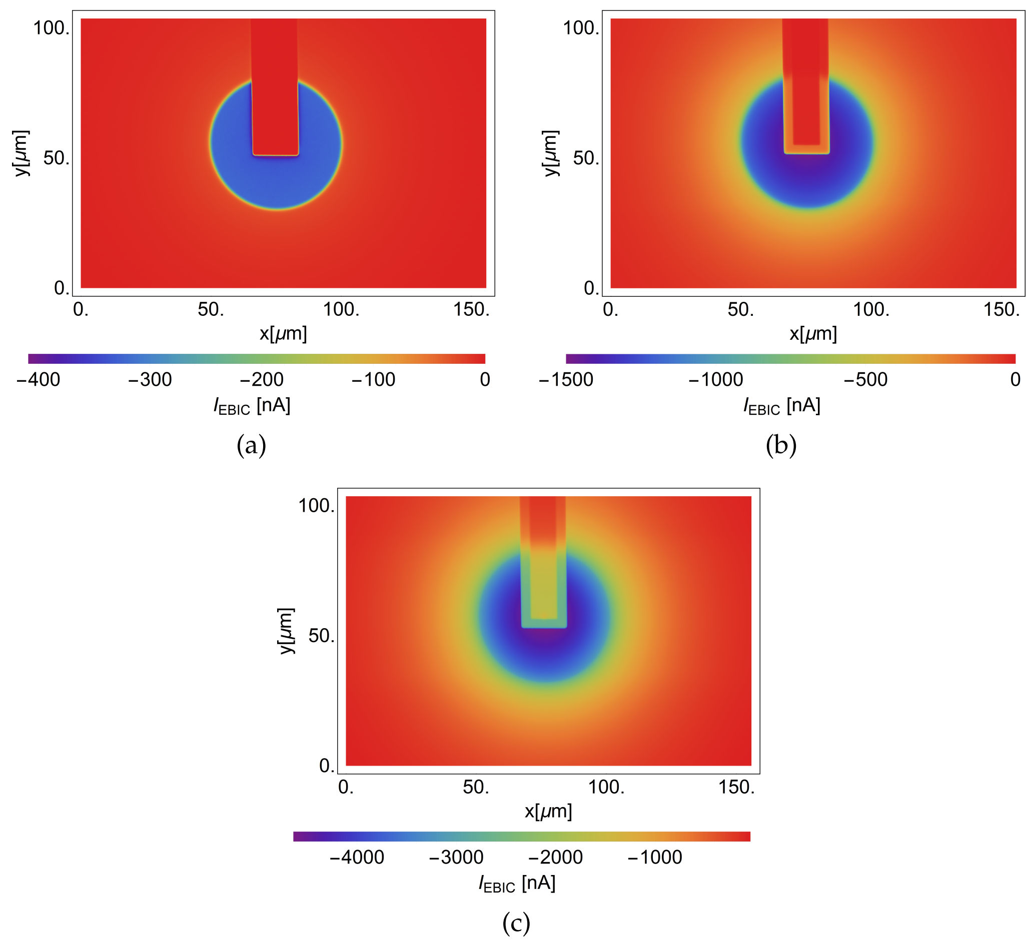

FIGURE 9.18: 2D EBIC signal of n+-well in passivated design for different electron beam energies. A beam current of 0.8 nA was used. (a)10 keV (b) 20 keV and (c) 30 keV electron beam energy

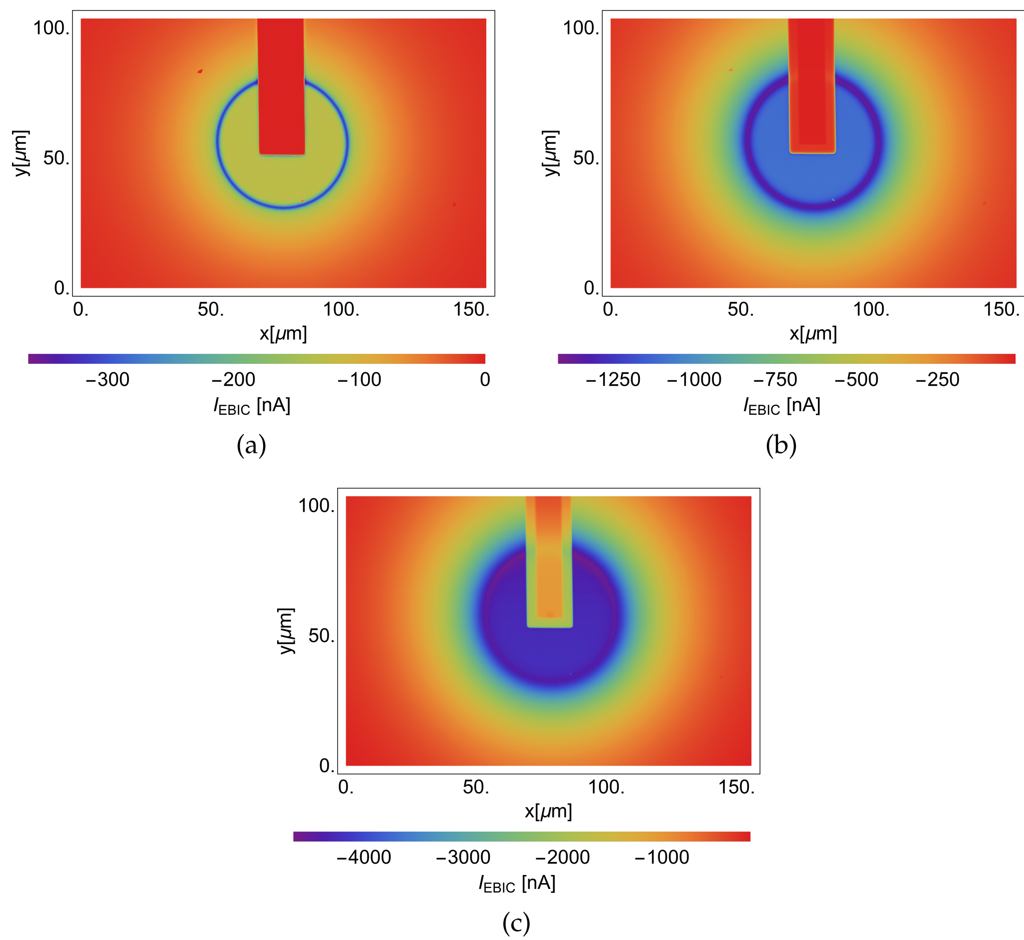

FIGURE 9.19: 2D EBIC signal of NW in passivated design for different electron beam energies. A beam current of 0.8 nA was used. (a) 10 keV (b) 20 keV and (c) 30 keV electron beam energy

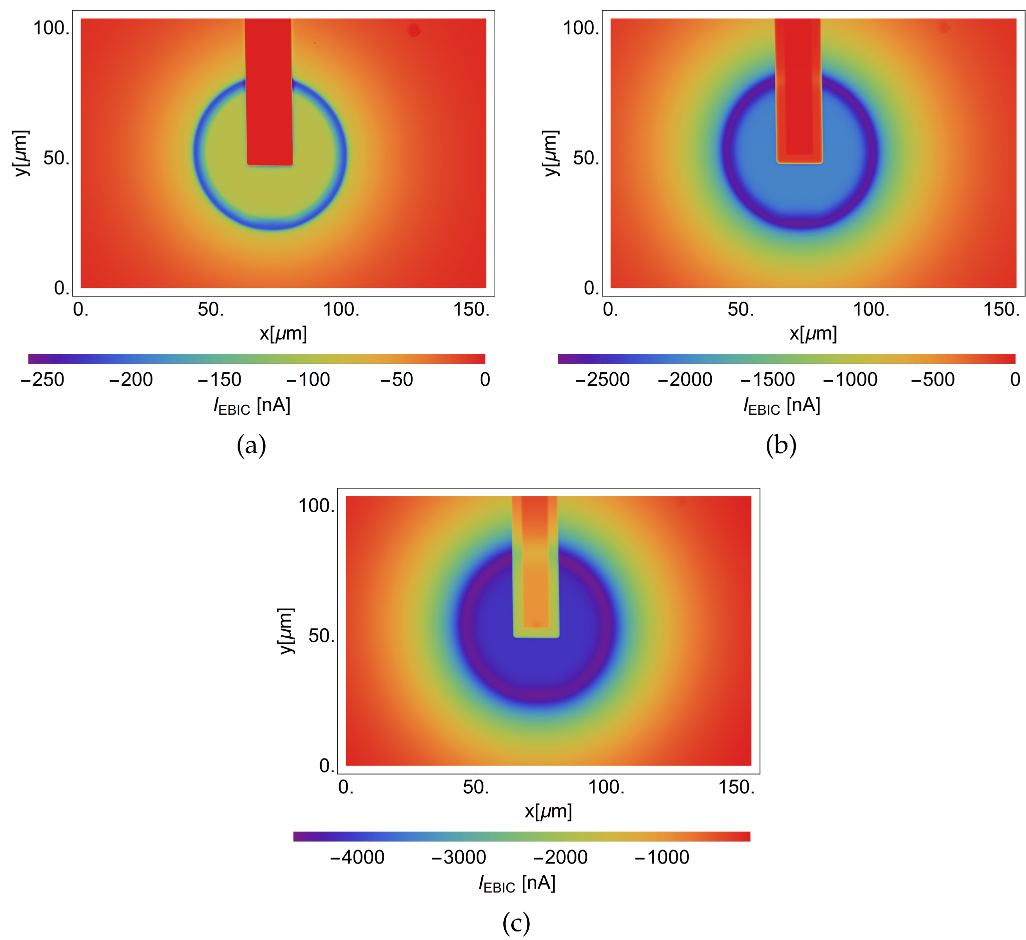

FIGURE 9.20: 2D EBIC signal of DN2 in passivated design for different electron beam energies. A beam current of 0.8 nA was used. (a) 10 keV (b) 20 keV and (c) 30 keV electron beam energy

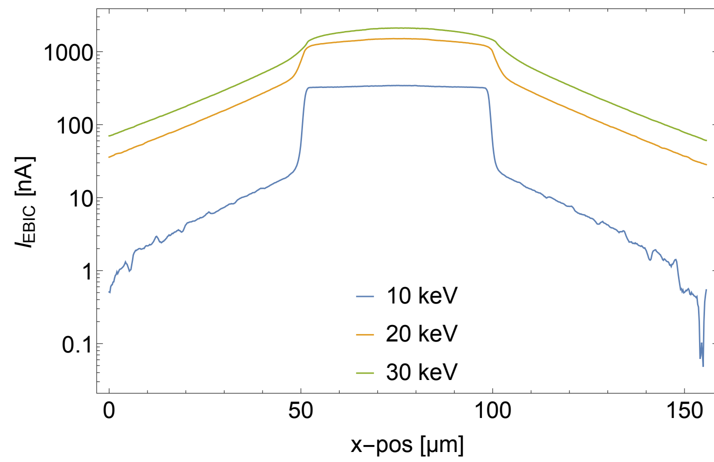

(a)

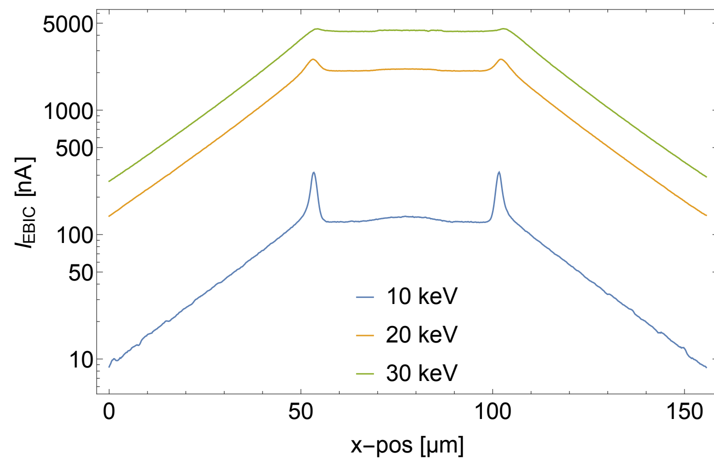

(b)

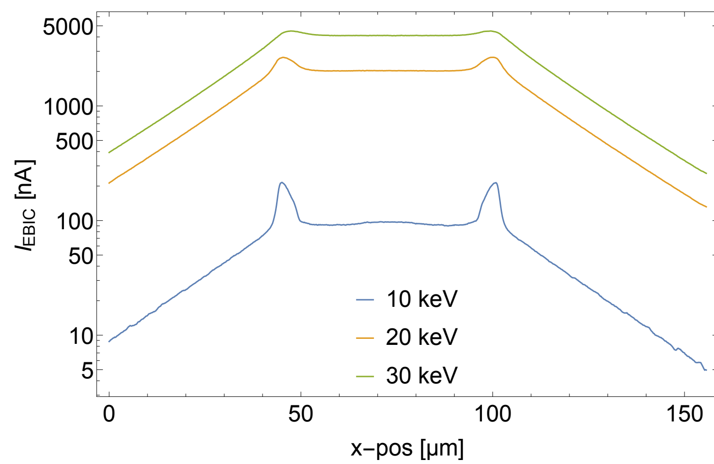

(c)

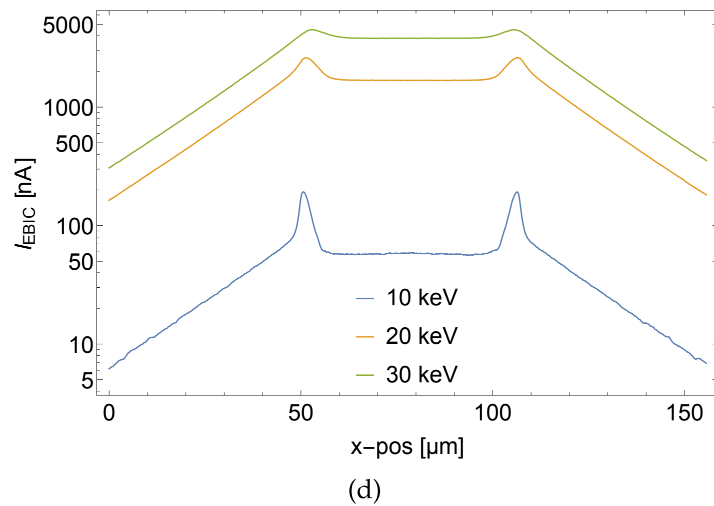

(d)

FIGURE 9.21: 1D EBIC signal of different n-well types in passivated design. Measurement was done using a beam current of 0.8 nA and electron beam energies of 10 keV, 20 keV and 30 keV. (a) n+ (b) NW (c) DN and (d) DN2

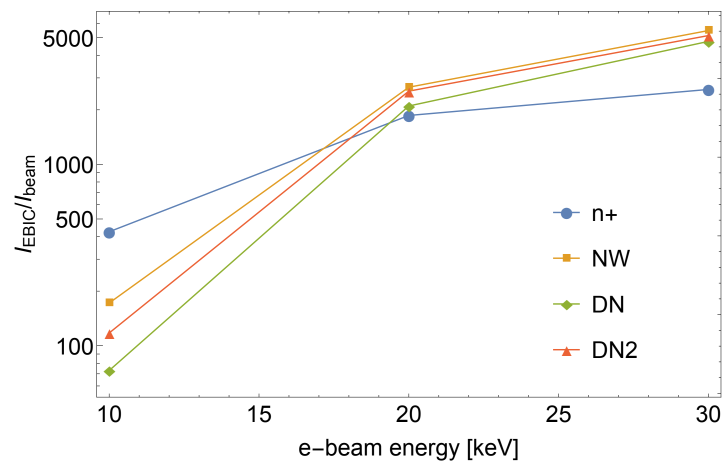

FIGURE 9.22: The EBIC signal normalized by the electron beam current (0.8 nA) for 10, 20 and 30 keV for different *n*-well types.

9.6 Influence of electric field across structure

In the investigations shown so far, the carrier transport was driven by two mechanisms. The minority carrier diffusion in the field free region and drift inside the space charge region due to the electric field. In this section the influence of an applied external electric field on the minority carrier transport behavior was investigated. By applying an external electric field across the structure, the minority carriers feel an additional force and a drift component is added to the diffusion. The electric field was generated by contacting the p-substrate on either side of the *n*-well and applying a negative voltage on one side to generate a potential difference. The strength of the electric field is tuned by the voltage applied. The comparison of the measurements with

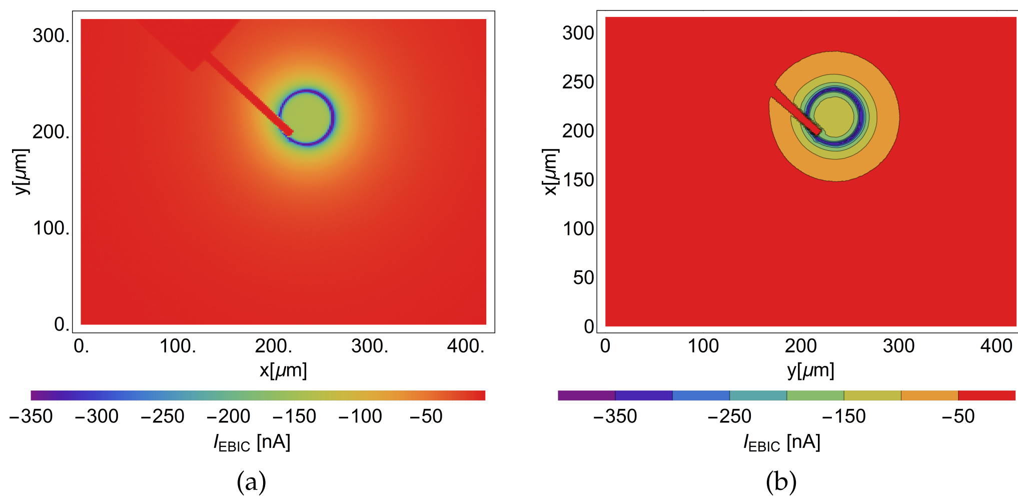

FIGURE 9.23: 2D EBIC signal of a passivated DN structure. No voltage was applied on the contacts.(a) Coloured EBIC plot and (b) contour plot.

varying electric field is done using contour plots as shown in Figure 9.23b, because the differences are better illustrated than in the standard plots. Measurements were done with an applied negative bias on the right as well as on the left side of the structure. The applied bias ranged from 0 V to -20 V.

In Figure 9.24 and Figure 9.25 one can see that by applying an electric field an additional component is added to the diffusion process. The signal looses its symmetric shape and a comet like signal is measured. The tail corresponds to the direction and the strength of the applied electric field. The stronger the electric field the more pronounced the tail gets. By reversing the applied voltage also the tail is reversed.

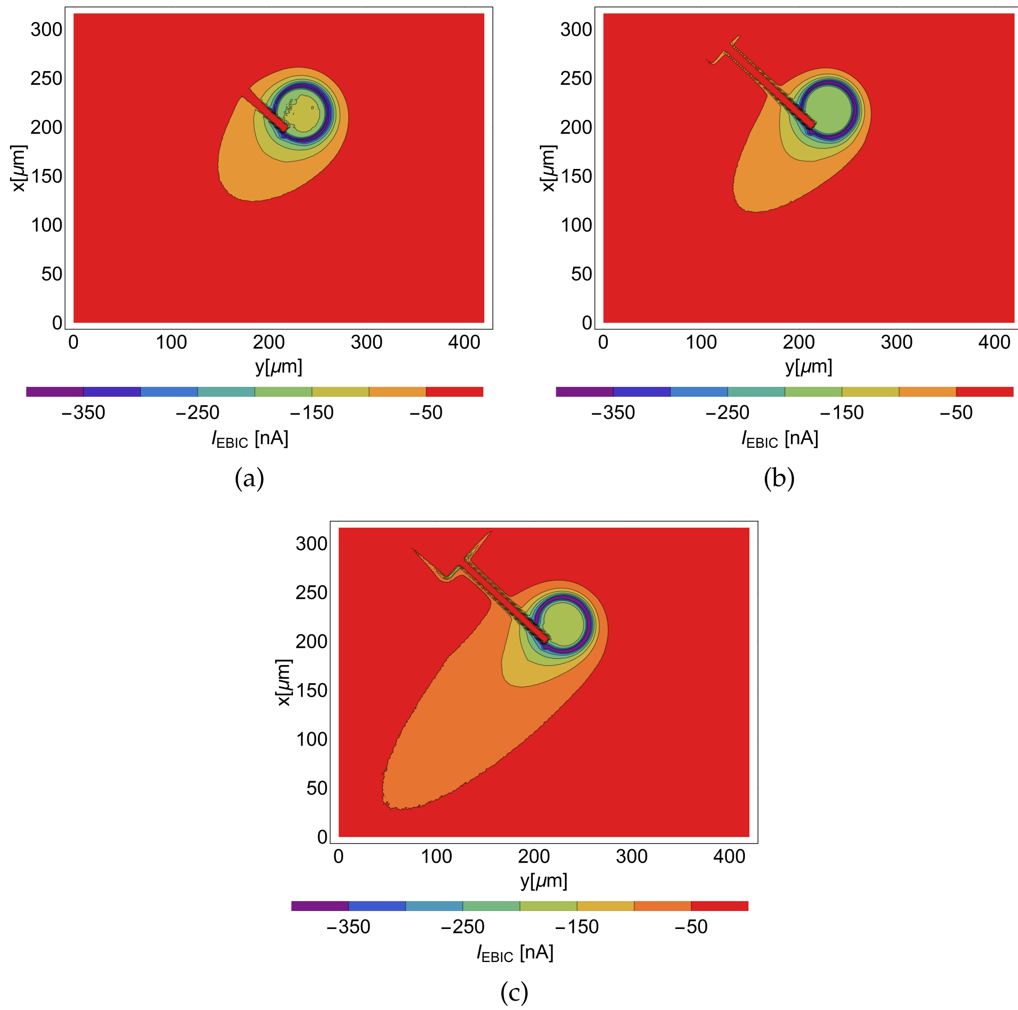

FIGURE 9.24: 2D contour plot of the EBIC signal of passivated DN with different voltage applied to the left contact. (a) -5 V (b) -10 V and (c) -15 V

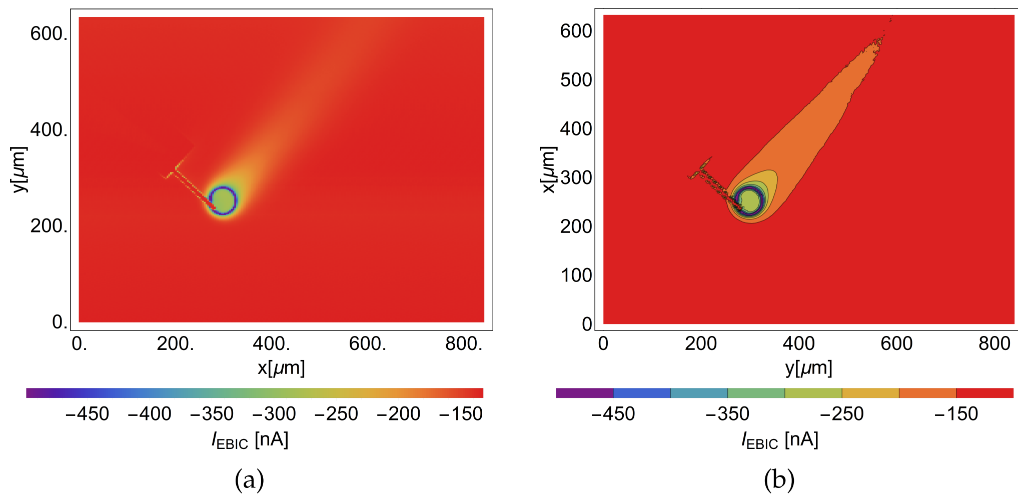

FIGURE 9.25: 2D EBIC signal of a passivated DN structure. On the right contact -20 V are applied.(a) Coloured EBIC plot and (b) contour plot.

9.7 EBIC on cross-sections

Until now only top-view measurements have been discussed. The advantage of top-view measurements is that it is a non destructive method. The only challenge is to surpass the issue with the BEOL stack, explained before. To get information about the vertical structure cross-section measurements have to be done like those described in Chapter 8. In the following two different ways of producing cross-sections are introduced and the resulting EBIC measurements are shown.

9.7.1 Cleaved sample

First the sample is simply cleaved as was done for the EPI diodes. Care was taken to cleave the sample along the center of the diode structures. Like this the vertical extension of the space charge region is visible but the contacts are preserved. The disadvantage of this procedure is that only structures located in a row can be investigated on one sample as the part has to be big enough for the cleaving procedure. Cleaved samples can't be cleaved any further. Furthermore, the contacts have to be placed in the right way making it possible to preserve the contacts but still showing the region of interest. This might not be possible in more complex structures. In Figure 9.26 the SEM image of the cross-section is shown in (a) and the corresponding EBIC signal in (b). One can see a very high almost constant EBIC signal over the whole wafer region with a signal maximum at the position of the n-well. This signal can be explained by the high quality of the surface and the long lifetime in the substrate.

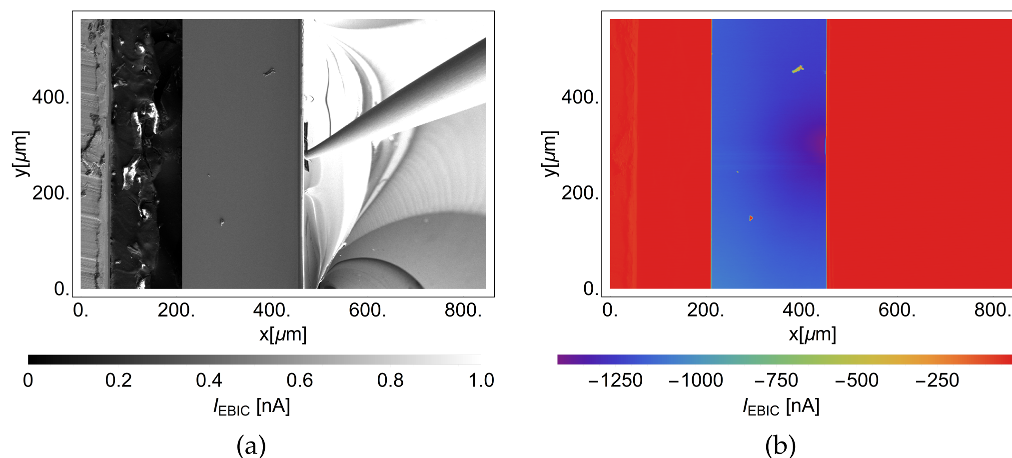

FIGURE 9.26: EBIC measurement of a cross-secton on a cleaved sample. In (a) the SEM image is shown and in (b) the 2D EBIC sgignal. Electron beam energy was 10 keV and electron beam current 0.8 nA.

When scanning longer over the sample with the electron beam, a degradation of the signal was observed. The longer one investigates the sample the smaller becomes the region with high signal until only the area at the junction produces a significant EBIC signal. This effect was already discussed in Chapter 8. In Figure 9.27 this evolution is shown.

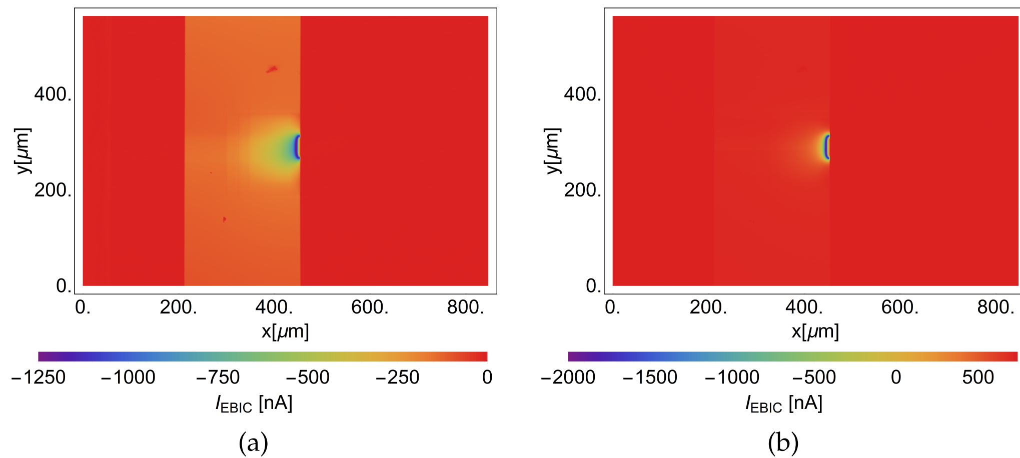

FIGURE 9.27: EBIC measurement of a cross-secton on a cleaved sample. The Evolution of the EBIC signal with time is shown. Electron beam energy was 10 keV and electron beam current 0.8 nA.

In this measurement the sensitivity of the cleaved surface to the the electron beam becomes very obvious. It seems that with high electron beam currents, the surface of the sample is changed. In the electron beam energy range used in a SEM, the introduction of lattice defects are very unlikely as stated in [44] and [45]. More likely is a contamination of the surface with carbon by electron stimulated adsorption [44], [45]. The contamination process is linear depending on the beam current fitting to the investigations of the measurement. When the interest lies in the investigation of p-n junctions and well configurations this effect is very welcome but for the investigation of carrier transport this is of course an unwanted effect. In Figure 9.28 the shape of the DN-well in vertical direction is compared for the unpassivated case in Figure 9.28a and the passivated in Figure 9.28b. As in the passivated case the lateral diffusion is restricted by the highly doped p-well at the surface region it seems that the vertical diffusion is more pronounced than in the unpassivated case where the lateral diffusion is bigger than in the passivated.

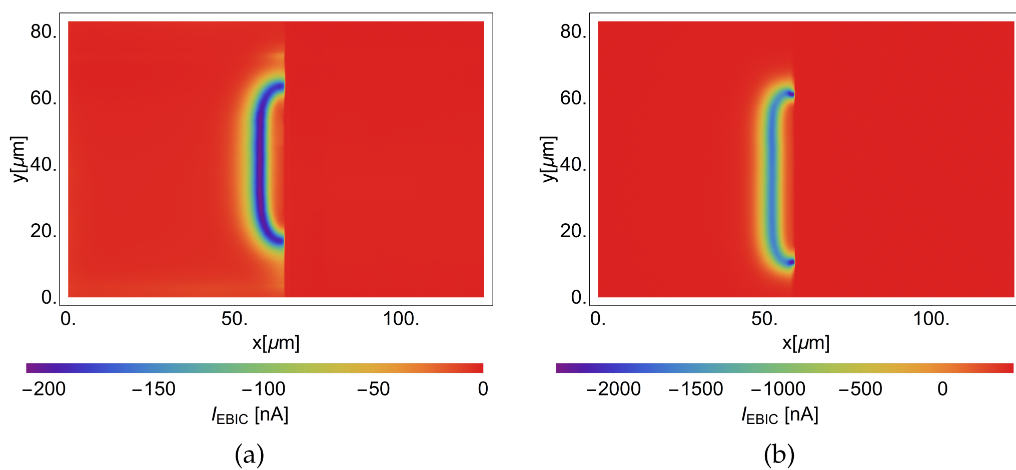

FIGURE 9.28: EBIC measurement of a cross-secton on a cleaved sample. Comparison between unpassivated DN (a) and passivated DN (b). Electron beam energy was 5 keV and electron beam current 0.8 nA.

9.7.2 FIB cross-section

A more advanced but also more time and resource consuming approach is to create cross-sections using a focused ion beam (FIB). Using this technique local cross-sections can be generated at the position of interest while not harming the rest of the device. In a FIB, energetic ions are accelerated onto the sample. The most important physical interactions between ions and substrate are sputtering of sample atoms, electron emission, displacement of atoms in the solid and the emission of phonons. Chemical bonds are broken due to chemical interactions. Here we will only focus on the sputtering of material as this effect is used to create cross-sections. Using a high ion beam current, removal of material is achieved. When scanning over the sample physical sputtering is achieved in the region of interest. The sputter process is dependent on material, ion beam current and energy and angle of incidence of the beam. To create a FIB cross-section, first material next to the region of interest is removed using a quite fast milling. Like this a steep side wall near the region under investigation is created. In a second step this sidewall is made perfectly vertical and polished by milling steps using lower ion beam currents and smaller milling steps. By tilting the sample the face of the created FIB cross-section can be investigated. The SEM image of a FIB cross-section is shown in Figure 9.29a and in Figure 9.29b the corresponding EBIC image is shown. The sample was tilted to 45°. The maximum possible tilt angle is dependent on the window opened in the first milling step. More detailed information about FIB and its application can be found in [73]. Because of the implantation and sputtering when creating the cross-section with the ion beam the surface quality is not very high [74]. This can be seen in the results of the EBIC measurements shown in Figure 9.30. Here an ion beam energy of 30 keV and a beam current of 21 nA was used to sputter away material to a depth of 25 μm. Subsequently, a sputtering step with a lower ion current of 9 nA was used for polishing the surface. This resulted in an amorphous surface layer of about 30 nm thickness and a high surface recombination rate [73],[75]. The 2D EBIC measurement of a cross-section is shown for a passivated NW- (Figure 9.30a) and a passivated DN-structure (Figure 9.30b).

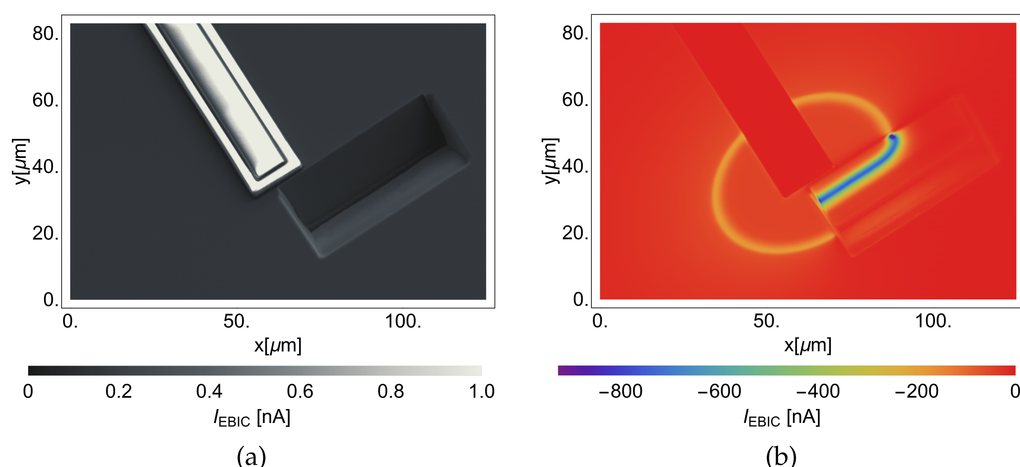

FIGURE 9.29: EBIC measurement on a FIB cross-section. (a) SEM image and (b) corresponding EBIC image. The sample was tilted 45°. [61]

The junction position is very well visible and the decay after the junction is very fast

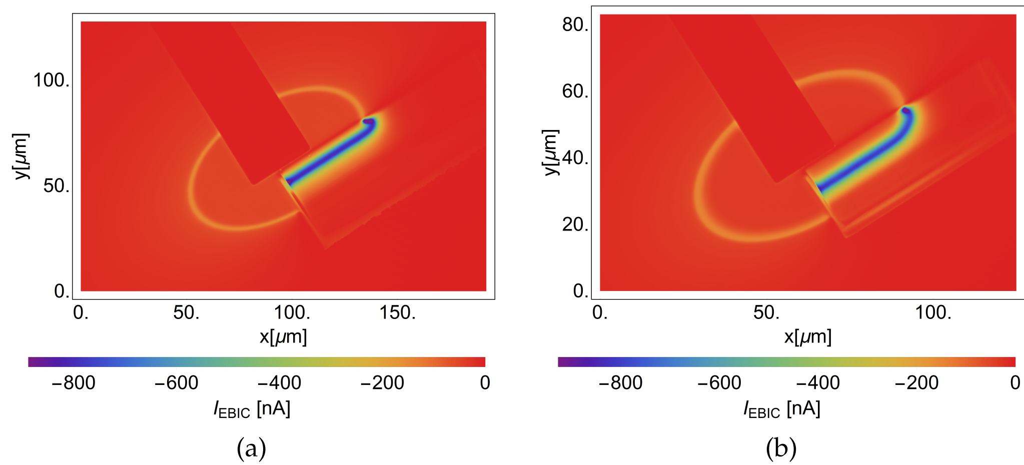

FIGURE 9.30: 2D EBIC signal of FIB x-sections. (a)Passivated NW and (b) Passivated DN. The electron beam energy was 10 keV, the beam current 0.8 nA and the sample was tilted 55° in both cases.

due to the high surface recombination rate. In this application the high surface recombination rate is not a drawback as it allows us to investigate the positions and shapes of the junctions. A good surface quality would lead to a long diffusion length and a high signal would be detected over the whole cross-section area. Comparing Figure 9.30a and Figure 9.30b, the difference between the two wells is very well represented. One can see the difference in depth very clearly. Furthermore the shape at the corner of the well looks different. This difference can be explained by referring to the layout of the structures. In the case of the NW-structure the p-well layer acting as passivation is drawn directly next to the n-layer. In the DN-structure, on the other hand, a distance between the to layers is implemented because of the stronger out-diffusion in lateral direction coming from longer diffusion times. Looking at the well shapes one can conclude that also for the NW-structure a distance would be necessary in order not to disturb the diffusion process by the highly doped p-layer. In Figure 9.31 is the 2D EBIC signal of a n+-well structure shown as overview (Figure 9.31a) and in detail (Figure 9.31b). It can be clearly seen how shallow this well is and that there is no diffusion step leading to a lateral or vertical diffusion of the well.

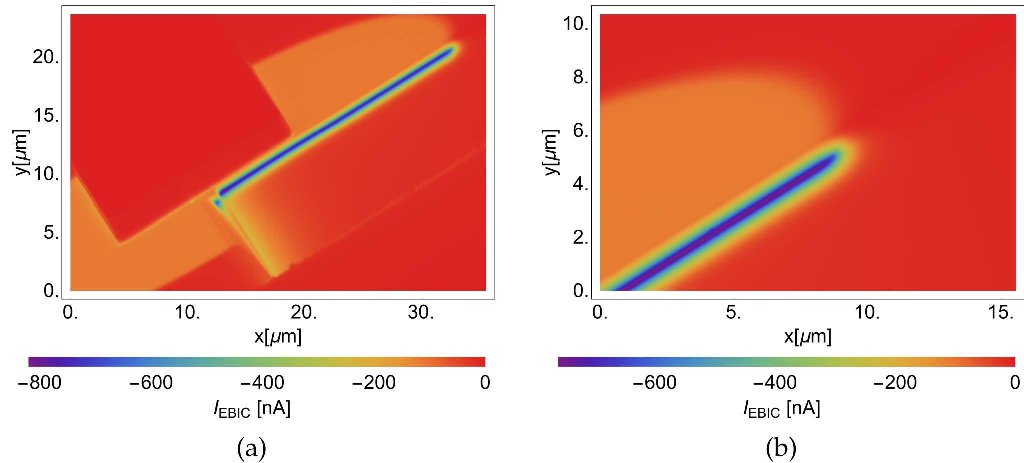

FIGURE 9.31: 2D EBIC signal of FIB x-sections.(a) Passivated $n+$ well and (b) zoomed in passivated $n+$ well. The electron beam energy was 10 keV, the beam current 0.8 nA and the sample was tilted 75° in both cases.

9.8 EBIC TCAD simulation

Using the previously calibrated EBIC TCAD environment also the more complex structure of the test chip was simulated. Because of the complexity of the structure and wells used in the design it was necessary to use process simulation in combination with Sentaurus SDE [54] in order to generate the structure. To save simulation time only a quarter of the structure was generated which is a valid assumption because of the symmetry of the diode.

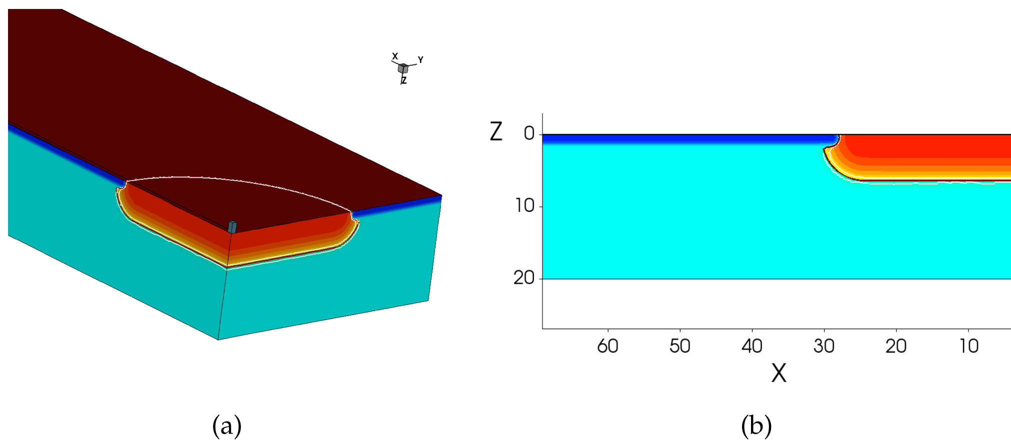

FIGURE 9.32: Structure generated with Sentaurus SProcess and Sentaurus SDE showing the doping profile. Blue tones are p-type and red/yellow tones are n-type doping (dark colors high doping concentration, light colors low doping concentration) (a) 3D and (b) 2D.

In Figure 9.32a the 3D structure including the doping profile of a passivated structure with DN-well in a standard non-EPI substrate, is shown and for a more detailed look the 2D cross-section through the structure in Figure 9.32b. In Figure 9.33 the electric field across the structure is shown. There is a strong electric field at the p-n junction

and also at the *p*-*p*+ junction coming from the surface passivation.

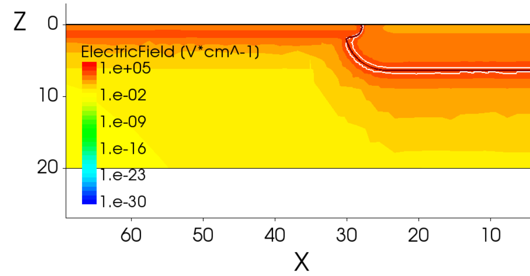

FIGURE 9.33: Structure generated by Sentaurus SProcess and Sentaurus SDE showing the electric field distribution in a 2D cut.

Across this structure a EBIC line scan was simulated in order to compare with the measurement results. The simulation was done for two surface recombination rates of 10^3 cm/s and 10^6 cm/s. The linescans are shown in Figure 9.34.

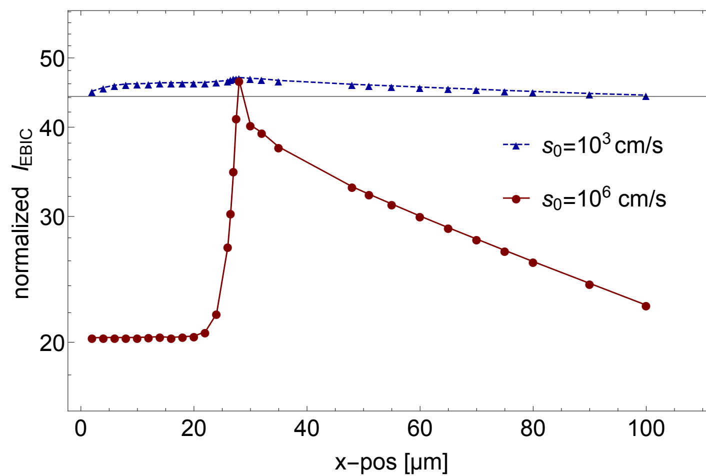

FIGURE 9.34: Simulated EBIC linescans of a DN n-well design with passivation for a surface recombination rate of 10^3 cm/s and 10^6 cm/s. Electron beam energy was 20 keV.

Surprisingly, a strong influence of surface recombination rate can be seen. This was not the case in the measurements, where almost no influence was observed. Additionally, the extracted diffusion lengths, of 125 µm and 1250 µm, are much longer than evaluated by measurement. To meet the experiment better, the lifetime in the implanted *p*-well is decreased in comparison to the substrate. This is reasonable, as the lifetime is influenced by the implantation process. The simulation results are shown in Figure 9.35. The influence of the surface recombination velocity is almost eliminated. Due to the decreased lifetime, carriers generated in the *p*-well are more likely to recombine and their contribution to the EBIC signal is decreased. The extracted diffusion lengths of 100 µm are still longer than extracted from measurement.

Even though the simulation needs further work to reproduce the measurement, the shape of the measurement is reproduced.

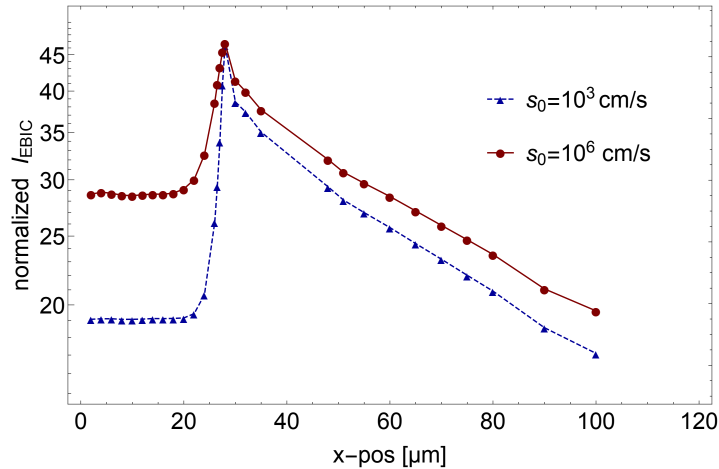

FIGURE 9.35: Simulated EBIC linescans of a DN n-well design with passivation for a surface recombination rate of 10^3 cm/s and 10^6 cm/s. Electron beam energy was 20 keV and the lifetime in the *p*-well passivation is decreased relative to the substrate lifetime.

9.9 Rectangular diodes

In most standard applications the photodiode shape is not round but rectangular. This shapes introduces corner effects. In order to prevent premature breakdown because of a high electric field at the corners, designs with round or beveled corners are used. Three diode variations were processed on the testchip to investigate the effect of corner shape. The SEM image and corresponding EBIC image of an overview of the diode with 90° edges are shown in Figure 9.36. The contact of the *p*-substrate surrounds the *n*-well as can be seen in Figure 9.36a.

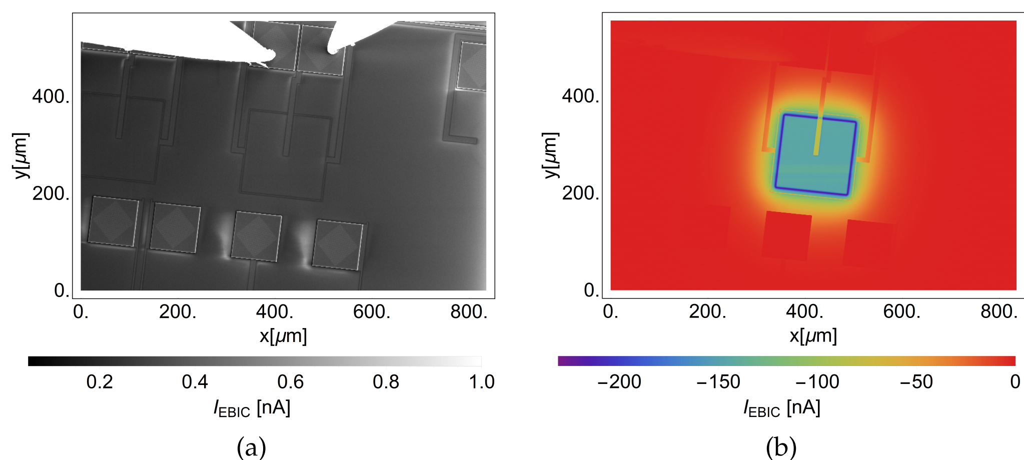

FIGURE 9.36: (a) SEM image of rectangular *n*-well in *p*-substrate diode and (b) corresponding EBIC image.

In Figure 9.37 the three different design variations according to corner shape are shown and compared. The shape is very nicely visible in the EBIC signal. The line with low signal around the diode is the metalization of the substrate contact.

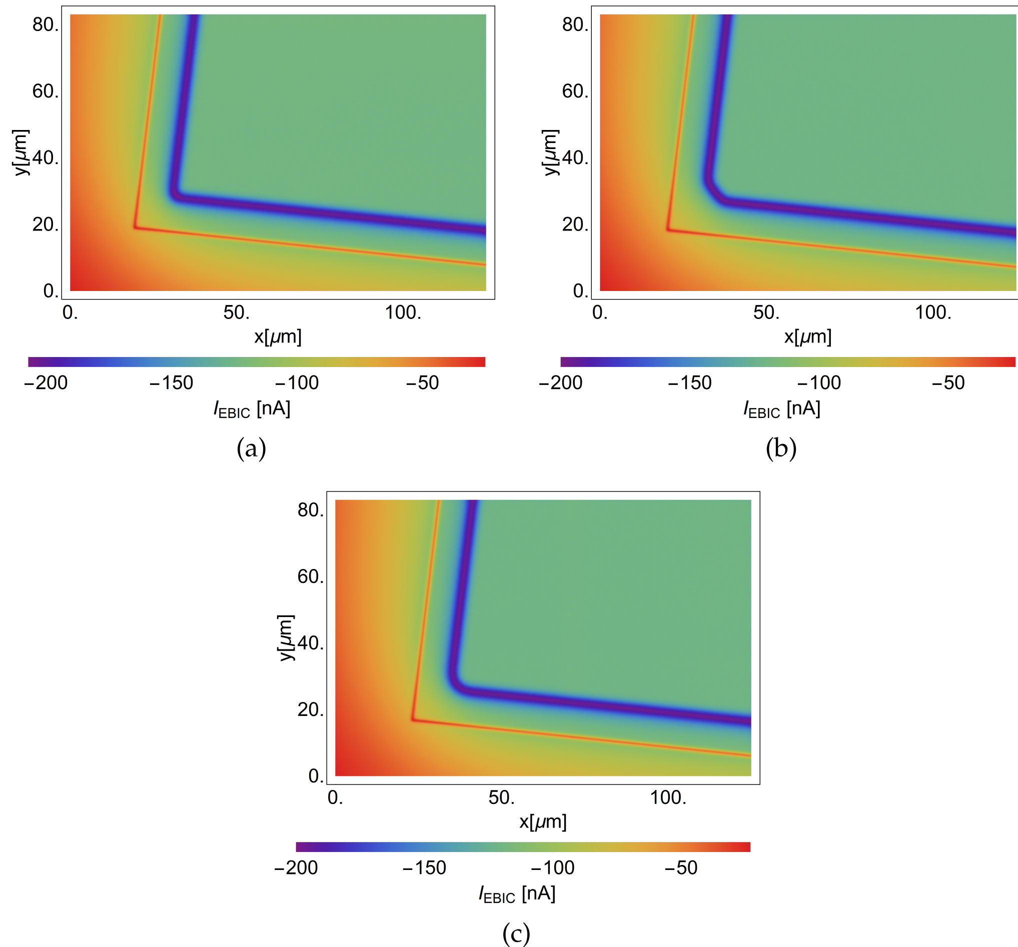

FIGURE 9.37: 2D EBIC signals showing different corner shapes of standard rectengular diodes. (a) 90° corner, (b) beveled corner with 45° and (c) round corner.

9.10 Conclusion on EBIC testchip

In this chapter a dedicated EBIC testchip was introduced and its characterization was presented. It was shown that even though top-view investigations have a lot of advantages, the BEOL stack introduces a challenge in sample preparation. Again, as already in the investigations of the EPI diodes, the surface preparation, in this case the removal of the BEOL oxide is crucial to the EBIC results. The best procedures were found to be either using only a two metal process, where the reduced amount of metal also reduces the oxide thickness. With more complex structures this is not always possible. The second approach, which results in a reproducible process, is the use of a mask etch in the production line. Performing a plasma etch step it is important to leave some residual oxide, in order not to harm the silicon surface. It was shown that an effective diffusion length can be extracted out of the EBIC measurement. The measured value includes the influence of the surface condition like surface recombination rate and surface charge and the substrate type, e.g. EPI thickness. It was shown that using a surface passivation layer, e.g. a layer with high doping at the surface, eliminates influence of the surface quality. Additionally, to the investigation of substrate type and doping, the influence of different *n*-well types were examined. Top-view measurements with different electron beam energies give an indication of the depth of the well. A

even better idea of the the depth and the shape of the well can be achieved doing measurements on cross-sections produced by cleaving or FIB. Furthermore, this is a good example that not in every investigation a low surface recombination rate is preferable. When the shape and the position of a junction is of major interest, a higher surface recombination is an advantage as it illustrates the location sharply. Furthermore, the influence of an applied electric field across the structure was shown. The shape of the EBIC signal is a result of the combination of a diffusion current and a drift current dependent on the applied field strength. At the end again simulation results of an exemplary test chip structure were shown. Even though the general shape of the simulated line scan is in accordance with the measurement, the extracted diffusion lengths are too long in comparison to the measured results. Additionally, a strong surface dependence was observed, even though, a passivated structure was simulated. Further work has to be done to improve the simulation and to fit it to the measurement.

Chapter 10

Conclusion

In this work, the transport behavior of minority carriers in silicon devices was investigated. The main goal was to extract carrier transport parameters on the device level. As an investigation method, EBIC was chosen as it gives spatial information about the carrier transport. After first test measurements of already known structures, special structures dedicated for this work were investigated.

In the first part of the work, rather simple, step junction structures, were produced using EPI deposition. The goal of the investigation of these structures was to get to know the measurement system and procedure and to set-up the TCAD simulation environment. Different device parameters such as doping concentration of the n- and p-type EPI and surface quality were investigated. Furthermore, the influence of measurement parameters, including the electron beam energy and reverse biasing of the diode was examined. The measurements performed experimentally were reproduced by TCAD simulation with very good agreement. Parameters such as surface charge and bulk minority carrier lifetime are hard to investigate experimentally. After calibration of the simulation environment, these parameters and their influence on the EBIC signal were investigated using the TCAD simulation. One of the main results of this chapter is the strong dependence of the surface quality on the EBIC signal. It was shown that in the case of a high surface recombination velocity it is not straight forward to extract the bulk diffusion length out of the measurement as a measured value will always be a combination of surface recombination rate and bulk recombination lifetime. A measurement method that provides information about the surface quality by doing measurements at different electron beam energies was introduced. Furthermore, it was shown, that out of the combination of measurement and simulation, the surface recombination rate can be determined. Another outcome was, that for extracting bulk diffusion lengths out of position dependent EBIC measurements, bigger structures, at least in the order of the diffusion length, with a high surface quality are necessary in the case of high quality material such as that used in the microelectronics industry.

With the knowledge gained in the first part, in the second part, a test chip was designed and produced using a 0.35 µm high voltage (0.35 HV) CMOS process. The size was chosen accordingly to extract diffusion lengths from position dependent EBIC scans. Additionally to the investigation of different starting materials, also different n-well types, available in the 0.35 HV process were processed. Measurements were done, depending on beam energy, beam current and sample preparation. It was shown that the best way to do top-view measurements on a fully processed device including a BEOL stack is using a dedicated mask to etch the BEOL stack in the area of interest. Care has to be taken that the etching is not done all the way to the silicon, but is stopped several 100 nm before in the oxide. In this way, the surface is not harmed by the plasma etching and the residual oxide is thin enough to produce a high EBIC signal. Two

different designs were introduced to investigate the concept of surface passivation. For this, a highly *p*-doped surface layer was introduced around the implanted *n*-well. It was shown that measurements done on the design without surface passivation are very sensitive to surface treatment and the electron beam, while measurements done on passivated structures were very stable. Diffusion lengths were extracted, using the passivated design for different substrate types. Furthermore, different *n*-well structures were compared and measured with different electron beam energies. Information about the well depth can be gained out of these measurements. Even more information about the depth and shape of a well can be achieved by measurements on cross-sections. Two methods have been introduced: cleaving the sample and performing a FIB cross-section. It was shown, that when the major interest is to visualize *p*-*n* junctions, a high surface recombination rate is preferable, while for determining diffusion lengths in substrates a low surface recombination is necessary.

The power of the combination of a TCAD model and experimental measurements was shown. While any experimentally measurable quantity can be used to compare to simulations, EBIC is particularly interesting because it produces two-dimensional maps of fully processed devices. Only if parameters such as the mobility, the minority carrier lifetimes, and the surface recombination rates are known in all regions and on all surfaces in the device and are implemented to the simulation, will the EBIC simulation and experiment match in all details.

Even though a lot of information about surface effects and their influence on the EBIC signal and thus on the recombination processes in a device could be gained within this work, there are still a lot of open points which have to be further investigated. Especially, a better understanding of the electron-matter interactions and the influence of the measurement method on recombination at the surface is necessary. To sum up one can say, that EBIC cross-sections, with a high surface recombination rate, can be used to investigate doping profiles. This can be used as a process control tool, to evaluate diffusion well processes.

To determine bulk and interface recombination rates, cross section structures are not advisable. It was shown that the surface generated by cleaving is hard to control and strongly influences the evaluated parameters. The more superior approach, is to do top-view measurements, like shown on the example of the test-chip structures. But also in this case, an altering of the sample due to the measurement procedure was observed in some structures. Possible explanations for the altering effects are charge injection into the silicon-dioxide or depassivation of silicon dangling bonds at the interface because of the electron beam. To prove this theory, an interesting experiment would be, to verify the altering effect by measuring standard characteristics, like the threshold voltage or the mobility of a MOSFET, before and after electron beam bombardment of the device. To overcome the issue of surface altering due to electron beam bombardment, OBIC would be a very interesting complementary measurement method because of the differences in light-silicon interaction and electron-silicon interaction. The excitation depth of electron-hole pairs can be tuned by the use of different wavelengths following the absorption law of light. While an electron beam, still generates a big portion of carriers close to the surface, even when using high beam energies, in the case of visible light, the generation of electron hole pairs can be limited to bulk regions by choosing the wavelength accordingly. Another interesting approach, to gain additional knowledge, would be to perform transient measurements, using a chopped electron beam.

Doping gradients could be a useful way to tune surface and interface recombination rates. The surface recombination rate can be reduced dramatically by heavier doping

near the interface. The gradient in the doping repels the minority carriers from the interface. Samples with a heavy doping at the surface were not altered by an EBIC measurement probably because the minority carriers were kept away from the areas damaged by the electron beam.

Bibliography

[1] D. K. Schroder, “Carrier lifetimes in silicon”, *IEEE Transactions on Electron Devices*, vol. 44, pp. 160–170, 1997.

[2] R. Bernin, A. Cutolo, A. Irace, P. Spirito, and L. Zeni, “Contactless characterization of the recombination process in silicon wafers; separatioin between bulk and surface contribution”, *Solid-State Electronics*, vol. 39, no. 8, pp. 1165–1172, 1996.

[3] D. K. Schroder, “Effective lifetimes in high quality silicon devices”, *Solid-State Electronics*, vol. 27, pp. 247–251, 1984.

[4] N. V. Loukianova, H. O. Folkerts, J. P. V. Maas, D. Verbugt, A. J. Mierop, W. Hoekstra, E. Roks, and A. J. P. Theuwissen, “Leakage current modeling of test structures for characterization of dark current in CMOS image sensors”, *IEEE Transactions on Electron Devices*, vol. 50, no. 1, 2003.

[5] J. Bogaerts, B. Dierickx, and R. Mertens, “Enhanced dark current generation in proton-irradiated CMOS active pixel sensors”, *IEEE Transactions on Nuclear Science*, vol. 49, no. 3, 2002.

[6] J. Schmidt, “Measurement of differential and actual recombinatin paramerts of crystalline silicon wafers”, *IEEE Transactions on Electron Devices*, vol. 46, no. 10, 1999.

[7] R. Ahrenkiel, N. Call, S. Johnston, and W. Metzger, “Comparison of techniques for measuring carrier lifetime in thin-film and multicrystallien photovoltaic materials”, *Solar Energy Materials and Solar Cells*, vol. 94, pp. 2197–2204, Aug. 2010.

[8] L. Chernyak, A. Osinsky, and A. Schulte, “Minority carrier transport in GaN and related materials”, *Solid-State Electronics*, vol. 45, pp. 1687–1702, 2001.

[9] Z. Z. Bandic, P. M. Bridger, E. C. Piquette, and T. C. M. Gill, “The values of minority carrier diffusion lengths and lifetimes in GaN and their implications for bipolar devices”, *Solid-State Electronics*, vol. 44, pp. 221–228, 2000.

[10] M. Miyashia, T. Tusga, K. Makihara, and T. Ohmi, “Dependence of surface microroughness of cz, fz, and epi wafers on wet chemical processing”, *Journal Electrochemical Society*, vol. 139, no. 8, 1992.

[11] J. Y. Cheng, D. J. Eaglesham, D. C. Jacobson, P. A. Stolk, and J. L. Benton, “Formation of extended defects in silicon by high energy implantation of B and P”, *Journal of Applied Physics*, vol. 80, no. 4, 1996.

[12] M. Watanabe, G. Actor, and H. C. Gatos, “Determination of minority-carrier lifetime and surface recombination velocity with high spacial resolution”, *IEEE Transactions on electron devices*, vol. 24, 1977.

[13] C. Donolato, “Theory of beam induced current characterization of grain boundaries in polycrystalline solar cells”, *Journal of Applied Physics*, vol. 54, 1983.

[14] S.-Q. Zhu, E. I. Rau, and F.-H. Yang, “A novel method of determining semiconductor parameters in EBIC and SEBIC modes of SEM”, *Semiconductor Science and Technology*, vol. 18, pp. 361–366, 2003.

[15] V. K. Ong and D. Wu, “Determination of diffusion length from within a confined region with the use of ebic”, *IEEE Transactions on Electron Devices*, vol. 48, no. 2, pp. 332–337, 2001.

[16] D. S. H. Chan, V. K. S. Ong, and J. C. H. Phang, "A direct method for the extraction of diffusion length and surface recombination velocity from an ebic line scan: Planar junction configuration", *IEEE Transactions on Electron Devices*, vol. 42, no. 5, pp. 963–968, May 1995.
[17] M. Kittler and W. Seifert, "On the origin of EBIC defect contrast in silicon", *Physica Status Solidi*, vol. 138, pp. 687–693, 1993.
[18] T. S. Fell, P. R. Wilshaw, and M. D. D. Coteau, "EBIC investigations of dislocations and their interactions with impurities in silicon", *Physica Status Solidi*, vol. 138, pp. 695–704, 1993.
[19] S. Kirnstoetter, M. Faccinelli, M. Jelinek, W. Schutereder, J. G. Laven, H.-J. Schulze, and P. Hadley, "Depletion of superjunction power MOSFETs visualized by electron beam induced current and voltage contrast measurements", *Physica status solidi C*, vol. 11, 2014.
[20] E. Edri, S. Kirmayer, S. Mukhopadhyay, K. Gartsman, G. Hodes, and D. Cahen, "Elucidating the charge carrier separation and working mechanism of CH3NH3PbI3 xClx perovskite solar cells", *Nature communications*, vol. 5, 2014.
[21] M. A. Green, A. Ho-Baillie, and H. J. Snaith, "The emergence of perovskite solar cells", *Nature Photonics*, vol. 8, 2014.
[22] O. Marcelot, S. I. Maximenko, and P. Magnan, "Plan view and cross-sectional view EBIC measurements: Effect of e-beam injection conditions on extracted minority carrier transport properties", *IEEE Transactions on Electron Devices*, vol. 61, no. 7, 2014.
[23] D. A. Neamen, *Semiconductor Physics and Devices*, 3rd ed. McGrawHill, 2002.
[24] B. van Zeghbroeck. (2011). Principles of semiconductor devices, [Online]. Available: `http://ecee.colorado.edu/~bart/book/book/title.htm` (visited on 09/14/2013).
[25] D. K. Schroder, *Semiconductor Material and Device Characterization*, 2nd ed. John Wiley and Sons, Inc., 1998, ISBN: 0-471-24139-3.
[26] D. E. Aspnes, "Recombination at semiconductor surfaces and interfaces", *Surface Science*, vol. 132, pp. 406–421, 1983.
[27] A. Cuevas and D. Macdonald, "Measuring and interpreting the lifetime of silicon wafers", *Solar Energy*, vol. 76, pp. 255–262, 2004.
[28] H. Nagel, C. Berge, and A. G. Alberle, "Generalized analysis of quasi-steady-state and quasi-transient measurements of carrier lifetimes in semiconductors", *Journal of Applied Physics*, vol. 86, no. 11, 1999.
[29] A. Irace, L. Sirleto, P. Spirito, G. F. Vitale, A. Cutolo, S. Campopiano, and L. Zeni, "Optical characterization of the recombination process in silicon wafers, epilayers and devices", *Optics and Lasers in Engineering*, vol. 39, no. 6, pp. 219–232, 2003.
[30] J. Härkönen, E. Tuovinen, Z. Li, P. Luukka, E. Verbitskaya, and V. Eremin, "Recombination lifetime characterization and mapping of silicon wafers and detectors using the microwave photoconductivity decay (μpcd) technique", *Materials Science in Semiconductor Processing*, vol. 9, pp. 261–265, 2006.
[31] D. C. Gupta, F. R. Bacher, and W. M. Huges, Eds., *Recombination lifetime measurements in silicon*, STP 1340, 1998.
[32] R. Ahrenkiel, "Recombination processes and lifetime measurements in silicon photovoltaics", *Solar Energy Materials and Solar Cells*, vol. 76, pp. 243–256, 2003.
[33] S. Herlufsen, D. Hinken, M. Offer, J. Schmidt, and K. Bothe, "Validity of calibrated photoluminescence lifetime measurements of crystalline silicon wafers for arbitrary lifetime and injection ranges", *IEEE Journal of Photovoltaics*, vol. 3, no. 1, pp. 381–386, 2013.

[34] J. Giesecke, B. Michl, F. Schindler, M. Schubert, and W. Warta, "Spatially resolved carrier lifetime calibrated via quasi-steady-state photoluminescence", *Energy Procedia*, vol. 8, pp. 64–70, 2011.

[35] J. Giesecke, M. Schubert, B. Michl, F. Schindler, and W. Warta, "Minority caarrier lifetime imaging of silicon wafers calibrated by quasi-steady-state photoluminescence", *Solar Energy Materials and Solar Cells*, vol. 95, pp. 1011–1018, 2011.

[36] M. Wilson, P. Edelmann, J. Lagowski, S. Olibet, and V. Mihailetchi, "Improved QSS-μPCD measurement with quality of decay control: Correlation with steady-state carrier lifetime", *Solar Energy Materials and Solar Cells*, vol. 106, pp. 66–70, 2012.

[37] M. Wilson, J. Lagowski, P. Edelman, A. Savtchouk, A. Findlay, S. Oliber, and V. Mihailetchi, "Unified lifetime measurement for silicon PV", in *38th Photovoltaic Specialists Conference*, Austin. TX, Jun. 2012, pp. 1860–1863.

[38] O. Palais, L. Clerc, A. Arcari, M. Stemmer, and S. Martinuzzi, "Mapping of minority carrier lifetime and mobility in imperfect silicon wafers", *Materials Science in Semiconductor Processing*, vol. 4, pp. 27–29, 2001.

[39] O. Palais, J. Gervais, L. Clerc, and S. Martinuzzi, "High resolution lifetime scan maps of silicon wafers", *Materials Science and Engineering*, vol. B71, pp. 47–50, 2000.

[40] W. Pengchan, T. Phetchakul, and A. Poyai, "The logal generation and rcombination lifetime based on forward diode characteristics diagnostics", *Journal of Crytal Growth*, vol. 362, pp. 300–303, 2013.

[41] S. Kumar, P. Singh, G. Chilana, and S. Dhariwal, "Generation and recombination lifetime measurement in silicon wafers using impedance spectroscopy", *Semiconductor Science and Technology*, vol. 24, 2009.

[42] J. Kzisek, Z. Machacek, and V. Benda, "Monitoring of carrier lifetime distribution in high power semiconductor device technology", *Microelectronics Journal*, vol. 39, pp. 884–889, 2008.

[43] L.Reimer, *Scanning Electron Microscopy – Physics of Image Formation and Microanalysis*. Springer, 1998.

[44] R. Egerton, P. Li, and M. Malac, "Radiation damage in the tem and sem", *Micron*, vol. 35, pp. 399–409, 2004. DOI: `10.1016/j.micron.2004.02.003`.

[45] C. Pantano, "Electron beam damage in auger electron spectroscopy", *Application of Surface Science*, vol. 7, pp. 115–141, 1980. DOI: `10.1016/0378-5963(81)90065-9`.

[46] D. Drouin, A. R. Couture, D. Joly, X. Tastet, V. Aimez, and R. Gauvin, "CASINO V2.42—A fast and easy-to-use modeling tool for scanning electron microscopy and microanalysis users", *Scanning*, vol. 29, pp. 92–101, 2007.

[47] S. M. Sze, *Physics of semiconductor devices*, 2nd ed. John Wiley and Sons, 1981.

[48] J. Singh, *Semiconductor Devices, Basic Principles*. John Wiley, 2001.

[49] T. Kushida, S. Tanaka, C. Morita, T. Tanji, and Y. Ohshita, "Mapping of minority carrier lifetime distributions in multicrystalline silicon using transient electron-beam-induced current", *Journal of Electron Microscopy*, vol. 61, no. 5, pp. 293–298, 2012.

[50] D. E. Ioannou, "A sem-ebic minority-carrier lifetime-measurement technique", *Journal of Physics D: Applied Physics*, vol. 13, no. 4, pp. 611–616, 1980.

[51] O. Kurniawan and V. K. Ong, "An analysis of the factors affecting the alpha parameter used for extracting surface recombination velocity in EBIC measurements", *Solid-State Electronics*, vol. 50, pp. 345–354, 2001.

[52] S. Li and Y. Fu, *3D TCAD Simulation for Semiconductor Processes, Devices and Optoelectronics*. Springer, 2012, ISBN: 978-1-4614-0480-4.

[53] G. Armstrong and C. K. Maiti, *Technology Computer Aided Design for Si, SiGe and GaAs Integrated Circuits*. The Institution of Engineering and Technology, 2007, ISBN: 978-0-86341-743-6.

[54] Synopsis, *Sentaurus stucture editor user guide*, Version L-2016.03, 2016.

[55] T. E. Everhart and P. H. Hoff, "Determination of kilovolt electron energy dissipation versus penetration distance in solid materials", *Journal of Applied Physics*, vol. 42, no. 13, pp. 5837–5846, 1971.

[56] C. Donolato, "An analytical model of SEM and STEM charge collection images of dislocations in thin semiconductor layers", *Physica Status Solidi*, vol. 65, pp. 649–658, 1981.

[57] E. Yakimov, "Electron beam induced current investigations of electrical inhomogeneities with high spatial resolution", *Scanning Microscopy*, vol. 6, no. 1, pp. 81–96, 1991.

[58] Synopsis, *Sentaurus device user guide*, Version K-2015.06, 2015.

[59] T. Otaredian, "The influence of the surface and oxide charge on the surface recombination process", *Solid-State Electronics*, vol. 36, pp. 905–9015, 1993.

[60] A. Kraxner, F. Roger, B. Loeffler, M. Faccinelli, S. Kirnstoetter, R. Minixhofer, and P. Hadley, "Investigation on CMOS photodiodes using scanning electron microscopy with electron beam induced current measurements", in *SPIE Proceedings, Scanning Microscopies 2014*, vol. 9236, 2014. DOI: `10.1117/12.2066124`.

[61] A. Kraxner, F. Roger, B. Loeffler, M. Faccinelli, E. Fisslthaler, R. Minixhofer, and P. Hadley, "An ebic model for TCAD simulation to determine the surface recombination rate in semiconductor devices", *IEEE Transactions on Electron Devices*, vol. PP, no. 99, 2016. DOI: `10.1109/TED.2016.2606703`.

[62] G. W. Trucks, K. Raghavacharai, G. S. Higashi, and Y. J. Chabal, "Mechanism of hf etching of silicon surfaces: A theoretical understanding of hydrogen passivation", *Physcial Review Letters*, vol. 65, no. 4, 1990.

[63] E. Yablonovitch, D. L. Allara, C. C. Chang, T. Gmitter, and T. B. Bright, "Unusually low surface-recombination velocity on silicon and germanium surfaces", *Physical Review Letters*, vol. 57, no. 2, 1986.

[64] L. A. Giannuzzi and F. A. Stevie, Eds., *Introduction to focused ion beams - Instrumentation, Theory, Techniques and Practice*. Springer, 2005.

[65] X. Correig, J. Calderer, E. Blasco, and R. Alcubilla, "Comments on the use of the surface recombination velocity concept", *Solid State electronics*, vol. 33, no. 5, pp. 477–484, 1990.

[66] D. J. Fitzgerald and A. S. Grove, "Surface recombination in semiconductors", *Surface Science*, vol. 9, pp. 347–369, 1968.

[67] J. G. Fossum and D. Lee, "A physical model for the dependence of carrier lifetime on doping density in nondegenerate silicon", *Solid-State Electronics*, vol. 25, pp. 741–747, 1982.

[68] W. H. Hackett, R. H. Saul, R. W. Dixon, and G. W. Kammlott, "Scanning electron microscope characterization of GaP red emitting diodes", *Journal of Applied Physics*, vol. 43, pp. 2857–2868, 1975.

[69] A. S. Grove and D. J. Fitzgerald, "Surface effects on p-n junctions: Characteristics of surface space-charge regions under non-equilibrium conditions", *Solid-State Electronics*, vol. 9, pp. 783–806, 1966.

[70] J. M. Park, R. Minixhofer, and M. Schrems, "Cost effective high-voltage IC technology implemented in a standard CMOS process," in *EKC 2010*, vol. 138, 2011, pp. 97–105.

[71] A. Kraxner, E. Wachmann, I. Jonak-Auer, J. Teva, J. M. Park, and R. Minixhofer, "Characterization of spectral optical responsivity of Si-photodiode junction combinations available in a 0.35μm HV-CMOS technology", in *Proceedings of SPIE*, vol. 8767, 2013.

[72] A. Kraxner and R. Minixhofer, "A novel measurement set up for optical characterization of CMOS photodiodes using immersion oil", in *2014 IEEE Photonics Conference*, Oct. 2014, pp. 566–567. DOI: 10.1109/IPCon.2014.6995266.

[73] S. Reyntjens and R. Pures, "A review of focused ion beam applications in microsystem technology", *Journal of Micromechanics and Microengineering*, vol. 11, pp. 287–300, 2001.

[74] J. Melngailis, "Focused ion beam technology and applications", *Journal of Vacuum Science & Technology B*, vol. 5, no. 2, pp. 469–495, 1987. DOI: http://dx.doi.org/10.1116/1.583937.

[75] L. Lechner, J. Biskupek, and U. Kaiser, "Improved focused ion beam target preparation of (S)TEM specimen - a method of obtaining ultrathin lamellae", *Microscopy and Microanalysis*, 2012. DOI: 10.1017/S1431927611012499.

My Publications

A. Kraxner, F. Roger, B. Loeffler, M. Faccinelli, S. Kirnstoetter, R. Minixhofer, and P. Hadley, "Investigation on CMOS photodiodes using scanning electron microscopy with electron beam induced current measurements", in *SPIE Proceedings, Scanning Microscopies 2014*, vol. 9236, 2014. DOI: 10.1117/12.2066124.

A. Kraxner and R. Minixhofer, "A novel measurement set up for optical characterization of CMOS photodiodes using immersion oil", in *2014 IEEE Photonics Conference*, Oct. 2014, pp. 566–567. DOI: 10.1109/IPCon.2014.6995266.

A. Kraxner, J. M. Park, and R. Minixhofer, "Investigation of the influence of unwanted micro lenses caused by semiconductor processing excursions on optical behavior of CMOS photodiodes", in *SPIE Proceedings, Physics and Simulation of Optoelectronic Devices XXIII*, vol. 9357, 2015. DOI: 10.1117/12.2079022.

A. Kraxner, F. Roger, B. Loeffler, M. Faccinelli, E. Fisslthaler, R. Minixhofer, and P. Hadley, "An ebic model for TCAD simulation to determine the surface recombination rate in semiconductor devices", *IEEE Transactions on Electron Devices*, vol. PP, no. 99, 2016. DOI: 10.1109/TED.2016.2606703.